VILNIUS UNIVERSITY
AND
CENTER FOR PHYSICAL SCIENCES AND TECHNOLOGY
INSTITUTE OF PHYSICS

Rokas Danilevičius

FIBER LASER BASED TECHNOLOGIES FOR HIGH ENERGY FEMTOSECOND WAVELENGTH-TUNABLE OPTICAL PARAMETRIC CHIRPED PULSE AMPLIFICATION SYSTEMS

Doctoral dissertation,
Physical Sciences, Physics (02P)

Vilnius, 2017

The research was performed in 2012-2016 at the Department of Laser Technologies of the Center for Physical Sciences and Technology and the company EKSPLA.

Scientific supervisor:

Dr. Andrejus Michailovas (Center for Physical Sciences and Technology, Physical Sciences, Physics - 02P).

Scientific advisor:

Dr. Nerijus Rusteika (Center for Physical Sciences and Technology, Physical Sciences, Physics - 02P).

VILNIAUS UNIVERSITETAS
IR
VALSTYBINIS MOKSLINIS TYRIMŲ INSTITUTAS
FIZINIŲ IR TECHNOLOGIJOS MOKSLŲ CENTRAS

Rokas Danilevičius

SKAIDULINIŲ LAZERIŲ TECHNOLOGIJOS DIDELĖS ENERGIJOS FEMTOSEKUNDINĖMS DERINAMO BANGOS ILGIO OPTINĖMS PARAMETRINĖMS ČIRPUOTŲ IMPULSŲ STIPRINIMO SISTEMOMS

Daktaro disertacija,
Fiziniai mokslai, fizika (02P)

Vilnius, 2017

Disertacija rengta 2012-2016 metais Fizinių ir Technologijos Mokslų Centro Lazerinių technologijų skyriuje ir kompanijoje EKSPLA.

Mokslinis vadovas:

Dr. Andrejus Michailovas (Fizinių ir technologijos mokslų centras, fiziniai mokslai, fizika - 02P).

Mokslinis konsultantas:

Dr. Nerijus Rusteika (Fizinių ir technologijos mokslų centras, fiziniai mokslai, fizika - 02P).

Contents

Acknowledgements

The work was supported by laser manufacturing and development company EKSPLA, Research Council of Lithuania under projects LAT-10/2016 and MIP- 099/2011 (FEMTOSKAIDULA) and European Social Fund under project VP1-3.1-ŠMM-10-V-02-002.

First of all, I am grateful to my scientific supervisor **Dr. Andrejus Michailovas** for creating perfect conditions to study, improve and present my achievements at international conferences.

I express my sincere gratitude to **Dr. Nerijus Rusteika** for endless help and support throughout my PhD studies. You will always be an example to follow for me.

Special thanks to **Dr. Audrius Zaukevičius** for consulting me and giving a valuable insight into my work. Furthermore, thanks for being the best teammate in table football matches.

Thanks to **Dr. Kęstutis Regelskis** for important help with numerical modelling.

Thanks to **Julijanas Želudevičius** for his valuable support and especially for appreciating my music.

Thanks to **Dr. Karolis Viskontas** for SESAM supply and pleasant conversations at coffee breaks.

Thanks to the rest of my colleagues from the fiber technology group of EKSPLA: **Saulius Frankinas, Tadas Bartulevičius, Karolis Madeikis** and **Laurynas Veselis** for the friendly atmosphere and support.

Thanks to **Dovilė Mackevičiūtė** from the fiber laser manufacturing group of EKSPLA for various support during my studies. I will always appreciate it.

Thanks to **Tomas Kašponas**. You are the handiest big man I have ever known and a true friend and advisor in engineering.

Finally, I would like to thank my friends and family for support during the studies of physics and what is more important - the never ending studies of life. Love you all, your help will never be forgotten!

List of abbreviations

ASE	amplified spontaneous emission
BPF	band-pass filter
BS	beam splitter
CFBG	chirped fiber Bragg grating
CPA	chirped pulse amplification
DPSS	diode-pumped solid-state
FBG	fiber Bragg grating
FCPA	fiber chirped pulse amplification
FROG	frequency resolved optical gating
FS	fused silica
FWHM	full width at a half maximum
GVD	group velocity dispersion
HHG	high-order harmonic generation
LD	laser diode
LMA	large-mode-area
LPF	long-pass filter
MFD	mode field diameter
NLSE	nonlinear Schrödinger equation
NOPA	noncollinear optical parametric amplifier
OPA	optical parametric amplifier
OPCPA	optical parametric chirped pulse amplification
PF	protection filter
PM	polarization maintaining
RA	regenerative amplifier
ROC	radius of curvature
SCG	supercontinuum generation
SESAM	semiconductor saturable absorber mirror
SHG	second harmonic generation
SM	single-mode
SPM	self-phase modulation
TEC	thermoelectric cooler
TL	transform-limited
TOD	third-order dispersion
WDM	wavelength division multiplexer
WLC	white-light supercontinuum
WLG	white-light generation

Introduction

Femtosecond wavelength-tunable laser systems are essential for ultrafast science applications such as time-resolved pump-probe experiments (transient absorption, fluorescence up-conversion, time-resolved photoelectron spectroscopy, time-resolved mass spectrometry), femtosecond digital holography, CARS (Coherent Anti-Stokes Raman Spectroscopy) and others [1-7]. Titanium-doped sapphire is the only practical laser crystal which allows significant wavelength tuning due to the ultra-broad amplification bandwidth [8–10]. However, high energy Ti:sapphire lasers are usually optimized for a constant wavelength operation in femtosecond regime [11]. Optical parametric amplification (OPA) phenomenon [12] enabled the extension of accessible spectral regions from UV to MIR. Incorporation of optical parametric chirped pulse amplification (OPCPA) technique [13,14] leads to the extremely high peak intensity of light which is required by modern laser-matter interaction applications, e.g. HHG (High-Order Harmonic Generation) and attosecond science [15,16]. A common seed source for a high peak power table-top Vis-NIR OPCPA system is a Ti:sapphire femtosecond oscillator [13,17,18]. Alternatively, white-light supercontinuum (WLC) generated by the femtosecond pulses from the regenerative amplifier (Ti:sapphire, Yb:KGW) can be used as a seed [19,20]. In both cases seed pulses have energy in nJ range and need to be preamplified in femtosecond OPA stage before the amplification in OPCPA stage, where pulses are stretched, parametrically amplified using long picosecond pulses as a pump and finally compressed to femtosecond duration. Picosecond Nd^{3+} doped solid-state lasers are usually used as a pump [21–23].

Conventional approach requires using a complex femtosecond CPA laser system and optical or electronic synchronisation of the femtosecond and picosecond laser systems, which typically operate at different wavelengths [24,25]. Furthermore, in many strong field applications, it is important to have very high temporal contrast in picosecond to nanosecond time

scales of the generated femtosecond pulses [14,26]. If pulses from regenerative amplifiers are used in all parametric amplification stages, achievable pulse contrast is limited or requires sophisticated techniques for contrast improvement [26].

Already mature and yet rapidly emerging ultrafast fiber laser technologies can definitely be a field to investigate for development of the ultrafast wavelength-tunable systems. Fiber-based laser sources offer many practical advantages compared with solid-state systems, including high average power output, nearly diffraction-limited beam quality, compact and robust design and maintenance-free operation. A broad emission spectrum of Yb^{3+} doped fused silica fibers allows for amplification of ultrashort pulses. Furthermore, methods to tune the wavelength intrinsically in fiber have been demonstrated already a decade ago not only for telecommunication wavelengths [27–29] but also at 1 μm [30–32]. However, these approaches are confined to a relatively narrow tuning range and are often hard to implement.

Fiber laser technology can be also employed in OPCPA systems. Er^{3+} and Yb^{3+} doped fiber lasers were used as seed sources [33–35]. Yb-based fiber amplifiers providing high average power sub-ps duration pump pulses were implemented in a few-cycle OPCPA schemes [36–38]. Moreover, fiber OPCPA systems based on a four-wave mixing process were constructed and experimentally realised [39–41]. Although, the output pulse durations from such systems were relatively long, in a sub-ps range, theoretical investigations showed prospects to operate in a few-cycle regime [42].

An important drawback in fiber-based technology is limitations in achieving high pulse energies and high peak powers. Fiber geometry, which offers good thermo-optical properties for high average power operation, is not conducive to achieve high energy ultrashort pulses. In the case of the ultrashort pulse amplification, high peak irradiances in the small diameter fiber core and long interaction length cause a significant impact of nonlinear effects, which limit achievable pulse peak power at the output of the system. Usually, nonlinear effects in fiber are reduced by implementing two main strategies. The first one

is based on the modification of the active fiber itself to increase the mode field diameter (MFD) and to reduce peak irradiance. Conventional large-mode-area (LMA) fibers with numerical apertures reduced to the technologically practical limit of ∼0.06 and with core diameter up to ∼30 μm are currently commercially available. However, larger core diameters suitable for strictly fundamental mode operation are only possible by using advanced microstructured fiber designs, such as different types of photonic crystal fibers [43–45] or chirally-coupled-core fibers [46]. The second strategy, used to avoid nonlinear effects during amplification in a fiber, is chirped pulse amplification (FCPA), when pulses are stretched in time before amplification, amplified, and then recompressed [47]. However, to achieve high-quality transform-limited (TL) pulses at the output, the system design has to be optimised to account for material dispersion and non-uniform spectral gain, which is not a simple task for fiber systems with long fiber lengths and multiple amplification stages [48]. Moreover, when pulses are stretched, even up to the largest practical duration of ∼1 ns, the achievable peak power is still limited by the most dominant nonlinear effect – self-phase modulation (SPM). The SPM-induced nonlinear phase shift of more than 1 rad already affects pulse compression and results in a noticeable temporal broadening and a reduction of the peak power of the recompressed pulses [49].

Considering the advantages and the drawbacks of fiber and solid-state laser technologies, a hybrid approach seems to be optimal and can lead to the construction of a compact, stable and cost-effective high energy femtosecond wavelength-tunable laser. This task was the main goal of my doctoral work.

First of all, numerical modelling software was developed and used to investigate the effects on ultrashort pulses in fiber lasers. The modelling analysis helped to gain knowledge how to conveniently control and modify the ultrashort pulse parameters applying it for practical application. Furthermore, numerical calculations were used to improve a FCPA system. Finally, the whole gathered experience was realised in developing and experimentally implementing a novel hybrid femtosecond high energy wavelength-tunable Vis-NIR OPCPA system.

Scientific novelty

Scientific novelty of this work lies on the incorporation of already proven fiber and solid-state technologies:

1. A novel optically synchronised dual-wavelength all-in-fiber laser source for seeding both femtosecond Yb and picosecond Nd-based solid-state lasers was proposed and experimentally demonstrated.
2. A new method for generation of femtosecond light pulses based on fiber laser technology was investigated and realised experimentally.
3. Method to improve the output pulse contrast in Yb-based FCPA system by applying the temperature gradient on a chirped fiber Bragg grating (CFBG) stretcher and thus controlling the dispersion parameters was investigated numerically and experimentally. This was the first demonstration of such approach at 1 μm wavelength range.
4. A compact femtosecond wavelength-tunable OPCPA system with a novel front-end, which uses a spectrally broadened picosecond fiber oscillator for seeding picosecond diode-pumped solid-state (DPSS) regenerative amplifier and WLC generator was developed and demonstrated experimentally for the first time. This approach eliminates the need of the seed and pump pulse synchronisation therefore greatly simplifying the system and uses all-parametric femtosecond pulse amplification stages potentially increasing the temporal contrast of final pulses.

Practical value

Development of OPCPA systems is a rapidly emerging field in ultrafast laser technology. The use of compact, robust and maintenance-free fiber lasers together with well-established solid-state technologies in an OPCPA system has a high practical potential as it leads to the realisation of a turn-key light source for ultrafast spectroscopy as well as strong field experiments.

This doctoral work has a practical significance in several aspects:

1. A novel patented fiber-based optically synchronised dual-wavelength source was experimentally demonstrated and successfully incorporated in a high energy OPCPA system in collaboration with TU Wien group.
2. Evident output pulse contrast improvement achieved in the experiments with temperature controlled CFBG led to the implementation of this approach in commercial laser systems which are at the final stage of development at company EKSPLA.
3. A novel method to generate femtosecond light pulses was experimentally confirmed and realised in a compact hybrid femtosecond high energy wavelength-tunable OPCPA system which is already commercially available. The product will be the basis for a family of advanced femtosecond laser systems for science and technology.

Statements to defend

S1. Controlling the influence of dispersion and nonlinearity on ultrashort pulse properties in ultrafast fiber laser enables the realisation of an optically synchronised dual-wavelength source to seed both femtosecond Yb and picosecond Nd-based solid-state lasers with sufficient energy for high contrast operation.

S2. Incorporation of pulse temporal and spectral stretching techniques in a picosecond all-in-fiber laser together with the methods of narrowband Nd ions based solid-state and broadband optical parametric amplification enables the realisation of a compact all-optically synchronised fiber/solid-state femtosecond OPCPA system front-end which can be used for high contrast few-cycle pulse amplification.

S3. Implementation of temperature-controlled dispersion CFBG pulse stretcher with 4 independent TEC elements in a Yb-based femtosecond FCPA system contributes to a significant improvement of the compressed pulse contrast and paves the way for even more precise dispersion control by increasing the number of independent TEC units.

S4. Compact femtosecond wavelength-tunable Vis-NIR OPCPA system, featuring more than 20 GW pulse peak power in 680-960 nm wavelength range from a single OPCPA amplification stage, can be realised using all-optically synchronised picosecond fiber laser seed and picosecond DPSS laser pump.

Author's contribution

All the research presented in the thesis was performed by the author except the work mentioned in the Co-authors' contribution section. The author developed the modelling software described in Appendix and performed all the numerical calculations and theoretical analysis presented in A1-A5 articles. Furthermore, author constructed and experimentally realised the laser system described in the article A1 and contributed to theoretical and experimental investigations preparing the manuscripts A2, A3 and patents P1, P2.

Co-authors' contribution

- Dr. Andrejus Michailovas was a supervisor of the author's PhD studies and suggested significant ideas for the work published in A1, A2 articles and organised the process of P1 and P2 patenting.
- Dr. Nerijus Rusteika provided the most valuable ideas and consultation in order to achieve the success in this work. Furthermore, Nerijus made a great contribution in preparing manuscripts for A1 and A2 publications.
- Dr. Audrius Zaukevičius developed, constructed and experimentally realised the pump laser described in A1. In addition to this, he shared his huge experience in ultrafast optical parametric amplification topic.
- Rimantas Budriūnas helped to realise a few-cycle pulse compression experimentally and performed a few-cycle pulse characterization by the chirpscan and FROG methods outlined in the A1 article.

- Julijanas Želudevičius accomplished experimental measurements for the A3 article and helped to resolve numerical modelling issues for A3 and A4 articles.
- Dr. Kęstutis Regelskis shared his experience in ultrashort pulse formation, propagation and amplification modelling and was a supervisor of work presented in A3, A4 papers.
- Dr. Karolis Viskontas constructed and supplied fiber pigtailed SESAM units for fiber oscillators used in the experiments of A1-A4 articles.

Scientific papers

Publications related to the topic of the thesis:

A1. **R. Danilevičius,** A. Zaukevičius, R. Budriūnas, A. Michailovas, and N. Rusteika, *Femtosecond wavelength-tunable OPCPA system based on picosecond fiber laser seed and picosecond DPSS laser pump*, Opt. Express **24**, 17532 (2016). DOI: 10.1364/OE.24.017532.

A2. K. Michailovas, A. Baltuška, A. Pugžlys, V. Smilgevičius, A. Michailovas, A. Zaukevičius, **R. Danilevičius**, S. Frankinas, and N. Rusteika, *Combined Yb/Nd driver for optical parametric chirped pulse amplifiers*, Opt. Express **24**, 22261 (2016). DOI: 10.1364/OE.24.022261.

A3. J. Želudevičius, **R. Danilevičius**, and K. Regelskis, *Optimization of pulse compression in a fiber chirped pulse amplification system by adjusting dispersion parameters of a temperature-tuned chirped fiber Bragg grating stretcher*, J. Opt. Soc. Am. B **32**, 812 (2015). DOI: 10.1364/JOSAB.32.000812.

Other publications:

A4. J. Želudevičius, **R. Danilevičius**, K. Viskontas, N. Rusteika, and K. Regelskis, *Femtosecond fiber CPA system based on picosecond master oscillator and power amplifier with CCC fiber*, Opt. Express, **21**, 5338 (2013). DOI: 10.1364/OE.21.005338.

A5. J. Adamonis, N. Rusteika, **R. Danilevičius**, and A. Krotkus, *A Compact Terahertz Burst Emission System Driven With 1 μm Fiber Laser*, Opt. Comm. **293**, 61-64 (2013). DOI: 10.1016/j.optcom.2012.11.100.

Patents

P1. N. Rusteika, A. Michailovas, **R. Danilevičius**, V. Vosylius, *Dviejų bangos ilgių optiškai sinchronizuotų ultratrumpųjų šviesos impulsų generavimo būdas ir lazerinis šaltinis*. Patent number: LT6122. Patent extension to EU: *Method and laser source for generation of optically synchronised dual-wavelength ultrashort light pulses*. Patent application No. 14177007.3.

P2. N. Rusteika, **R. Danilevičius**, A. Zaukevičius, A. Michailovas, *Femtosekundinių šviesos impulsų gavimo būdas ir lazerinis šaltinis*. Patento numeris: LT6231. Patent extension to EU: *Method for generation of femtosecond light pulses, and laser source thereof*. Patent application No. 15159873.7.

Conference presentations

Presentations directly related to the topic of the thesis:

C1. **R. Danilevičius**, R. Budriūnas, A. Michailovas, N. Rusteika, *Few-Cycle Femtosecond OPCPA Front-End based on Picosecond Fiber Laser Seed and Picosecond Solid State Regenerative Amplifier Pump*, 6th EPS-QEOD EUROPHOTON conference "Solid State, Fibre, and Waveguide Coherent Light Sources“, Neuchâtel, Switzerland, August 24-29, 2014 (poster presentation).

C2. **R. Danilevičius**, A. Zaukevičius, A. Michailovas, N. Rusteika, *Femtosecond Tunable Wavelength OPCPA System Based on Picosecond Fiber Laser Seed and Picosecond DPSS Laser Pump*, CLEO®/Europe-EQEC 2015, Munich, Germany, June 21-25, 2015 (poster presentation).

C3. **R. Danilevičius**, R. Budriūnas, A. Michailovas, N. Rusteika, *Femtosecond Tunable Wavelength OPCPA System Frontend Based on Hybrid Fiber-DPSS Laser*, Advanced Laser Technologies (ALT15), Faro, Portugal, September 7-11, 2015 (poster presentation).

C4. J. Želudevičius, **R. Danilevičius**, K. Regelskis, *Tuning of CFBG pulse stretcher dispersion parameters by controlling temperature distribution*, Northern Optics & Photonics 2015 (NOP 2015), Lappeenranta, Finland, June 2-4, 2015 (poster presentation).

C5. **R. Danilevičius**, A. Zaukevičius, A. Michailovas, N. Rusteika, *Compact Femtosecond Tunable Wavelength Vis-NIR OPCPA System Based on Picosecond Fiber Laser Seeded Frontend*, CLEO 2016, San Jose, USA, June 5-10, 2016 (poster presentation).

C6. **R. Danilevičius**, A. Zaukevičius, A. Michailovas, N. Rusteika, *Novel Approach Table-top Vis-NIR OPCPA System*, 17th International Conference "Laser Optics 2016", St. Petersburg, Russia, June 27 – July 1, 2016 (oral presentation).

Other presentations at conferences:

C7. J. Želudevičius, **R. Danilevičius**, K. Viskontas, N. Rusteika, K. Regelskis, *Femtosecond Fiber CPA System Seeded by Bandwidth-Limited Picosecond Pulses*, CLEO®/Europe-EQEC 2013, Munich, Germany, May 12-16, 2013 (poster presentation).

C8. **R. Danilevičius**, J. Želudevičius, K. Viskontas, N. Rusteika, K. Regelskis, *Femtosecond Fiber CPA System Seeded by Bandwidth-limited Picosecond Pulses: Numerical and Experimental Study,* XX Belarussian-Lithuanian seminar "Lasers and optical nonlinearity", Vilnius, Lithuania, November 21-22, 2013 (oral presentation).

C9. **R. Danilevičius**, N. Rusteika, *Derinamos siaurajuostės terahercinės spinduliuotės generavimo čirpuotais impulsais iš skaidulinio lazerio modeliavimas,* LNFK-40, Vilnius, Lithuania, June 10-12, 2013 (poster presentation).

C10. **R. Danilevičius**, J. Želudevičius, N. Rusteika, K. Regelskis, *Reduction of third order dispersion mismatch between fiber stretcher and grating compressor by using split-second-grating compressor design,* DOI: http://dx.doi.org/10.1109/LO.2014.6886277, 16th International Conference

„Laser Optics 2014“, St. Petersburg, Russia, June 30 – July 04, 2014 (poster presentation).

C11. J. Želudevičius, **R. Danilevičius**, K. Viskontas, N. Rusteika, K. Regelskis, *Performance of nonlinear ultra-short pulse fiber CPA system using power amplifiers with core diameter from 12 to 33 μm*, DOI: http://dx.doi.org/10.1109/LO.2014.6886281, 16th International Conference „Laser Optics 2014“, St. Petersburg, Russia, June 30 – July 04, 2014 (poster presentation).

C12. S. Frankinas, **R. Danilevičius**, N. Rusteika, „High power femtosecond CPA system with TOD compensating chirped fiber Bragg grating stretcher“. DOI: http://dx.doi.org/10.1109/LO.2014.6886278, 16th International Conference „Laser Optics 2014“, St. Petersburg, Russia, June 30 – July 04, 2014 (poster presentation).

C13. J. Želudevičius, **R. Danilevičius**, K. Viskontas, N. Rusteika, K. Regelskis, *Ultrashort-Pulse Nonlinear Fiber CPA System Performance Using Power Amplifiers with Core Diameter from 12.5 to 33 μm*, 6th EPS-QEOD EUROPHOTON conference "Solid State, Fibre, and Waveguide Coherent Light Sources“, Neuchâtel, Switzerland, August 24-29, 2014 (poster presentation).

C14. J. Adamonis, R. Venckevičius, I. Kašalynas, **R. Danilevičius**, N. Rusteika, R. Adomavičius, A. Krotkus, *Terahertz generation by optical mixing of chirped fiber laser pulses*, 39th International Conference on Infrared, Millimeter, and Terahertz Waves, The University of Arizona, Tucson, AZ, USA, September 14-19, 2014 (poster presentation).

The structure of the thesis

The material of the thesis is divided into 4 main parts. First, methods and technologies relevant to this work are presented in Literature review. The following chapters cover the research part of the thesis. Chapter 2 is dedicated to outline two novel fiber-based methods for OPCPA systems and their experimental realisation. An approach of compressed pulse contrast improvement in Yb-based FCPA system is presented in Chapter 3. Finally, in

Chapter 4 implementation of the developed methods into a femtosecond high energy wavelength-tunable Vis-NIR OPCPA system is presented. The methodology of numerical modelling is described in Appendix A.

1 Literature review

Ultrafast optical parametric amplification

The dawn of femtosecond technology was more than four decades ago, when passively mode-locked dye lasers capable of generating less than 1 ps pulses were produced [50]. Although, OPA phenomenon was discovered and experimentally realised even earlier [51,52], only the manufacturing of nonlinear crystals with high second-order susceptibility [53] and the invention of broadband solid-state lasers, in particular, Ti:sapphire based systems with implemented Kerr-lens mode-locking technique [8,54,55], led to the efficient amplification and significant progress. These developments opened prospects for new fields of research in physics, chemistry, biology and exploration of new regimes of light-matter interaction [56].

The principle of OPA is straightforward. A high frequency and intensity beam (pump) amplifies a lower frequency and intensity beam (signal) in a suitable nonlinear crystal. In addition to this, a third beam (idler) is generated. The energy and momentum conservation laws must be satisfied [12]:

$$\hbar\omega_p = \hbar\omega_s + \hbar\omega_i, \tag{1.1}$$

$$\hbar\vec{k}_p = \hbar\vec{k}_s + \hbar\vec{k}_i, \tag{1.2}$$

where ω_p, ω_s, ω_i are frequencies of the pump, signal and idler respectively and $\vec{k}_p$, $\vec{k}_s$, $\vec{k}_i$ are the wave vectors of the pump, signal and idler respectively.

The interaction of the three waves is governed by coupled amplitude equations. Assuming OPA with ultrashort pulses in a collinear geometry, amplitudes of the signal, pump and idler change according to the equations [12]:

$$\frac{\partial A_s}{\partial z} + \frac{1}{v_{gs}}\frac{\partial A_s}{\partial t} = -i\frac{\omega_s d_{eff}}{n_s c}A_i^* A_p \exp(-i\Delta kz), \tag{1.3}$$

$$\frac{\partial A_i}{\partial z} + \frac{1}{v_{gi}}\frac{\partial A_i}{\partial t} = -i\frac{\omega_i d_{eff}}{n_i c}A_s^* A_p \exp(-i\Delta kz), \tag{1.4}$$

$$\frac{\partial A_p}{\partial z} + \frac{1}{v_{gp}}\frac{\partial A_p}{\partial t} = -i\frac{\omega_p d_{eff}}{n_p c}A_s A_i \exp(i\Delta kz), \tag{1.5}$$

where d_{eff} is the effective nonlinear optical coefficient, which depends on propagation direction and polarization of the beams, $\Delta k = k_p - k_s - k_i$ is the wave vector mismatch, c is the speed of light, n_s, n_i, n_p are the refractive indexes at signal, idler and pump frequencies respectively and v_{gs}, v_{gi}, v_{gp} are the group velocities of these three waves.

Amplification characteristics of OPA can be easily presented by solving the coupled amplitude equations for monochromatic beams. In this case, time derivatives of the amplitudes are neglected. Then, the energy flow of signal, idler and pump waves is described by Manley-Rowe relations [12]:

$$\frac{1}{\omega_i}\frac{dI_i}{dz} = \frac{1}{\omega_s}\frac{dI_s}{dz} = -\frac{1}{\omega_p}\frac{dI_p}{dz}, \tag{1.6}$$

where I denotes intensities of the three waves. In the case of OPA, a weak signal beam at frequency ω_s interacts with much stronger pump beam at frequency ω_p which loses its power to the signal and the newly generated idler beam at frequency ω_i. During the interaction, the signal beam is significantly amplified as well as the idler.

Under the conditions of no pump depletion, assuming that the initial signal intensity is I_{s0} and no idler beam is present, equations (1.3)-(1.5) can be solved to describe the change of signal and idler intensities after propagation length L along nonlinear crystal [12]:

$$I_s(L) = I_{s0}\left(1 + \frac{\Gamma^2}{g^2}\sinh^2(gL)\right), \tag{1.7}$$

$$I_i(L) = I_{s0}\frac{\omega_i}{\omega_s}\frac{\Gamma^2}{g^2}\sinh^2(gL), \tag{1.8}$$

$$g = \sqrt{\Gamma^2 - \left(\frac{\Delta k}{2}\right)^2}, \tag{1.9}$$

$$\Gamma^2 = \frac{2\omega_i\omega_s d_{eff}^2 I_p}{n_i n_s n_p \varepsilon_0 c^3} = \frac{8\pi^2 d_{eff}^2 I_p}{n_i n_s n_p \lambda_i \lambda_s \varepsilon_0 c}, \tag{1.10}$$

where ε_0 is the vacuum permittivity and Γ is the nonlinear coefficient. Considering the case of perfect phase matching ($\Delta k = 0$) and the large-gain approximation ($\Gamma L \gg 1$) lead to the simplification of the above equations [12]:

$$I_s(L) \cong \frac{1}{4} I_{s0} \exp(2\Gamma L), \tag{1.11}$$

$$I_i(L) \cong \frac{\omega_i}{4\omega_s} I_{s0} \exp(2\Gamma L). \tag{1.12}$$

The ratio of signal and idler intensities corresponds to the equal number of generated signal and idler photons. The parametric gain equals to:

$$G = \frac{I_s(L)}{I_{s0}} \cong \frac{1}{4} \exp(2\Gamma L). \tag{1.13}$$

Under the presence of strong pump field, seed photons at ω_s frequency provokes the generation of additional signal photon and also a photon at idler frequency ω_i. In addition to this, the amplification of idler causes the generation of signal photon. This positive feedback determines the exponential growth of both signal and idler waves.

The maximum parametric gain will be achieved in a perfect phase matching conditions ($\Delta k = 0$), which can be expressed in a form:

$$n_p = \frac{n_i \omega_i + n_s \omega_s}{\omega_p}. \tag{1.14}$$

This condition cannot be satisfied in bulk isotropic materials at the normal dispersion frequency range where $n_i < n_s < n_p$. The situation is different in anisotropic birefringent crystals, where two equal frequency but perpendicular polarization waves can propagate in the same direction with different phase velocities. One wave, which refractive index is independent of propagation direction is called an ordinary ("o") wave, the other is called an extraordinary ("e") wave. Refractive index depends on the propagation direction for "e" wave. Negative uniaxial crystals ($n_e < n_0$) are commonly used in ultrafast OPA schemes, where the pump wave is polarized in the extraordinary direction [12]. Type I phase matching is defined when both signal and idler waves are ordinary and perpendicular to the pump ($o_s + o_i \rightarrow e_p$). If either signal or idler wave has a parallel to the pump polarization, type II phase matching takes place.

Generally, the phase matching condition can be achieved by changing the angle θ between the optical axis of the crystal and the wave vector of propagating beams or adjusting the crystal temperature. For type I configuration in a negative uniaxial crystal phase matching angle is obtained according to the relations [12]:

$$n_{ep}(\theta)\omega_p = n_{os}\omega_s + n_{oi}\omega_i, \tag{1.15}$$

$$\theta = \sin^{-1}\left[\frac{n_{ep}}{n_{ep}(\theta)}\sqrt{\frac{n_{op}^2 - n_{ep}^2(\theta)}{n_{op}^2 - n_{ep}^2}}\right], \tag{1.16}$$

in which n_{ep} and n_{op} are the principal extraordinary and ordinary refractive indexes of the pump (at θ = 90° plane).

Temporal dependence must be taken into account for femtosecond OPA. In that case, the effects of group velocity mismatch (GVM) between the interacting pulses are analysed by including the first derivatives of the amplitude with respect to time in (1.3)-(1.5) equations. GVM between the pump and signal or idler pulses limits the interaction length in which the parametric amplification occurs. This effect can be described by defining the pulse splitting length:

$$L_{jp} = \frac{\tau}{GVM_{jp}}, \quad j = s, i, \tag{1.17}$$

$$GVM_{jp} = \frac{1}{v_{gj}} - \frac{1}{v_{gp}}.$$

Furthermore, GVM between signal and idler limits the phase matching bandwidth. Considering the perfect phase matching at the central signal frequency, Δk is approximated to the first order and, within the large-gain approximation, phase matching bandwidth at FWHM is calculated as:

$$\Delta\nu \cong \frac{2\sqrt{\ln 2}}{\pi}\sqrt{\frac{\Gamma}{L}}\frac{1}{|GVM_{si}|}. \tag{1.18}$$

It is seen from the above equation, that large GVM can significantly decrease $\Delta\nu$, which becomes important for broadband femtosecond pulse OPA. Approaching the phase matching condition at degeneracy ($\omega_s \rightarrow \omega_i$), wave vector mismatch Δk must be expanded to the second order, leading to:

$$\Delta\nu \cong \frac{2\sqrt[4]{\ln 2}}{\pi}\sqrt[4]{\frac{\Gamma}{L}}\frac{1}{\left|\frac{\partial^2 k_s}{\partial\omega_s^2}+\frac{\partial^2 k_i}{\partial\omega_i^2}\right|}. \tag{1.19}$$

For type II interaction the bandwidth $\Delta\nu$ is smaller than for type I but almost constant at the crystal tuning range, while for type I interaction the bandwidth increases approaching degeneracy [12]. Due to such characteristic features, type I phase matching is usually used to produce shortest pulses and type II phase matching is chosen to obtain a broad tuning range [57]. Moreover, broadband type I OPA will exhibit spectral modulations near degeneracy due to the interference between signal and idler waves having parallel polarizations.

During the last decade of the 20th century, typical femtosecond OPA systems operating at Vis-NIR wavelength was pumped by the second harmonic of Ti:sapphire laser using white-light supercontinuum [57,58] or parametric superfluorescence generation [59–61] as a seed. Incorporating dispersion compensation technique, which usually was a prism pair compressor, less than 30 fs transform-limited (TL) pulses could be achieved [62].

The main limitation to produce shorter pulses was a narrow phase matching bandwidth, which could be broadened by shortening the nonlinear crystal. However, such method is highly inefficient. The breakthrough was achieved when noncollinear optical parametric amplifiers (NOPA) were developed [63,64]. In NOPA scheme, signal and pump waves propagate through a nonlinear crystal forming an angle α. Idler is generated at angle Ω with respect to the signal. The schematic of such configuration is pictured in Fig. 1.1(a).

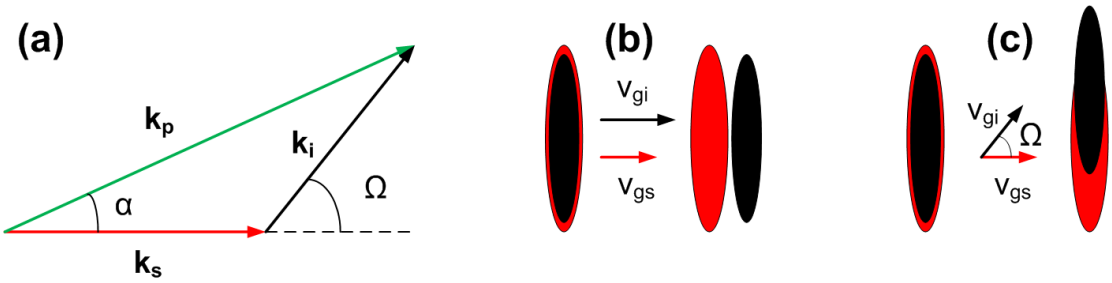

Fig. 1.1 (a) Principal scheme of NOPA geometry; (b) signal and idler pulse propagation in collinear (b) and noncollinear (c) schemes.

A broadband phase matching can be realised for such angle Ω between signal and idler that signal group velocity is equal to the projection of idler group velocity (Fig. 1.1(c)). Due to the different signal and idler group velocities, in a collinear case, these waves get separated during the propagation in the nonlinear crystal. However, in a noncollinear geometry signal and idler waves remain overlapped, not taking into account the separation due to walk-off. In practice, it is useful to calculate the so-called "magic angle" α between signal and pump waves for the broadband phase matching, which is given by [12]:

$$\alpha = \sin^{-1}\sqrt{\frac{1 - v_{gs}^2/v_{gi}^2}{1 + \frac{2v_{gs}n_s\lambda_i}{v_{gi}n_i\lambda_s} + \frac{n_s^2\lambda_i^2}{n_i^2\lambda_s^2}}}. \tag{1.20}$$

An example of type I BBO NOPA pumped at 532 nm (second harmonic of Nd:YAG laser) is taken. The phase matching angle θ as a function of wavelength is pictured in Fig. 1.2. At the "magic angle" $\alpha \approx 2.43^{o}$ and the phase matching angle $\theta = 24^{o}$ between the pump wave and the optical axis, an ultra-broad amplification bandwidth is achieved, approximately spanning from 700 nm to 1000 nm.

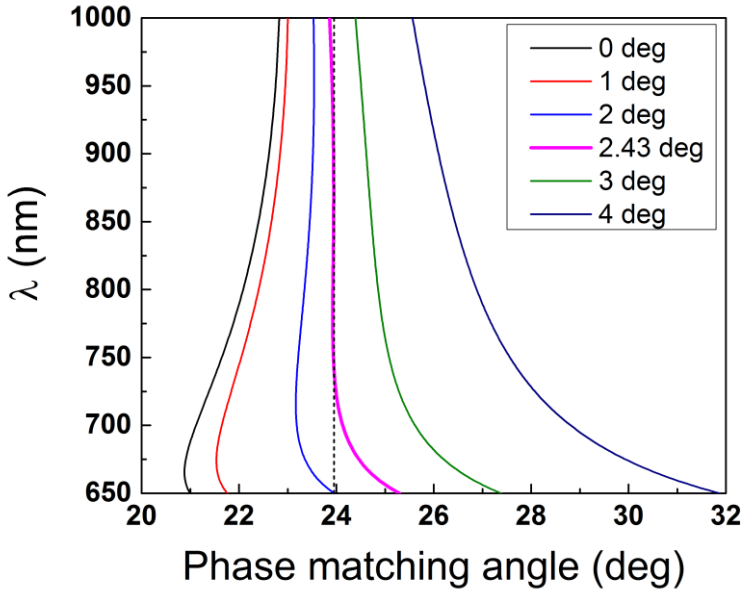

Fig. 1.2 Phase matching curves at different $\boldsymbol{\alpha}$ angles between the signal and pump waves for type I BBO NOPA pumped at 532 nm wavelength modelled using free SNLO software [65].

Assuming the case of a broadband signal and monochromatic pump, an optimal NOPA parametric bandwidth is expressed by [66]:

$$\Delta\lambda_s = \sqrt{\frac{2}{\pi}}\frac{\lambda^2}{c}\sqrt{\frac{1}{L}}\sqrt{\frac{1}{\left|\frac{\partial^2 \Delta k}{\partial \omega_s^2}\right|}}. \tag{1.21}$$

At first, noncollinear geometry was realised experimentally in broadband OPOs generating sub-20 fs pulses [67] and later implemented in WLC seeded OPAs [63]. A long lasting record of the shortest pulse was achieved from Vis-NIR NOPA by Andrius Baltuška et al. in 2002 [68]. They demonstrated 4 fs duration pulses from two-stage NOPA incorporating the programmable dispersion control.

Available high energy femtosecond pump sources, which typically produced sub-mJ level, ~100 fs duration pulses at kHz repetition rates, determined a μJ level output from ultrafast parametric amplification systems [58,63]. Such output energy was sufficient for time-resolved spectroscopic applications. A new era had begun, when advantages of chirped pulse amplification (CPA) technique in solid-state lasers [11,69] were combined with the benefits of broadband femtosecond OPA in the optical parametric chirped pulse amplification (OPCPA) scheme [70,71]. Common issues of high energy CPA systems, such as amplification bandwidth reduction due to gain narrowing, amplified spontaneous emission (ASE), accumulated phase distortions due to dispersion and nonlinearity, preventing to achieve high contrast, high peak power pulses were resolved by the OPCPA technique. In this approach, high energy, up to nanosecond duration pump pulses are coupled with chirped broadband seed in a nonlinear crystal. Since a parametric crystal is not capable of storing the inversion, the bandwidth-efficient amplification is achieved only when the ratio between the pre-stretched seed and pump pulse durations are correctly chosen [72]. Proper recompression techniques allow achieving extremely high peak powers at the table-top system output [14]. Noncollinear parametric amplification bandwidth in OPCPA system is significantly broader comparing to the conventional femtosecond laser amplifier. This provides an

opportunity to maintain few-cycle pulses. Large damage threshold of nonlinear crystals allows tight pump focusing and thus short amplification lengths, which minimises phase distortions, in order to achieve high temporal and spatial profile pulses. Excellent contrast pulses are obtained due to the absence of ASE. Furthermore, no pump absorption in the nonlinear crystal eliminates the thermal loading caused aberration issues.

Highest peak power achieved to date in a table-top design OPCPA system is 16 TW (130 mJ, 7.9 fs, 805 nm, 1 kHz) [22,73]. The shortest pulse duration obtained - 5.5 fs, considering a TW-level peak power [74]. The largest average power was produced by J. Rothhardt et al. [38] (22 W at 1 MHz repetition rate). In this system a hybrid approach was exploited, employing femtosecond Ti:sapphire laser as a seed source and a Yb-based FCPA system as a pump. Peak powers approaching PW scale (10^{15}) but at longer pulse duration from OPCPA systems were demonstrated and presented in [75,76]. Furthermore, various concepts based on OPCPA are proposed and realised for existing large scale laser facilities to leap over 1 PW peak power [77–79]. Such systems employ ultra-high intensity infrared radiation for high-harmonic generation, which allows reaching soft X-ray wavelengths and attosecond (10^{-18}) pulse durations [15] applied in attosecond spectroscopy and imaging. Even higher intensities can be used for laser-plasma interaction induced electron acceleration, which is a prospect to change the large free-electron laser facilities with table-top systems [80,81]. In recent years, a huge interest has been paid to develop high peak power and high average power OPCPA systems, where sub-ps pump sources generally based on Yb^{3+} doped active medium and thin-disk geometry are implemented [73,82]. The system of this kind operating at repetition rates from 100 to 500 kHz and delivering more than 3 μJ, two-cycle (5.7 fs) pulses was presented by M. Schultze et al. [83].

Increasing the central wavelength of high peak power few-cycle OPCPA systems is anticipated by the attosecond science community as it leads to the highest achievable HHG photon energy [16]. Advances in development of pump sources based on a variety of active media as well as novel broadband seed

formation techniques enabled to realize chirped pulse OPAs using different highly nonlinear crystals and shift the operating wavelength from NIR to MIR spectral regions. Broadband amplification at 1.5 μm was demonstrated using a femtosecond Er^{3+} fiber laser seed and picosecond solid-state Nd:YLF laser pump in a KTA-based chirped pulse OPA [33]. A different approach for seed formation was chosen by G. Andriukaitis et al. [84]. In their system, a WLC seeded KTP OPA driven by femtosecond Yb:CaF_2 amplifier produced signal pulses at 1.46 μm. Moreover, due to the implementation of a collinear OPCPA scheme this system provided utilizable high peak power few-cycle idler pulses at 3.9 μm. O. Chalus et al. [85] incorporated a difference frequency generation between the two outputs of a broadband Er^{3+} fiber laser to provide seed pulses at 3.3 μm which were later amplified in a two-stage OPCPA based on PPLN crystals pumped by sub-10 ps pulses from Nd:YVO_4 laser. Recently, D. Sanchez et al. presented the longest wavelength to date OPCPA system which produced sub-millijoule level 7 μm pulses [86]. A high energy Ho:YLF chirped pulse amplifier operating at 2 μm wavelength was developed [87] and used to pump a highly efficient OPA based on ZGP crystal.

Seed and pump synchronisation

In order to achieve stable amplification, OPCPA system requires implementation of a method to synchronise the high energy pump pulses with pre-stretched weak seed pulses. Not only the amplified pulse energy but also pulse spectrum can fluctuate when a change in pump-seed arrival time to the nonlinear crystal occurs [13]. Relative timing must be stabilised with sub-ps accuracy for 10-100 ps duration pulses [13,77].

One way to synchronise the seed and pump source lasers is active electronic stabilisation. This approach uses complicated high-frequency electronic feedback loops to phase-lock the repetition rates of two mode-locked oscillators. The relative timing can be adjusted electronically by controlling the phase between repetition rate signals [13]. The active stabilisation method was incorporated in Vis-NIR OPCPA systems, where Ti:sapphire oscillator

produced broadband seed pulses, which were later parametrically amplified using the second harmonic of high energy picosecond Nd:YAG lasers [17,88]. Furthermore, actively synchronised OPCPA systems at 1.5 μm wavelength were realised [89,90]. In these systems, Er^{3+} doped fiber laser was used as a seed and picosecond Nd-doped solid-state laser as a pump. Sub-ps timing jitter can be typically achieved using commercially available locking electronics [89].

A passive approach is based on the generation of both seed and pump pulses from a single source. Ti:sapphire oscillator is capable of producing spectrum broad enough to seed a Nd-based pump source such as a picosecond Nd:YLF laser working at 1053 nm wavelength [23]. Incorporation of photonic crystal fiber pumped by Ti:sapphire laser can be used to produce optical solitons at 1064 nm via Raman effect caused soliton self-frequency shift [91]. However, such nonlinear frequency conversion process is sensitive to the input energy and may prevent from the stable long-term operation. Moreover, an important drawback of the described passive method is a very low, pJ-level seed energy causing a significant amount of ASE to be generated in the regenerative amplifier which results in a limited contrast of amplified pulses. An improvement of the contrast can be realised by constructing an additional preamplifier [92]. Even more sophisticated alternative method of passive synchronisation was demonstrated by several groups [93,94]. Here the synchronisation of two mode-locked lasers was achieved by injecting one laser pulse into another laser cavity. Due to cross-phase modulation effect between the two co-propagating pulses of different wavelengths, the spectral shift is induced. If the cavity exhibits total negative group velocity dispersion, the change in round-trip group delay for the initial cavity pulse occurs, which leads to the self-synchronisation [94]. This scheme was realised with Ti:sapphire seed injected into a Yb-based fiber CPA pump system and proved to have a very low, femtosecond jitter. However, to implement the method experimentally, rather strict conditions regarding the pump power and laser repetition rate must be fulfilled.

Further technological challenges emerge when the OPCPA system is pumped by ultrashort picosecond and sub-picosecond pulses. For such system, an additional timing jitter occurs due to the air turbulences, temperature drifts and mechanical vibrations of optical components [24]. Implementing an active stabilisation technique require a closed loop scheme with a delay element, for example, a piezo stage, which allows adjusting the optical path between seed and pump pulses. The time delay is generally measured using a nonlinear process, because a direct measurement with conventional photodiodes is impossible in femtosecond time scale. Various detection and delay control techniques allowing to achieve a timing jitter of few femtoseconds are presented in [24,25,35]. A passive synchronisation method demonstrated by R. Riedel et al. [35] is the closest approach to the one described in this thesis. A single femtosecond fiber oscillator was used to generate pulses for the Yb-based pump amplifier. A small fraction of the pump pulses generated white-light supercontinuum seed, which was later amplified by the remaining part of the pump. The optical path length of seed and pump pulses was reduced to less than 4 meters. The measured timing jitter of 7 fs originated due to the WLG process.

Dispersion control

An accurate phase compensation for parametrically amplified broadband pulses was a challenge since the early development of NOPA schemes. While a conventional prism pair compressor was generally used to compensate the residual material dispersion in the collinear OPAs [57], few-cycle NOPAs and later OPCPA systems required techniques which allow managing dispersion up to the 4^{th} or even the 5^{th} order [12,13].

A single-stage NOPA scheme, where the light path through the material was minimised, and a pair of low dispersion glass (fused silica, BK7) prisms were used for compression, allowed to obtain 10-15 fs duration pulses in visible [64,95] and slightly less than 10 fs in Vis-NIR wavelength ranges [96]. Implementation of thin prism sequence compressor reduced the amount of accumulated TOD, which helped to achieve sub-8 fs pulses at the system

output [97]. Opportunities for a more precise high-order dispersion control were given with the proposed prism-grating and prism-chirped mirror compressor combinations [98,99]. These combinations incorporated with adaptive compression techniques and programmable dispersion control led to the shortest output pulse durations from a NOPA system [68,100]. However, the throughput of such compressors was low and the dispersion control range was limited to the exact arrangement of optical components.

Since the invention of CPA [69], a variety of stretcher-compressor schemes were proposed. In the first demonstration of CPA, 1.4 km length optical fiber was used as a stretcher and a pair of diffraction gratings in a double-pass configuration as a compressor. This technique is still applicable in FCPA systems, in order to achieve sub-ps duration compressed pulses [101]. Compression to shorter pulses was limited due to the effects of uncompensated TOD, as both fiber stretcher and grating compressor accumulate TOD of the same sign. In order to compensate higher-order dispersion, self-compensating stretcher-compressor schemes were developed, which were mainly based on the invention of positive GVD exhibiting grating arrangement by O. E. Martinez [102,103]. The usage of the lens system in the Martinez-type scheme made this stretcher-compressor design unsuitable for shorter than 100 fs pulses, due to spatial aberrations and lens material dispersion. Therefore, all-reflective optics designs were proposed [104], from which the most promising was the aberration-free stretcher scheme based on the Offner telescope design [105,106] described in detail in Chapter A.4. This implementation allowed the pulse stretching up to 1 ns and compression down to sub-30 fs using a conventional grating compressor [107] in a TW-class peak power Ti:sapphire CPA systems [108–110]. With the help of adaptive optics such as spatial light modulators and deformable mirrors [111] even less than 10 fs duration pulses were achieved [112]. Although these schemes are low-loss when efficient high line density diffraction gratings are used, high stretching ratios of ultra-broadband pulses require large spherical optics with accurate and perfect quality surfaces [113].

In contrast to the CPA systems, OPCPA has an advantage due to the small interaction length, leading to the less challenging task of matching the dispersion of stretcher and compressor. Self-compensating stretcher-compressor methods usually incorporating Offner-type pulse expander were also proposed and used in the OPCPA systems [78,89,114], as well as in the work of this thesis [96]. However, few-cycle pulse compression is still a challenging task, which requires implementation of adaptive techniques – spectral phase shapers. Computer controllable liquid crystal spatial light modulators used together with a pulse phase reconstructing devices were implemented in the OPCPA system to produce TW-level few-cycle pulses in Vis-NIR wavelength range [18,115]. The other widely applied alternative is acousto-optic programmable dispersion filtering (AOPDF) [116]. It was already used more than a decade ago to provide multi-millijoule few-cycle pulses in Vis-NIR range [17] and around 2 μm wavelength [117]. AOPDF devices are very lossy, exhibiting ~10% or less diffraction efficiency [20,117]. Thus, the OPCPA scheme requires an additional amplification stage because of a low-energy seed after the pulse stretcher to maintain a sufficient pulse contrast. Furthermore, the compensation range of these phase shapers is generally limited.

Despite the grating based pulse stretching-compression techniques, lately, a down-chirping stretcher and up-chirping bulk material glass compressor scheme was chosen in a few-cycle OPCPA systems [17,20]. The advantage of this approach is that the compressor becomes highly transmissive. In order to achieve more adjustable dispersion control, the combination of AOPDF with a grism (prism-grating) pair stretcher [118,119] can be used in such scheme [20].

From the other point of view, as the pump pulse duration sets the requirements for the seed temporal stretching ratio which is directly related to the residual high-order dispersion accumulation, a reduced complexity stretcher-compressor techniques could be realised for the ultrashort pump OPCPA systems. High intensity Yb-based picosecond and sub-ps pump lasers have a promising future in that respect [73,82,120,121].

Supercontinuum generation. Few-cycle regime

Intense ultrashort pulse propagation through a transparent medium can result in significant spatio-temporal changes due to the strongly nonlinear interaction. One of the most applicable effects is an extreme broadening of the pulse spectrum called supercontinuum generation (SCG). First discovered and demonstrated in BK7 glass [122], the effect of SCG was observed in many different media, such as liquids, gases and microstructured fibers [123,124]. Tens of femtoseconds duration pulses coupled into a photonic crystal fiber cause an octave-spanning spectral broadening, which can be used to produce few-cycle, sub-5 fs pulses [125]. However, it was shown that SCG by longer pulses resulted in a highly distorted spectrum and fluctuating energy output [124]. Smooth and high spatio-temporal coherence supercontinuum is generated using bulk materials [126–128]. Femtosecond NIR laser driven SCG sources based on a bulk few millimeter thickness solid-state dielectric medium eventually became popular in spectroscopy and ultrafast laser technology applications [128].

A variety of effects related with a process of femtosecond filamentation provoke the SCG in bulk dielectric medium. The interplay between self-phase modulation, self-focusing, four-wave mixing, multiphoton absorption and plasma generation can cause an extreme spectral broadening to shorter (blue-shift) and longer (red-shift) wavelengths of the exciting pulse [123,129]. This process in normal dispersion regime was well described by A. L. Gaeta [130]. An intense ultrashort pulse is strongly reshaped due to space-time focusing and self-steepening effects leading to optical shock formation and pulse splitting into two. The resulting leading and trailing sub-pulses are responsible for spectral red-shift and blue-shift respectively. The numerical inclusion of multi-photon absorption and electron plasma generation showed a very important role of both effects in the formation of the supercontinuum. In fact, these two effects can be decisive for broadband SCG, which was experimentally demonstrated by A. Brodeur et al. [131]. They had used different solid and liquid materials and proved that self-focusing is a triggering effect of SCG as the significant spectral

broadening was observed when the critical power of self-focusing was exceeded [128]:

$$P_{cr} \gtrsim \frac{0.15\lambda_0^2}{n_0 n_2}, \tag{1.22}$$

where λ_0 is the center wavelength, n_0 and n_2 are linear and nonlinear refractive indexes respectively. Moreover, their investigation revealed that SCG process depends on the material bandgap E_{gap}. It was shown that the blue-shift increases with the increasing bandgap and is inversely proportional to the nonlinear refractive index. These effects are related to the multi-photon excitation (MPE) induced by the catastrophic collapse of the pulse. The generation of free-electron plasma stops the self-focusing leading to a sudden negative change of the refractive index and a phase jump. This results in a large blue-shift. It was determined experimentally, that only above 3-photon MPE ($E_{gap}/\hbar\omega_0$) the ultra-broadband SCG was generated. If the material bandgap does not satisfy this condition, self-focusing is stopped by a free-electron defocusing at relatively low intensities and not enough nonlinear phase is accumulated for SCG. Furthermore, this leads to another conclusion, that SCG induced by longer wavelength pulses causes a larger blue-shift, which was demonstrated by M. Bradler et. al [128]. They used a YAG crystal and Ti:sapphire laser driven NOPA to change the wavelength from 1100 to 1600 nm. A much broader spectra than obtained with Ti:sapphire fundamental harmonic were achieved tuning the pump pulses to the long wavelength side. Moreover, the blue-shift cut-off wavelength remained almost the same at all tuning range. Ultrabroadband SCG with multi-octave blue-shift was demonstrated by J. Darginavičius et. al [132] using few-cycle pulses at 2 μm focused in wide-bandgap bulk solids in anomalous dispersion regime. Supercontinuum spectra spanning from 450 nm to more than 2500 nm were measured experimentally.

Properties of most popular solid-state dielectric media used for SCG are presented in Table 1.1 according to [128].

	Sapphire	*YAG*	*CaF_2*	*YVO_4*
n_2 [10^{-16} cm^2/W]	3.1	6.9	1.24	15
Bandgap [eV]	6.5	5.9	9.2	3.6
Blue-shift cut-off [nm]	440	470	280	550

Table 1.1 Relevant properties of popular SCG crystals. The blue-shift cut-off wavelength was measured pumping 3 mm thick Sapphire and 4 mm thick YAG, CaF_2 and YVO_4 plates by 150 fs pulses from 1 kHz repetition rate Ti:sapphire system (775 nm center wavelength). All values are taken from [128].

The largest blue-shift is observed in CaF_2, which makes this crystal suitable for the applications, where UV region is required [133,134]. However, it has to be rotated to avoid permanent damage even at low repetition rates. The most common solid-state dielectric medium for SCG is sapphire crystal. It is extensively used in supercontinuum seeded few-cycle OPA and OPCPA systems [20,68,135] and spectroscopic applications [136]. A laser host material YVO_4 showed promising results [128], as it requires approximately one order of magnitude lower pump energy for sufficient and stable SCG and can be applicable in high repetition rate but low pulse energy lasers systems. YAG crystal is known for large supercontinuum red-shift and higher spectral brightness above 1100 nm wavelength in comparison to sapphire and CaF_2. Supercontinuum extent to IR region is not only required by spectroscopic applications but is beneficial for efficient HHG [15]. For this purpose YAG-based SCG was incorporated in a few-cycle MIR OPCPA system [84].

Possibilities to control the supercontinuum red-shift was studied theoretically and experimentally by A. Dubietis group [129]. They observed the dependence of a red-shift to the pump beam focus and demonstrated that in loose focusing conditions enhanced spectral broadening to longer wavelengths is achieved. While this is not the case for the maximum blue-shift, supercontinuum spectral distribution to shorter wavelengths can be affected by the arrangement of the optical components, particularly the distance from the SCG medium front surface to the focus [137]. Therefore, correct experimental conditions must be prepared for a proper SCG realisation.

Development of high energy picosecond and sub-ps pump sources for OPCPA systems inspired studies of SCG in bulk solid-state dielectric media using longer pulses. In the femtosecond regime critical plasma density which leads to a catastrophic damage to the material is not reached even for powers several times above the threshold power of SCG [130]. In a longer, picosecond to nanosecond pulse regime avalanche ionisation is a dominant effect, due to the multiple free-electron absorption during the single pulse propagation. Therefore, a critical plasma density can be achieved before the SCG. Recently, an extensive study was carried out in order to demonstrate the dynamics of SCG process driven by 1.3 ps, 1055 nm pulses [138]. It was shown that SCG mechanism is significantly different compared to a femtosecond regime. A broadband supercontinuum spanning from 480 to more than 2000 nm with a multi-pulse spatio-temporal structure was formed at the output of YAG crystal, with two distinct sub-pulses responsible for blue and red shifts. These results are useful for designing ultrashort pump pulse OPCPA systems, without separate broadband seed source by generating supercontinuum directly from the pump laser [139].

Broadband seed formation schemes employing SCG in a few-cycle OPCPA systems can be used to preserve the electric field phase underneath the envelope of a few-cycle pulse. NIR OPCPA systems often provide less than 10 fs duration pulses with only a few cycles of the carrier wave (2.66 fs corresponds to 1 optical cycle at 800 nm). Therefore, the electric field can no longer be properly described by its intensity envelope. Few-cycle pulse shape depends on the phase between envelope and carrier wave, which is known as a carrier-envelope phase (CEP). Shot-to-shot CEP preservation and control plays a crucial role in HHG, determining the electric field strength for the attosecond XUV pulse generation. It was demonstrated experimentally, that $\pi/10$ level CEP drift has an immense effect on the temporal shape and spectral characteristics of the XUV pulses [140]. Conventional electronics does not provide the required precision of hundreds of attoseconds in timing between the carrier wave and the pulse envelope. Thus, the complex active stabilisation approaches were

developed [141]. A passive CEP control method was proposed by A. Baltuška et al. [142]. This group theoretically and experimentally proved that it is possible to parametrically generate an idler wave which is independent to the phase offset of the input waves. Knowing that supercontinuum radiation preserves the phase of the driving pulses [128,141], white-light seeded OPA can be the source of CEP-stable few-cycle pulses. In recent years, passive CEP stabilisation schemes are already implemented in high energy NIR OPCPA systems [141,143,144].

Femtosecond fiber chirped pulse amplification

Fiber lasers have many advantages compared to solid-state systems in terms of compactness, simplicity, long-term stability and thermo-optical properties. Emerging practical applications of ultrafast laser systems require persistent advancement of ultrashort pulse sources. Therefore, applied research field of femtosecond fiber lasers is highly active. Although the history of practical optical fiber implementation dates to the middle of the 20th century and is related to applications in medicine and optical communications, fiber lasers became very attractive when high brightness laser diode pump sources and cladding pumping technique were developed [145,146].

To this day, solid-state femtosecond seed sources such as Yb:KGW oscillators are often preferred in high peak power fiber laser systems [146,147]. On the other hand, various schemes of ultrafast fiber oscillators were demonstrated and successfully commercialised. Environmentally stable, all-in-fiber laser can be realised by passive mode-locking based on a semiconductor saturable absorber mirror (SESAM) [148]. With management of intracavity dispersion, fiber lasers producing transform-limited pulses down to few hundred femtoseconds duration were demonstrated [149,150]. However, SESAM mode-locked oscillators require different absorber parameters for each laser design, especially the different gain medium. Furthermore, long-term degradation issues of the absorber can often be encountered [151]. Therefore, other mode-locking techniques such as nonlinear polarisation evolution (NPE), nonlinear amplifying mirror (NALM) were proposed and investigated [152,153]. These methods can

be realised using all-normal dispersion components, providing strongly chirped and relatively energetic pulses which are compressed externally [154]. The shortest pulses to date from all-in-fiber oscillator at 1 μm wavelength were achieved by Z. Zhang et al. [155]. They incorporated anomalous dispersion photonic crystal fiber in a ring cavity together with NPE technique and measured 42 fs pulses after dechirping.

Femtosecond pulse energy scaling in single-mode fiber amplification systems become a challenging task because high-peak power pulses are confined in a small fiber core, and nonlinear effects are triggered leading to the distortion of the pulses. Designing the ultrashort pulse fiber laser system self-phase modulation (SPM) and stimulated Raman scattering (SRS) effects must be considered. SPM causes spectral modulations, so that pulse phase distortion arises from the intensity dependent refractive index (Chapter A.1). Raman spectral components will be generated when the peak power of the pulse reaches the SRS threshold power [146,156]:

$$P_{th} \approx \frac{16A_{eff}}{g_{Raman}L_{eff}}, \tag{1.23}$$

where $A_{eff} \approx \pi(MFD)^2/4$ is effective fiber mode area expressed using mode field diameter (MFD), g_{Raman} is the Raman gain coefficient and L_{eff} is effective interaction length, which is shorter compared to the fiber length due to the losses in fiber. SRS originates from the light interaction with vibrations of glass lattice [145]. Above SRS threshold, signal is absorbed and its spectrum is shifted to form a Stokes wave. Powerful first Stokes wave can generate higher-order waves in a cascaded SRS and thus the initial pulse spectrum is greatly distorted. Generally, combination of two approaches can be used in order to maximize the output peak power from fiber amplifier: temporal pulse stretching (CPA) and expansion of the fiber core with a single mode preservation.

A common design strategy for high energy ultrafast fiber laser is based on CPA. Sub-picosecond pulses, delivered by fiber or solid-state oscillator, are stretched up to 1000 times due to the chromatic dispersion, amplified in an active fiber and when recompressed. In this way, the peak power of the pulses is

significantly reduced during the amplification in fiber, and nonlinear effects are suppressed. To increase the pulse energy at fixed average power level, an optical down-counter, such as an acousto-optic modulator, which reduces the initial repetition rate of the oscillator (~50 MHz) to ~1 MHz or lower can be inserted into the scheme. Conventional ultrafast fiber amplifiers with core diameters up to approximately 10 μm can deliver ~1 μJ pulse energies [145]. For a variety of applications, for example, imaging of biological tissues, ophthalmology, fluorescence microscopy, etc. such pulse energy is sufficient [145]. However, for many other applications, such as pumping amplifiers, micromachining, the higher ultrashort pulse energy is required. For example, it was demonstrated that excellent hole quality and faster ablation speeds can be achieved with femtosecond pulses, particularly in combination with pulse bursts [145,157].

Development of large-mode-area active fibers gradually led to millijoule level energy pulses. An expansion of the fiber core diameter is effective and can be practically realised up to ~100 μm [145]. Fibers with such core diameters are already multi-mode, but the fundamental mode propagation is maintained by various methods of higher-order mode (HOM) suppression. The earliest techniques were based on mode matching at the input of the fiber and HOM filtering due to the fiber bending [158,159]. An insertion of additional cores which guide HOM and prevent from propagation in the central core was proposed by A. Galvanauskas group [160]. Due to its internal structure, the fiber was named as chirally-coupled-core (CCC) fiber. A Yb-based FCPA system was demonstrated using 33 μm core diameter CCC fiber. Over 100 μJ pulse energy was achieved at 100 kHz repetition rate [101]. CCC fibers with up to 60 μm core diameters were later demonstrated [46]. Alternative techniques are based on photonic crystal fiber design in which a core is surrounded by the pattern of air holes. A holey fiber structure was used in leakage channel and large-pitch active fibers to create a large loss for HOM and high throughput for the fundamental mode [161,162].

In contrast to a conventional approach of scaling the fundamental mode area and therefore increasing the output energy from FCPA systems, a different

strategy based on signal propagation and amplification in HOM fibers was proposed and developed [163]. Fundamental aspects and advantages of this technology was well described by S. Ramachandran et al. [164]. Few years ago, X. Peng et al. demonstrated an Er-based FCPA system in which HOM fiber with 6000 μm^2 effective area was used [165]. Conversion from $LP_{0,1}$ mode of both pump and signal to $LP_{0,11}$ mode before the amplification and reconversion back to the fundamental mode was performed by using long period fiber gratings. Measured output energy of less than 500 fs duration pulses was 300 μJ at 1.55 μm wavelength and the characterized spatial beam quality was nearly diffraction limited.

Highest pulse peak powers to date were achieved in FCPA systems based on spatio-temporally divided pulse amplification (DPA) and coherent beam combining (CBC). An initial pulse can be divided and later combined using polarisation beam splitters and actively controlled piezo temporal delay lines with a feedback loop [166]. Moreover, a passive approach which incorporated birefringent crystals with large polarisation mode delay and CBC using backward propagation after a double-pass through Faraday rotator was demonstrated [167]. One system comprised of 8 separate 64 μm mode field diameter large-pitch active fibers, pumped by 250 W diodes at 976 nm and delivered 1 mJ, 260 fs pulses with 91% combining efficiency [147]. The average power of the system was 1 kW. A 16-channel laser is being developed with expected 2 kW average power and 10 mJ pulses. The second system used the same spatial division scheme with an additional pulse temporal splitting into 4 replicas and achieved 12 mJ pulse energy with 700 W average power and 78% combining efficiency at the output [168]. As a future prospect, CBC architectures based on multi-core fiber amplifiers are extensively investigated and developed [169,170].

A set of initial pulse parameters and amplification conditions leads to different pulse propagation regimes which can also prevent or compensate the SPM caused ultrashort pulse phase distortion. One of the proposed regimes is the self-similar propagation of parabolic pulses in the presence of SPM leading

to the linear chirp evolvement across the pulse [171,172]. The pulse shape is preserved as the temporal duration increases along the fiber and the linear chirp can be compressed by simple compressor setup. Self-similar propagation is perturbed by the limited spectral amplification bandwidth and finite length of the active fiber which results in low-intensity pulse wings formation and also restricts the amount of tolerable SPM [47,146]. A few years ago, self-similar pulse evolution inside a laser cavity was demonstrated. The gain-bandwidth limitation to pulse duration was overcome and broad spectrum (~200 nm) sub-30 fs dechirped pulses were obtained [173]. Another amplification regime is known as cubicon pulse formation [47]. Amplification at highly nonlinear conditions can be tolerable for a strongly chirped self-similar like pulses which inherit a cubic spectral and temporal shape in FCPA system. In this regime, SPM can induce a negative sign TOD which leads to the flattening of the nonlinear pulse phase during the compression and shorter output pulses [47,101]. However, the compressed pulse contrast is still limited by a large amount of accumulated nonlinear phase.

Although pulse stretching and compression techniques in FCPA systems evolved greatly since the first demonstration of CPA, some of the initial schemes are still implemented. One of the simplest approaches – TOD mismatched fiber stretcher and diffraction grating compressor. Exploiting a cubicon-like pulse regime in a mismatched configuration, high quality 100 μJ, 270 fs pulses were obtained by Zaouter et al. [174]. Self-compensating schemes similar to the ones in OPCPA systems including high-efficiency diffraction gratings were also applied in order to achieve high energy femtosecond pulses [175]. A variety of all-in-fiber configurations were developed. Chirped fiber Bragg gratings (CFBG) were used for stretching and compression [176]. In later years, photonic band-gap fiber (PBGF) compressors showed excellent experimental results. J. Limpert et al. demonstrated 100 fs pulses at 6 W average power with 73% compression efficiency using air-guiding PBGF compressor [177]. Since all-in-fiber schemes are limited to μJ-level pulse energies due to nonlinearities, a large aperture alternative to chirped fiber Bragg grating is a chirped volume

Bragg grating (CVBG). This technology is rapidly improving in recent years, in the direction of expanding the available bandwidths and stretching ratios [178]. Moreover, issues regarding the CVBG induced group delay ripples are also being solved.

Pulse shortening beyond the bandwidth limit of the laser medium can be achieved by applying the methods of nonlinear compression. S. Hadrich et al. used a combination of Kr-gas-filled hollow-core fiber to broaden the pulse spectrum extremely and chirped mirrors to compress the pulses [179]. They obtained 540 μJ, 26 fs pulses at 250 kHz repetition rate at the system output. The efficiency of the nonlinear conversion stage was 49%. It was shown experimentally that laser system with such parameters is suitable for a high-harmonic generation [180]. However, for attosecond science, studying the processes on the time scale of electronic motion requires isolated attosecond pulses to be generated. Such requirement is only fulfilled by CEP-stable few-cycle pulse lasers [145,181]. Recently, as an intermediate goal of the currently constructed extreme light infrastructure attosecond light pulse source (ELI-ALPS), J. Limpert group demonstrated 6.3 fs, 170 μJ pulses at 216 W average power [182]. They used 660 W femtosecond FCPA system with externally constructed two nonlinear compression stages based on noble-gas-filled capillaries. This system delivers highest average power few-cycle pulses to date and outperforms the highest average power OPCPA system [38] by about an order of magnitude. The obtained results are a perfect example that current FCPA technology is at the frontier of high peak and high average power ultrafast laser systems. Together with emerging solid-state laser and OPCPA technologies it determines the future of modern laser science and drives to new discoveries.

2 Femtosecond OPCPA front-end based on picosecond fiber laser seed

This chapter is dedicated to discussing proposed and experimentally demonstrated two patented solutions for the femtosecond OPCPA systems. In the first section, experimental realisation of a novel all-in-fiber laser seed source is presented. This device generated passively synchronised dual-wavelength pulses for femtosecond seed and picosecond pump lasers for high energy OPCPA system. On the basis of this work, a unique femtosecond OPCPA front-end was designed and experimentally realised. This is discussed in the second section.

2.1 Laser source for generation of optically synchronised dual-wavelength ultrashort light pulses

Material related to this chapter was published in A2 and described in patent P1

To realise all-optical synchronisation of femtosecond OPA and picosecond OPCPA stages (Fig. 2.1.1) while providing enough seed for the generation of high contrast pump pulses, a dual-output fiber front-end was designed.

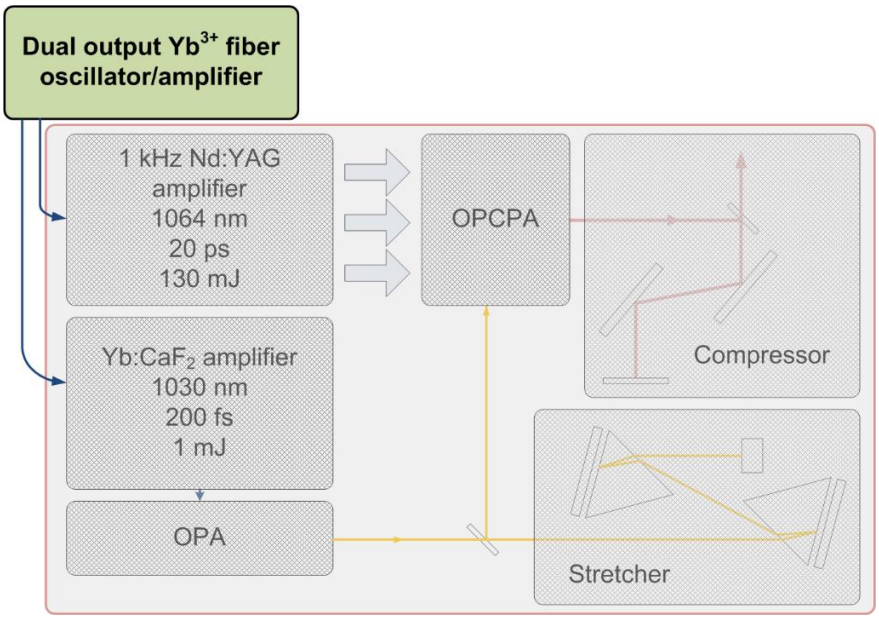

Fig. 2.1.1 Layout of an OPCPA system relevant to the one published in [84]. Related to this work dual-output fiber oscillator amplifier is highlighted while the 1 kHz Nd:YAG power amplification system and the rest of the OPCPA system are shaded.

The fiber laser design and pulse formation therein are based on effects of dispersion and Kerr nonlinearity acting on the ultrashort pulse, which propagates along the optical fiber. In order to prove and explain the concept, a simple numerical modelling was performed. Effects of GVD, TOD and Kerr nonlinearity were included using standard parameters for single-mode polarisation maintaining (SM PM) fiber (Chapter A.1). The initial pulse parameters were chosen according to the experimental conditions.

First, 3 ps duration Gaussian pulse centered at 1047 nm wavelength was propagated through a 25 m length fiber. The pulse energy and fiber length were chosen to maintain a sufficient spectral broadening due to SPM, generating enough spectral components around 1030 nm and 1064 nm, which were the central wavelengths of femtosecond OPA seed and picosecond OPCPA pump lasers respectively. Pulse envelope and spectrum after propagation in the fiber are pictured in Fig. 2.1.2. A close to flat-top pulse shape was formed due to the interplay between GVD and nonlinearity effects [156]. The temporal phase derivative showed a quasi-linear instantaneous frequency across the pulse (Fig. 2.1.2(a), green dashed curve).

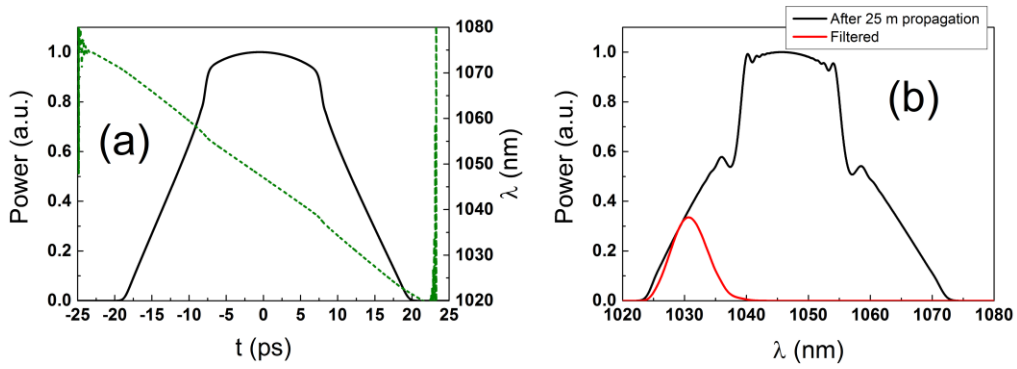

Fig. 2.1.2 Ultrashort pulse after propagation through 25 m of SM PM fiber: (a) pulse envelope (black curve) and instantaneous frequency (green dashed curve) expressed in the units of wavelength; (b) pulse spectrum (black curve) and filtered part at 1030 nm wavelength (red curve).

Narrow spectrum pulses centered at 1064 nm wavelength can be easily filtered from the broadened spectrum using a narrowband FBG. A broadband Yb:CaF_2 amplifier requires seed, which spectrum corresponds to less than 300 fs pulse duration. Moreover, seed pulses must have a linear chirp which could be

compensated by the diffraction grating compressor. To find out if such pulses can be produced by filtering a short wavelength side of the broadened spectrum, 8 nm width Gaussian filter function centered at 1030 nm was used in the calculation. The filtered part exhibited linear chirp across the FWHM of the intensity function (Fig. 2.1.3(a)). Then, compression with 1000 grooves/mm line density diffraction gratings was simulated. The resulting pulse envelope is shown in Fig. 2.1.3(b). Although the effect of residual TOD was visible, pulse duration was close to the transform-limit and less than 300 fs.

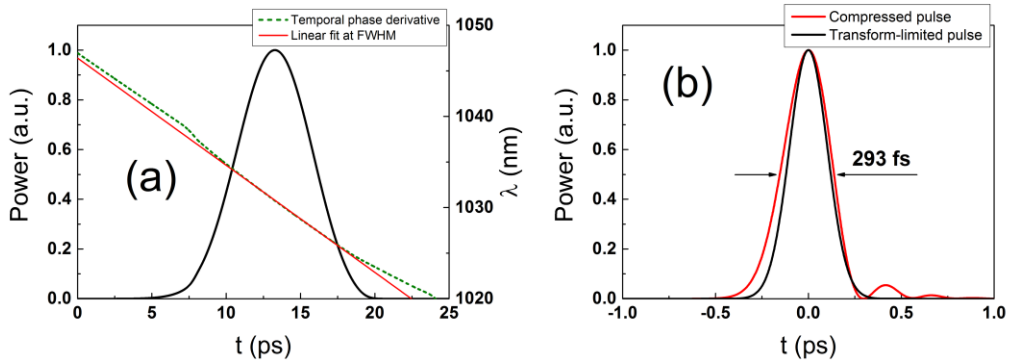

Fig. 2.1.3 Compression of the filtered pulse: (a) pulse envelope before compression (black curve) and instantaneous frequency (green dashed curve), fitted using linear function at FWHM of the intensity distribution (red curve); (b) compressed pulse envelope (red curve) compared to the transform-limited pulse (black curve).

The described concept was realised experimentally. The front-end consisted of a passively mode-locked fiber oscillator, a double stage fiber amplifier, and spectral and temporal pulse formation chain (Fig. 2.1.4). SM PM fiber was used in all parts of the system.

A chirped fiber Bragg grating (CFBG1) and a semiconductor saturable absorber mirror (SESAM) were employed as end mirrors of the resonator of the oscillator. CFBG1 with ~60% reflectivity at 1047 nm, 25 nm spectral bandwidth and anomalous dispersion of 4.5 ps/nm was implemented for the dispersion management of the resonator. A free-space long-pass filter (LPF) placed in the collimated beam before the SESAM provided wavelength tuning of the oscillator. The central wavelength of the oscillator was set to 1047 nm by adjusting the angle of incidence on the LPF.

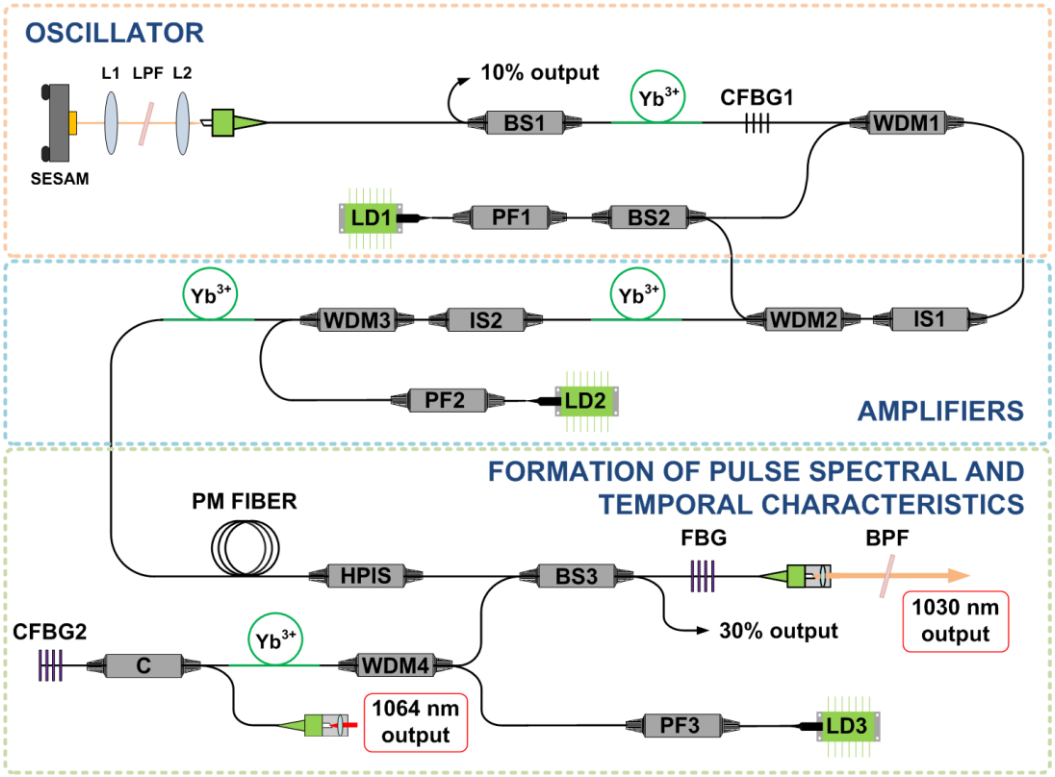

Fig. 2.1.4 Principal scheme of the dual output fiber front-end. SESAM - semiconductor saturable absorber mirror, L1,2 – spherical lenses, LPF – long-pass filter, BS1-3 – beam splitters, CFBG1,2 – chirped fiber Bragg gratings, WDM1-4 - wavelength division multiplexers, IS1,2 – isolators, HPIS – high power isolator, FBG – fiber Bragg grating, PF1-3 – band-pass filters, BPF – free space band-pass filter, LD1-3 – laser diodes, PM FIBER – polarization maintaining fiber, C - circulator.

The SESAM placed on a mirror mount for angular adjustment and a translation stage for optimisation of position along the beam, enabled self-starting passive mode-locking of the oscillator. Laser radiation was focused on the SESAM by a 12 mm focal length lens to a spot of 7 μm in diameter. The oscillator was pumped through a wavelength division multiplexer (WDM) and CFBG1 by a 20% fraction (about 80 mW) of an output of a laser diode (LD1). LD1 was protected from back returning pulsed radiation by a band-pass filter (PF1). Oscillator at a repetition rate of 60.3 MHz generated 2.9 ps pulses, which were close to transform limit. The pulse spectrum shown in Fig. 2.1.5 was typical for a soliton mode-locked fiber laser (see Chapter A.2). A large number of spectral sidebands were visible in logarithmic scale. The intensity of sidebands was not suppressed by CFBG1 filtering, as the reflection bandwidth of the grating was much wider than the pulse spectrum.

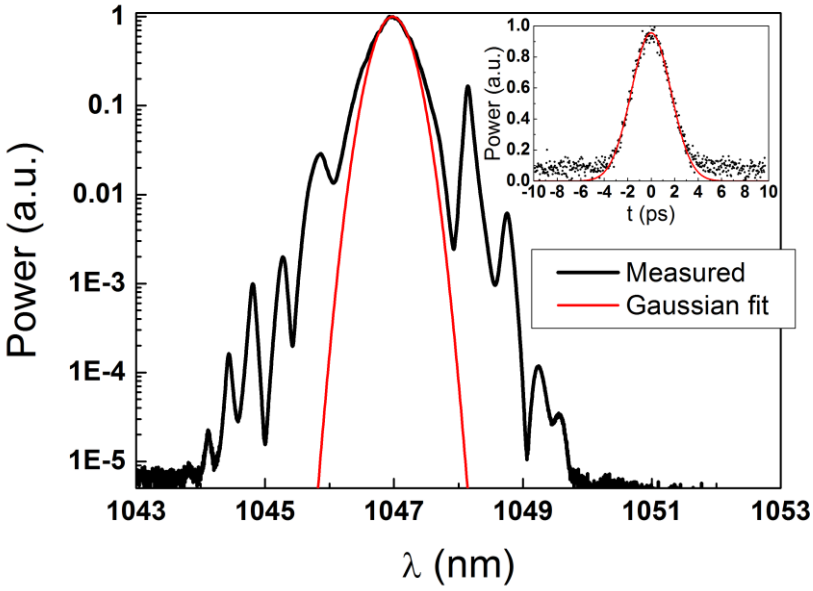

Fig. 2.1.5 Experimentally measured spectrum of the fiber oscillator. The measured autocorrelation function is pictured in the inset.

Average output power after the CFBG1, which served as an output coupler, was in the order of 3.5 mW. 10% of the output power reflected by a beam splitter BS1 (10/90) was used for synchronisation of the system to the clock of the master oscillator.

Pulses from the oscillator were directed through the WDMs and isolators to a two-stage amplifier. The first amplification stage was pumped by the remaining 80% output (320 mW) of LD1, while the second amplification stage was pumped by the high power (900 mW) single-mode laser diode LD2. After two stages pulses were amplified to 7.2 nJ pulse energy which corresponded to 435 mW of average power. The spectrum of amplified pulses was broadened due to SPM in an 11 m long passive fiber. Resulting spectrum spanning from 1025 nm to 1067 nm is presented in Fig. 2.1.6. It covered gain spectra of both Yb^{3+} and Nd^{3+} doped laser media. Duration of the spectrally broadened pulses was measured to be around 15 ps.

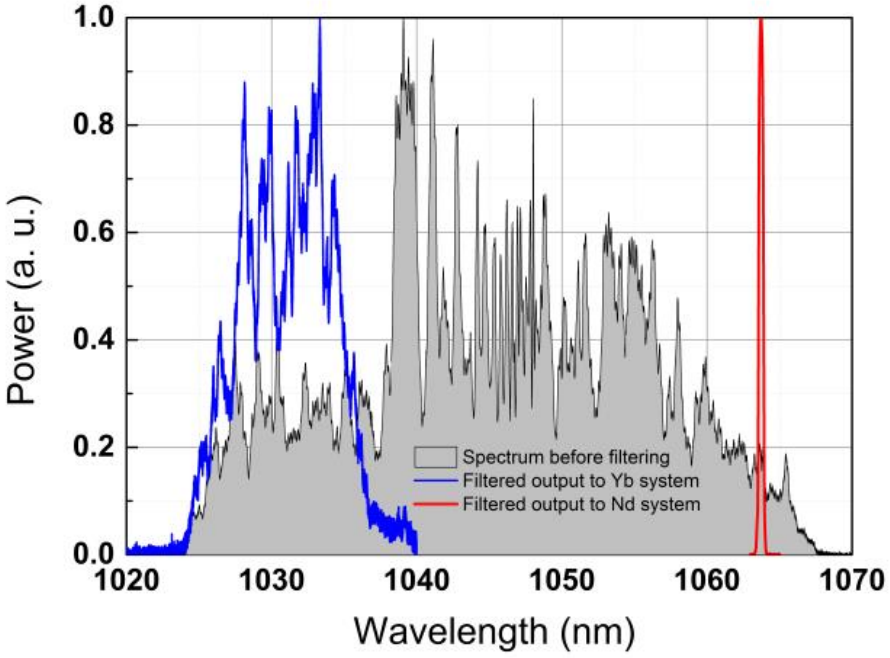

Fig. 2.1.6 Normalized spectra detected before and after filtering. Grey (filled area) – after spectral broadening in 11 m of fiber (30% Output in Fig. 2.1.4); blue – output to 1030 nm after filtering with bandpass filter; red – output of 1064 nm channel.

Spectrally broadened pulses were then divided by a 30/70 ratio beam splitter (BS3) with 30% fraction being dumped and 70% fraction being passed to a narrowband FBG2, which back-reflected 0.4 nm spectral bandwidth around the central wavelength of 1064 nm for further amplification. The spectral fraction centered around 1030 nm passed FBG for seeding femtosecond 1030 nm amplifier. A free-space band-pass filter (BPF) was used to reject spectral components, which would not be amplified in Yb^{3+} doped active medium. Output power after the BPF was measured to be 27 mW which corresponded to 450 pJ pulse energy. Spectral bandwidth of about 10 nm, and pulse duration of 4 ps indicated that the 1030 nm pulses were chirped. 10 nm bandwidth achieved through the SPM in fiber supported <300 fs pulse duration. In order to check the compressibility, ultrashort pulses from this output were externally compressed using a pair of 1000 grooves/mm line density diffraction gratings in a double-pass configuration. The measured autocorrelation trace is pictured in Fig. 2.1.7. The corresponding pulse duration was 305 fs at FWHM when fitted with

Gaussian function. The autocorrelation trace exhibited a large pedestal due to the uncompensated TOD of both fiber and grating compressor.

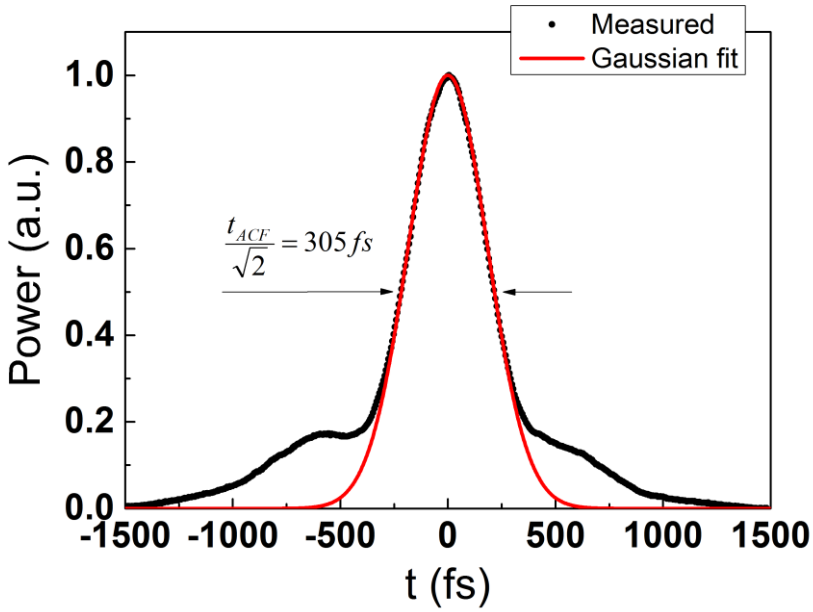

Fig. 2.1.7 Autocorrelation trace of the compressed pulses from the broadband 1030 nm output of the dual-wavelength source. The retrieved compressed pulse duration was 305 fs at FWHM when fitted with Gaussian function.

Narrowband pulses at 1064 nm were back reflected by FBG and coupled through 30% branch of the beam splitter BS3 to WDM4. An average power (~0.1 mW) and energy (~1.6 pJ) was too low for efficient seeding of a RA based on Nd-doped laser crystal. In order to boost pulse energy an additional fiber amplification stage, in which 1064 nm pulses were amplified by a factor of 100 to 150 pJ pulse energy, was installed. The resulting energy of 150 pJ was sufficient for high contrast operation of the solid-state regenerative amplifier [21]. The duration of the pulses was measured to be 8.5 ps with ~0.4 nm spectral bandwidth.

Chirped 1064 nm pulses were further stretched using CFBG2 with 0.3 nm spectral bandwidth at FWHM and -2000 ps/nm dispersion parameter. The duration of the resulting pulses was ~520 ps.

Conclusions

In this work, a novel optically synchronised dual-wavelength laser source was constructed and experimentally realised. All-in-fiber design laser was used to

seed both femtosecond Yb:CaF_2 and picosecond Nd:YAG amplifiers of the high energy OPCPA system. Ultrashort pulses at 1030 nm wavelength with a spectral bandwidth of 10 nm were produced from one output channel of the laser and compressed externally to 305 fs, which was close to a transform-limited pulse duration. Strongly chirped 520 ps duration pulses at 1064 nm wavelength were formed at the second output of the laser. Both channels provided sufficient amount of seed energy for the further amplification.

2.2 Method for generation of femtosecond light pulses based on fiber laser technology

Material related to this chapter was published in A1 and described in patent P2

In this chapter, an experimental realisation of a novel method for generation of femtosecond light pulses is presented. This method was implemented in an OPCPA system front-end in which few-cycle pulses around 800 nm wavelength were generated, amplified and compressed. Such scheme combines the patented concept of an optically synchronised dual-wavelength laser source described in the previous chapter with a new approach of high energy femtosecond pulse formation performing parametrical amplification and compression of spectrally broadened pulses from the fiber laser and white-light supercontinuum (WLC) generation.

The experimental setup of a novel front-end for a femtosecond OPCPA system is pictured in Fig. 2.2.1. Multiple channel picosecond all-in-fiber laser was used to serve both as a seeder for Nd:YAG regenerative amplifier and an optical parametric amplifier (ps OPA) which all-together were incorporated to form femtosecond pulses suitable for a consecutive WLC generation and parametric amplification.

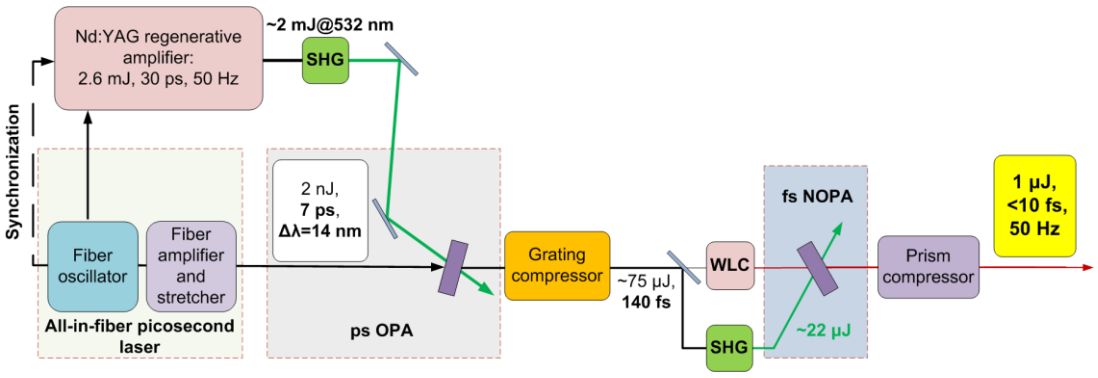

Fig. 2.2.1 Principal experimental scheme of the OPCPA system front-end. Multiple channel all-in-fiber picosecond laser was used to seed Nd:YAG pump laser and an optical parametric amplifier (ps OPA) in order to form pulses for WLC generation. WLC pulses were amplified in femtosecond noncollinear OPA (fs NOPA) and then compressed using a prism compressor.

The detailed scheme of the experimentally constructed fiber laser is presented in Fig. 2.2.2. A passively mode-locked all-in-fiber oscillator generated 2 ps pulses at 1064 nm central wavelength. The pulse duration was determined by

CFBG with optimised dispersion. Stable single pulse mode-locking regime at 31.2 MHz repetition rate was achieved using a SESAM.

In order to check the pulse temporal and spectral characteristics at different output ports of the oscillator, the numerical modelling was performed. Modelling methodology and parameters for the calculation are fully presented in Chapter A.2.

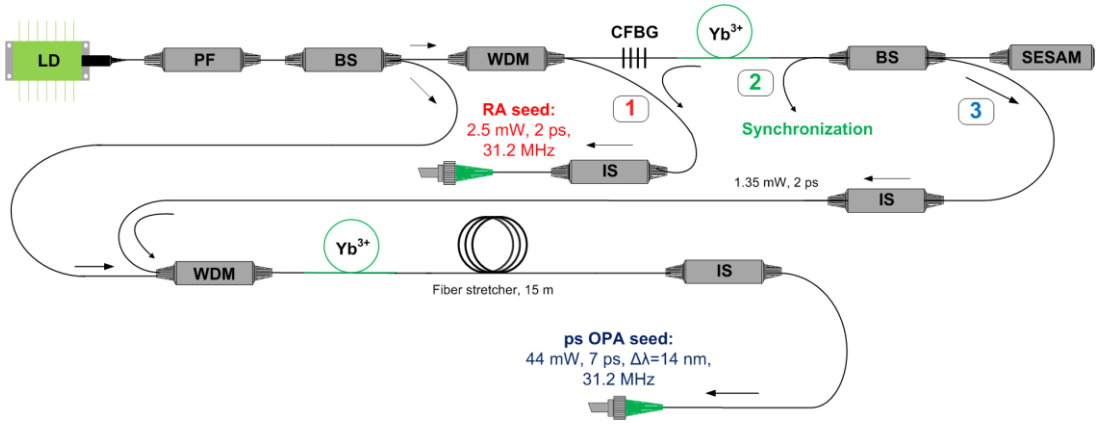

Fig. 2.2.2 The scheme of a picosecond all-in-fiber laser in detail. The abbreviations stand for: LD – laser diode, PF – protection filter, BS – beam splitter, WDM – wavelength division multiplexer, CFBG – chirped fiber Bragg grating, SESAM – semiconductor saturable absorber mirror, IS – isolator, RA – regenerative amplifier. Numbers 1, 2, 3 indicate the oscillator output ports described in the text.

Modelling of the mode-locked fiber oscillator

The main objective of the modelling was to calculate steady-state solutions of the complex pulse envelope at two output ports of the oscillator. The first one was formed inside the cavity using a beam splitter which was placed close to the SESAM unit. A partially transmitting CFBG served as a second output port.

The experimentally measured reflection spectrum of CFBG used in this scheme was provided by the commercial supplier (TeraXion). The dispersion value of CFBG was only estimated and not measured, thus at first it was set to the estimated value of 2 ps/nm and then recalculated according to the better coincidence between measured and modelled output pulse spectrum of the oscillator. Experimentally measured and calculated reflectivity of the grating is compared in Fig. 2.2.3(a). CFBG had a 50% reflection coefficient at the design wavelength of 1064.135 nm. Despite some minor irregularities in the measured spectrum, numerical and experimental data were in good agreement. It is shown

in the picture, that the correct dispersion value was slightly less than 2 ps/nm and not perfectly constant at the FHWM of the grating bandwidth which was 2.89 nm. The dispersion value varied from 1.74 to 2.03 ps/nm in that range and was equal to 1.87 ps/nm at the design wavelength λ_D. The grating exhibited zero dispersion at λ_D in the calculated response to the transmitted pulse (Fig. 2.2.3(b)), but still the value slightly changed in the same manner as in reflection.

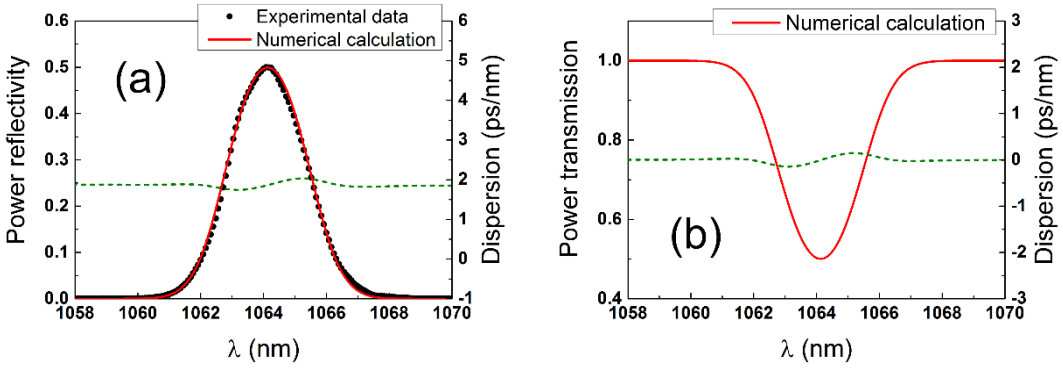

Fig. 2.2.3 Numerically modelled CFBG: (a) calculated power reflectivity spectrum (red curve) compared with experimental data (black dots), dashed green curve corresponds to the calculated dispersion; (b) calculated power transmission spectrum (red curve) with the corresponding dispersion curve (dashed green).

Calculated steady-state output pulses outcoupled through the beam splitter were compared with experimental data (Fig. 2.2.4). Amplification parameters of the numerical model were chosen in the way that the ratio between the main spectral peak and the nearest side peak would be equal to the measured experimentally. This spectrum was measured at 1.65 mW average output power. In order to emphasise the spectral structure of the output pulse, it is pictured in a logarithmic scale (Fig. 2.2.4(b)). The pulse spectrum was 1 nm wide at FWHM and had 8 detectable decreasing intensity sidebands. Four of them were clearly visible in the experimental measurement. However, this measurement lacked a sufficient dynamical range of the spectrum analyser to represent the spectral structure fully. These sidebands appear from constructive mixing between soliton pulse and dispersive radiation that is generated from a perturbated soliton [183]. Such spectral sidebands are characteristic for the soliton mode-locked fiber oscillators. The ratio between the main peak and the sideband spectral intensity decreases when the operating regime approaches the double-

pulse generation threshold. Furthermore, it is possible to determine the total cavity dispersion according to the relative positions of the sidebands and the main peak [184], which helps to calculate the exact value of CFBG dispersion coefficient.

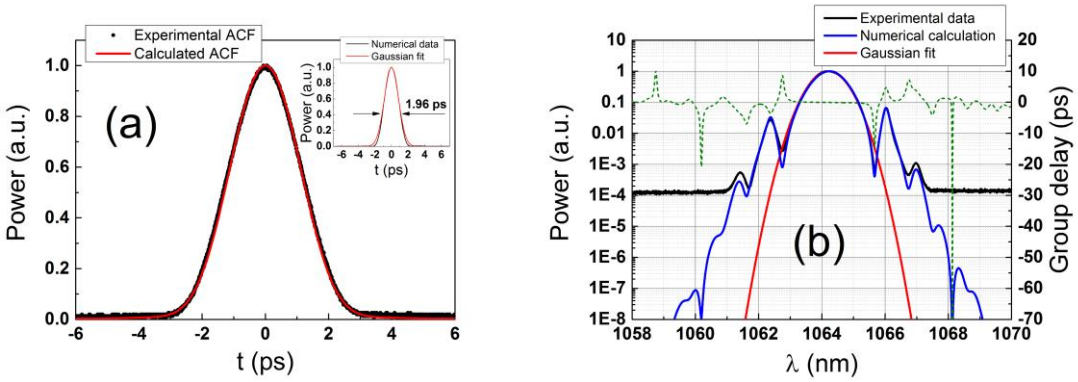

Fig. 2.2.4 Pulse characteristics at the output of the beam splitter: (a) calculated ACF (red curve) compared with the measured one (black dots). Inset: calculated pulse envelope (black curve) compared with a Gaussian function (red curve); (b) experimentally measured pulse spectrum (black curve) compared with the numerically calculated (blue curve) and a Gaussian function (red curve), green dashed trace corresponds to the group delay of the pulse in spectral domain.

The pictured group delay trace (Fig. 2.2.4(b)) indicates that spectral components of the main peak which also constitutes to the soliton pulse in the time domain were in phase and there was no evidence of pulse chirp at this output of the oscillator. The experimentally measured autocorrelation function was in perfect agreement with calculated from the modelled pulse envelope (Fig. 2.2.4(a)). The ultrashort pulse duration corresponded to 1.96 ps. The pulse envelope slightly differed from a Gaussian form due to the steeper edges.

Quite different results compared to the previous case were achieved modelling and experimentally measuring the output from the CFBG (Fig. 2.2.5). The measured average power through this output was 2.98 mW. The pulse envelope had a non-Gaussian, asymmetrical form with a duration of 2.3 ps (Fig. 2.2.5(a)). Calculated pulse spectrum width was larger than at the beam splitter output and corresponded to 1.25 nm (Fig. 2.2.5(b)). The group delay curve (Fig. 2.2.5(b), dashed green) indicated a quasi-linear upchirp which together with the spectral broadening suggests the dominating effect of SPM.

Outcoupling through the beam splitter caused the pulse to experience an extra bounce at the CFBG which added a chirp with an opposite sign (Fig. 2.2.3(a))

and compensated the residual group delay originated from the pulse propagation in fiber. In the other case, pulse transmitted through the grating experienced zero dispersion (Fig. 2.2.3(b)), thus the group delay due to SPM and cavity dispersion was left partly uncompensated. An additional spectral broadening was visible in the experimental trace (Fig. 2.2.5(b)) which was caused by SPM when pulse propagated in a single-mode fiber to the spectrum analyser.

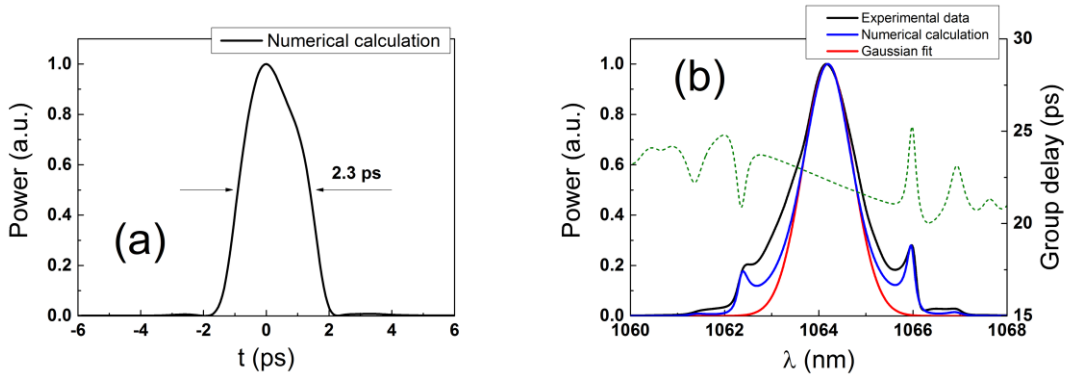

Fig. 2.2.5 Pulse characteristics at the output of CFBG: (a) calculated pulse envelope (black curve); (b) experimentally measured pulse spectrum (black curve) compared with the numerically calculated (blue curve) and Gaussian function (red curve), green dashed trace corresponds to the group delay of the pulse in spectral domain.

To sum up the results of this numerical modelling, Gaussian-like, nearly transform-limited pulses were produced from the fiber oscillator when outcoupling radiation through the beam splitter which was placed near the SESAM. Linearly chirped, asymmetrical form pulses were transmitted through the CFBG. Both outputs were used in the experimental setup presented further.

Experimental realisation

Experimentally constructed fiber oscillator had 3 output ports (Fig. 2.2.2). Port 1 was formed by using wavelength division multiplexer (WDM) to extract pulses transmitted through CFBG and used for seeding the Nd:YAG regenerative amplifier (RA). Although the output power from this port was 2.5 mW which corresponded to ~80 pJ pulse energy, only small fraction of the pulse spectrum coincided with Nd:YAG amplification bandwidth (Fig. 2.2.6).

Port 2 and Port 3 were formed using polarising beam splitter (BS) which was fusion spliced inside the resonator. Port 2 was used to synchronise fiber laser with the regenerative amplifier. This port was attached to a photodetector which gave a feedback signal to the synchronisation electronics of the amplifier.

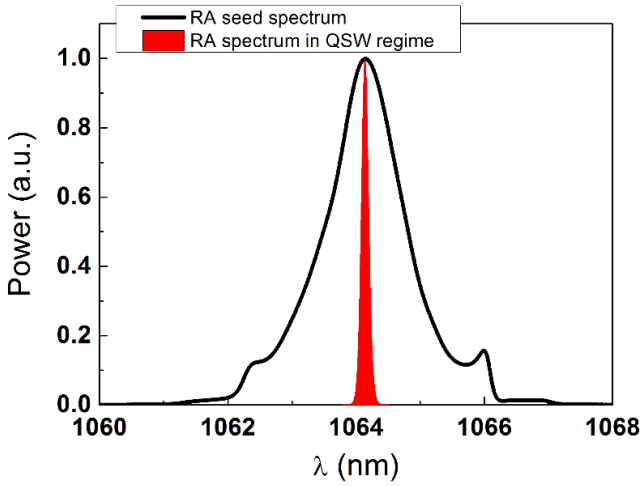

Fig. 2.2.6 Spectrum of the seed pulse for regenerative Nd:YAG amplifier, coloured area corresponds to measured RA output spectrum in QSW regime which shows the amplification bandwidth.

Port 3 was used to form pulses suitable for WLC generation. First of all, pulses were amplified in Yb^{3+} doped fiber amplifier. After the amplification pulse spectrum was stretched to ~14 nm by self-phase modulation in a single-mode polarisation maintaining fiber (Fig. 2.2.7(a)). The output power after the stretcher was 44 mW which corresponded to 1.4 nJ pulse energy. The pulse was temporally broadened to ~7 ps due to the dispersion in fiber.

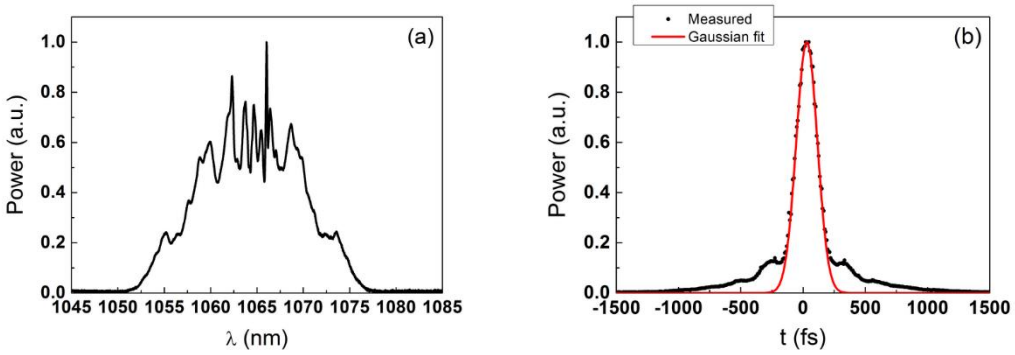

Fig. 2.2.7 (a) Spectrum of the NOPA seed pulses; (b) Autocorrelation trace of the compressed pulses which were used to generate WLC. The retrieved compressed pulse duration was 141 fs at FWHM when fitted with Gaussian function.

Spectrally broadened pulses were coupled out of the fiber via free-space collimator and amplified in an optical parametric amplifier (ps OPA in Fig. 2.2.1) to 100 μJ. Nd:YAG regenerative amplifier which was used as a pump produced 30 ps, 2.6 mJ pulses at 1064 nm which were frequency doubled with ~77% conversion efficiency using 9 mm length LBO crystal. The pump laser repetition rate was 50 Hz. Type I phase-matched 6 mm length BBO crystal was used in ps OPA and ~$7 \cdot 10^4$ amplification factor with 5% pump energy conversion was reached. This amplification stage was not optimised regarding an efficient temporal overlap between the signal and the pump. The ratio of the signal and the pump pulse duration was ~0.2 which indicated the prospect to achieve higher amplification factor by increasing this ratio. The pulse-to-pulse energy stability of the amplified signal was 0.25% measuring every pulse during 15 s period. This result indicated that the amplifier was close to the saturation regime as the energy stability parameter of the amplified signal and the pump pulses was nearly equal.

After ps OPA stage, pulses were compressed to ~140 fs duration (Fig. 2.2.7(b)) by diffraction grating compressor. 1000 grooves/mm transmission diffraction gratings working at Littrow configuration were used. The contrast of the compressed pulses was limited by the residual third order dispersion of the grating compressor which is seen from the pedestal in the autocorrelation trace (Fig. 2.2.7(b), black dotted curve).

A small part of the amplified and compressed light (~0.7 μJ) was focused into a 5 mm sapphire plate to generate WLC (Fig. 2.2.8, grey coloured curve). Focusing conditions and pulse energy were chosen to produce smooth and stable WLC.

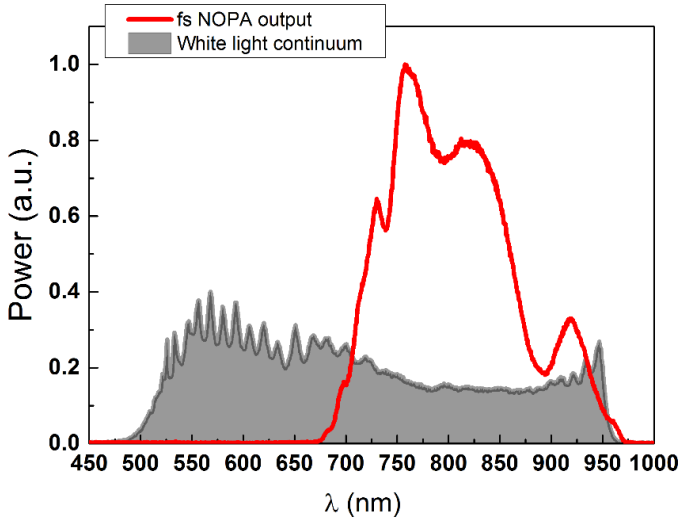

Fig. 2.2.8 White-light continuum generated in 5 mm sapphire plate (grey coloured area) and femtosecond NOPA output in a few-cycle regime (red curve). In order to remove 1064 nm radiation longer wavelengths (>970nm) were filtered using a short-pass filter.

The remaining part of the light (~70 μJ) was frequency doubled in a 2.5 mm thick BBO crystal with a ~32% frequency conversion efficiency and later used as a pump for femtosecond NOPA to pre-amplify broadband (690-960 nm) WLC (Fig. 2.2.8, red curve) to about 1.5 μJ pulse energy. Parametric amplification was realised in a 2 mm thick BBO crystal (type I) at a phase matching angle $\theta \approx 24^{o}$ and a noncollinearity angle $\alpha \approx 2.4^{o}$ in order to reach the broadest amplification bandwidth. The pump beam spot size in the crystal was adjusted to achieve the highest intensity avoiding significant parametric fluorescence generation.

In order to achieve shortest possible pulse duration from the femtosecond NOPA, we had to compensate the material dispersion of the system. Although only reflective optics were used after the WLC generation, pulses experienced temporal broadening passing through the sapphire plate and BBO crystal. We used a fused silica prism compressor and a pair of N-BK7 glass wedges for the fine tuning of the dispersion in the system. The chirpscan method [185] was used

to characterise output pulses. Chirpscan diagrams and retrieved pulse envelope (red curve) are shown in Fig. 2.2.9. Obtained pulse duration at FWHM was 8.5 fs compared to 7.9 fs transform-limit corresponding to the measured spectrum (Fig. 2.2.9(d)).

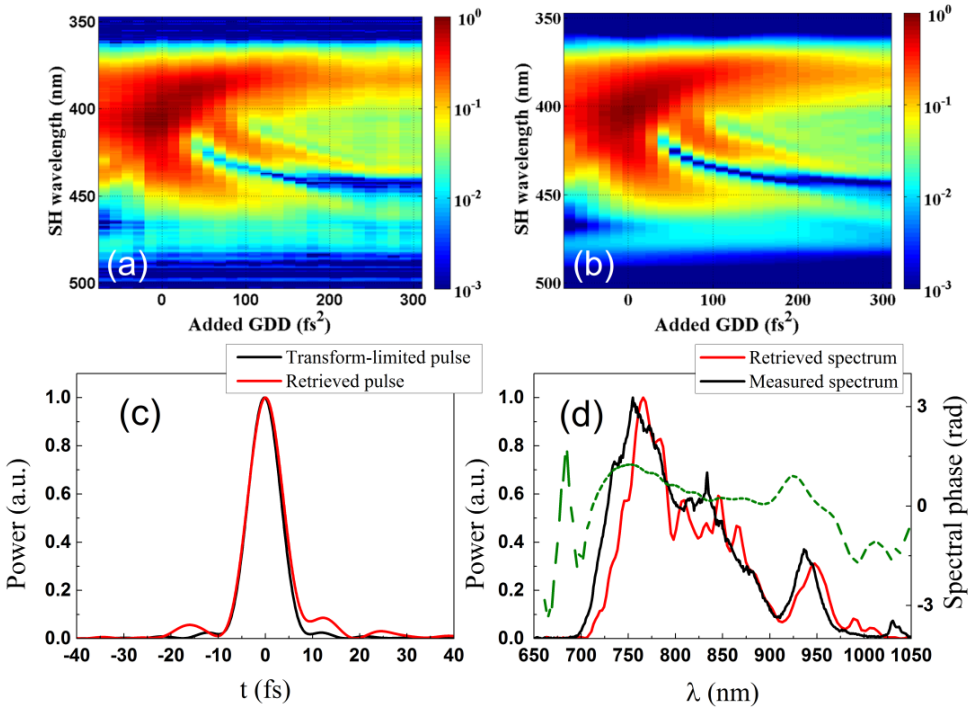

Fig. 2.2.9 The results of pulse characterization after a noncollinear parametric amplification of a broadband supercontinuum seed and dispersion compensation with a prism compressor. The measurement was realised using chirpscan method: (a) experimentally measured chirpscan trace; (b) numerically retrieved chirpscan trace; (c) retrieved pulse envelope compared with a transform-limited pulse; (d) measured and retrieved pulse spectra and retrieved spectral phase (dashed green trace).

Conclusions

A novel front-end for femtosecond OPCPA was constructed and experimentally realised using all-in-fiber picosecond laser which served both as an optical seed source for Nd:YAG amplifier and as a driving source for WLC generation. This approach has immensely simplified the synchronisation between seed and pump lasers.

The experimentally measured pulse duration of the parametrically amplified WLC was 8.5 fs. This corresponded to 3 optical cycles and nearly transform-limited pulse duration, which could be used for few-cycle OPCPA reaching extremely high peak intensity fields with excellent pulse contrast.

3 Optimisation of the FCPA scheme by implementing the method of tunable higher-order dispersion compensation

Material related to this chapter was published in A3

Theoretical calculations and experimental work presented in this chapter are a slight departure from the topics of Chapters 2 and 4, because here the analysis of the FCPA system is described. However, issues related with large temporal stretching and recompression of ultrashort pulses can be similar for both femtosecond FCPA and OPCPA systems. The main similarity is a necessity to compensate the third and higher orders of dispersion which can cause pulse broadening and distortion at the output of the system.

An elegant method to deal with the residual dispersion in FCPA scheme is the employment of specially designed CFBG as a pulse stretcher. Commercially available CFBG stretchers can be manufactured with controlled dispersion parameters up to the fifth order. However, inability to adjust these values during the experimental realisation of the system may result in a far from perfect pulse compression. The main reasons for such limitation are estimating errors of the exact system dispersion and the effect of fiber nonlinearity, causing phase modification of the pulse. Furthermore, the ability to tune the dispersion parameters enables to design and modify the experimental realisation of the FCPA system more freely.

In this chapter, the way of achieving high contrast femtosecond pulses from FCPA system through the application of pulse stretching allowing for the tuning of dispersion parameters in CFBG was investigated. In the beginning, picosecond pulses were generated in a passively mode-locked fiber oscillator, then pre-stretched in a passive fiber, in which spectrum and duration of pulses were broadened due to combined effects of SPM and dispersion. Then a CFBG with temperature tuning capability was used as the main pulse stretcher. After stretching, pulses were amplified in an LMA fiber amplifier and compressed using a conventional grating compressor. By inducing nonlinear temperature

distribution along the CFBG, its dispersion characteristics were modified enabling to tune TOD or even higher-order dispersion parameters and to minimise residual uncompensated spectral phase after pulse compression with the grating compressor. This method was investigated numerically and verified experimentally by using CFBG stretcher with 4 independently controlled thermoelectric cooler (TEC) elements. Significant improvement in the pulse compression by optimising the nonlinear temperature distribution along CFBG stretcher was achieved.

Numerical analysis

Theoretical calculations were performed in order to simulate the effect of the induced nonlinear temperature distribution along CFBG in the FCPA system and to identify optimal conditions for possible experimental realisation. The numerical model is depicted as a block diagram in Fig. 3.1. This model was based on the experimental FCPA system. The methodology of numerical calculation is described in Chapter A.

The seed source of the system was a passively mode-locked all-in-fiber picosecond oscillator working at a 1064.63 nm center wavelength. Calculated 2 ps duration pulses from the fiber oscillator were preamplified up to 2 nJ pulse energy. Then, pulses were stretched to more than one hundred of picoseconds duration in 200 m long passive single-mode optical fiber (MFD – 6.3 μm). Pulses were stretched in time because of material dispersion and in frequency domain due to SPM.

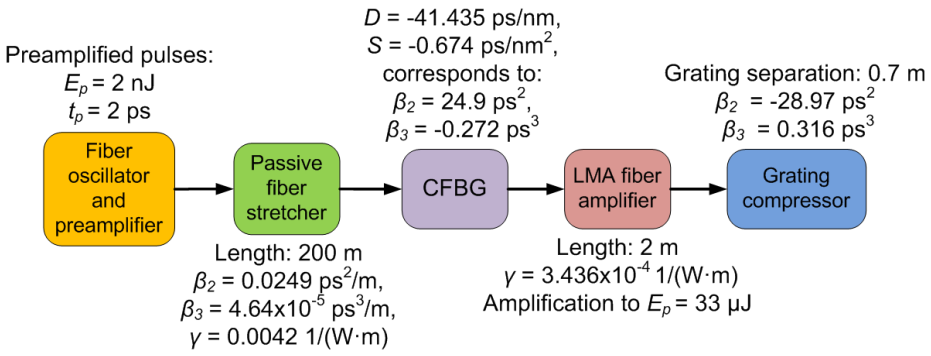

Fig. 3.1 Theoretical modelling scheme. Each block indicates pulse formation and amplification stages with different dispersion and nonlinearity parameters. E_p – pulse energy, t_p – pulse duration.

At the next stage of calculations, CFBG parameters were applied. CFBG reflection spectrum was provided by the manufacturer (Fig. 3.2). The group delay curve ($GD = D(\lambda - \lambda_0) + \frac{S}{2}(\lambda - \lambda_0)^2$) is presented in Fig. 3.2 as grey trace, which corresponds to the dispersion parameter and dispersion slope (at nominal temperature of 77 ^{O}C) equal to D = -41.435 ps/nm and S = -0.674 ps/nm^2 respectively.

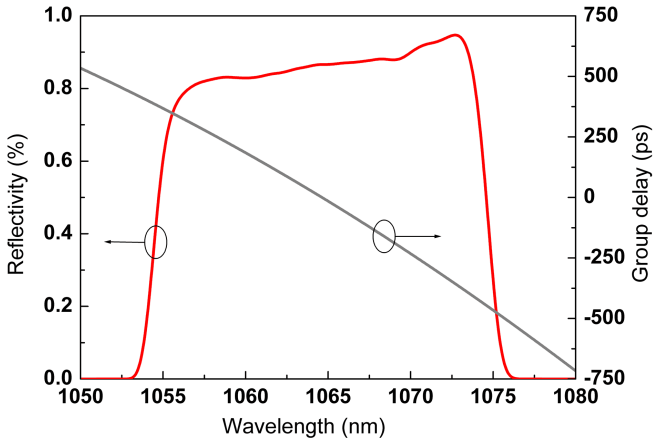

Fig. 3.2 Reflection spectrum and calculated group delay curve of unperturbed CFBG (at a nominal temperature of 77 ^{O}C), which is further used in the experimental setup.

Stretched pulses were propagated and amplified in LMA fiber amplifier (MFD – 22 μm) up to 33 μJ by numerical integration of the nonlinear Schrödinger equation with the wavelength-dependent gain. Finally, pulses were compressed using dispersion parameters of the diffraction grating compressor with 1600 grooves/mm line density gratings. The grating separation was tuned according to the highest peak power of the compressed pulse. The temporal profile of the optimally compressed pulse is shown in Fig. 3.3 (black trace). As it can be seen from the picture, the temporal envelope of the pulse has significant trailing edge oscillations. These distortions originate mainly from TOD mismatch between the stretcher and the compressor. The pulse spectrum (Fig. 3.3 inset) reveals modulations in spectral domain caused by the nonlinear amplification (calculated B-integral value – 1.36π rad) of non-Gaussian seed pulses in an LMA fiber, which also affects temporal contrast of the compressed pulse. These effects add to the residual nonlinear phase, which cannot be compensated using a conventional grating compressor.

Next, transform-limited (TL) pulses of the corresponding spectrum (Fig. 3.3 inset) were calculated. In order to calculate the temperature distribution along CFBG, which is required to compensate phase distortions and achieve nearly TL pulses at the system output, the reverse propagation modelling was performed [186].

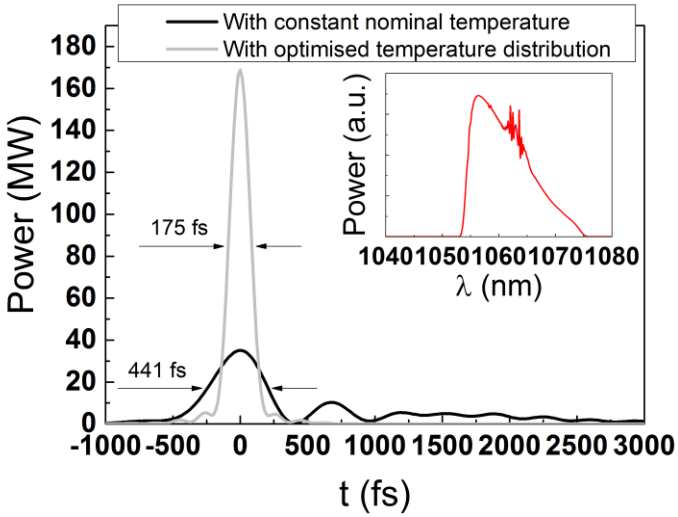

Fig. 3.3 Compressed pulse envelope at the FCPA system output with and without nonlinear temperature distribution applied along CFBG. Amplified pulse spectrum is pictured in the inset of the graph.

After reverse propagation of TL pulses from the system output to the point between CFBG and the LMA fiber amplifier, a group delay as a function of wavelength $GD_{optimal}(\lambda)$ corresponding to the optimal pulse compression was calculated. The group delay (GD) as a function of wavelength before CFBG $GD_{before}(\lambda)$ of pre-stretched pulse and of CFBG itself $GD_{CFBG}(\lambda)$ (Fig. 3.2 grey trace) were also known. By taking the inverse of these functions, the required wavelength shift for each group delay point was found and, accordingly, the temperature distribution was calculated from the relation:

$$T(GD) = \frac{\lambda_{optimal-before}(GD) - \lambda_{CFBG}(GD)}{k\lambda_{CFBG}(GD)} + T_0. \quad (3.1)$$

This formula has been derived using the linear approximation of Bragg wavelength shift dependence on temperature [187]:

$$\Delta\lambda_B = \lambda_B k \Delta T. \quad (3.2)$$

The temperature-dependent refractive index change has a predominant influence on Bragg wavelength shift, so thermal expansion influence was neglected. k represents the thermo-optic coefficient ($k = 7 \cdot 10^{-6}$ $^{o}C^{-1}$), which was determined from measurements of the temperature-dependent center wavelength shift of the narrowband FBG reflection spectra. T_0 is a nominal CFBG temperature, which is 77 ^{o}C.

The calculated temperature distribution required to achieve the nearly TL pulses at the system output is presented in Fig. 3.4. The modelling reveals that temperature values are not highly elevated, span over the range of only 30 ^{o}C and so could possibly be achieved under experimental conditions. Furthermore, the numerical results indicate a significant improvement in temporal contrast of the compressed pulse, compression of pulse duration by nearly 60 % and increase of pulse peak power by factor of 4.8 at the FCPA system output (Fig. 3.3, grey trace). It should be noted that the envelope of the compressed pulse in the case of optimal temperature distribution is almost identical to the TL pulse envelope (peak power mismatch <0.5%). Because of this, the TL pulse envelope is not indicated separately in Fig. 3.3. To verify this spectral phase compensation method, an experimental investigation was accomplished, which is presented in the following section.

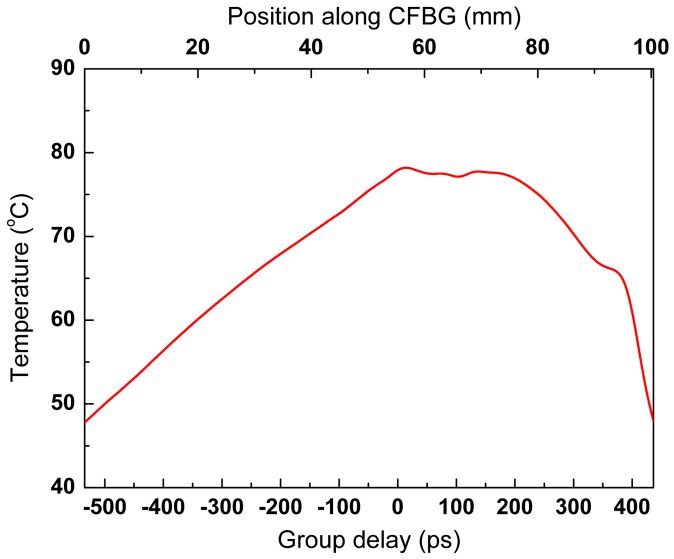

Fig. 3.4 Calculated temperature distribution along CFBG, which is required to achieve TL pulses at the FCPA system output. The bottom horizontal scale shows group delay values and top horizontal scale shows calculated position along CFBG.

Experiment

The schematic diagram of the experimental setup is depicted in Fig. 3.5. All fibers used in this system were polarisation maintaining PANDA type. Ultrashort pulses of 2 ps duration were generated in all-in-fiber passively mode-locked oscillator operating at 1064.63 nm center wavelength. These pulses were amplified in a Yb^{3+} doped single-mode fiber preamplifier up to 2 nJ energy. Then pulses were broadened in time and frequency domains because of the combined effects of SPM and dispersion in a 200 m long passive fiber. After that, pulse stretching in time domain was applied using custom designed CFBG with temperature tuning capabilities (TeraXion Inc.). Parameters of CFBG (at nominal temperature) used in the experiment were described in the previous section (Fig. 3.2). Total dispersion parameters of the stretcher module (passive fiber and CFBG) can be evaluated to be equal to: β_2 = 29.91 ps^2, β_3 = -0.263 ps^3.

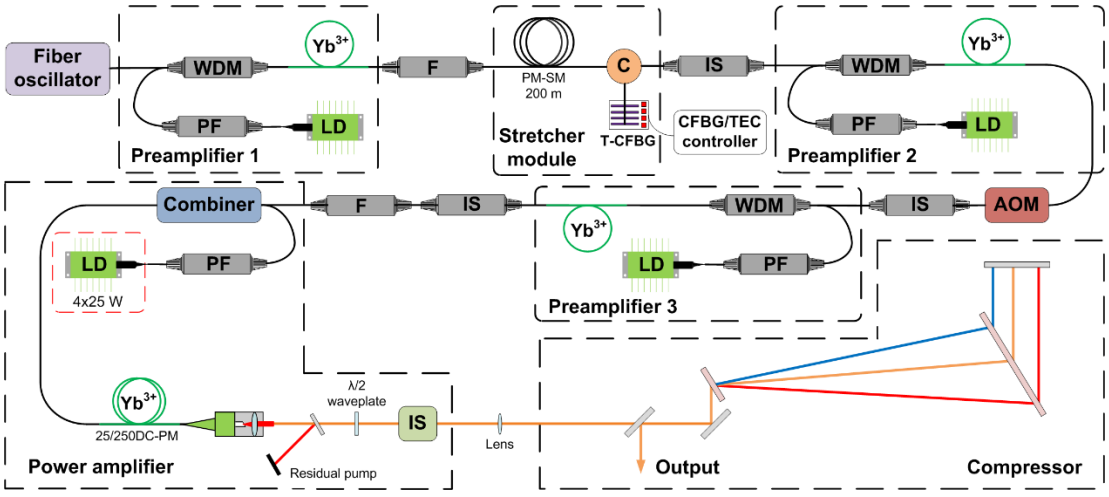

Fig. 3.5 Schematic diagram of the experimental FCPA system with tunable CFBG stretcher. The abbreviations stand for: LD – pump laser diode, PF – protection filter, F – ASE filter, IS - optical isolator, WDM – wavelength division multiplexer, T-CFBG – CFBG module with temperature tuning capabilities, AOM – acousto-optic modulator, 25/250DC-PM – Yb^{3+} doped polarisation maintaining double-clad LMA fiber.

The temperature distribution along CFBG was controlled by 4 TEC, separated by equal distances of 33 mm, which allowed GVD tuning by setting constant temperature gradient along the whole CFBG or tuning of the higher-order dispersion parameters by setting different temperature gradients at three sections along CFBG. The temperature tuning range for each of TEC was 35-120 °C. As there were only three sections for setting different temperature

gradient (only 4 TEC elements), the higher-order dispersion parameter tuning was limited. By using a larger number of TEC's along CFBG and thus controlling larger number of temperature gradients, it could be possible to tune dispersion characteristics in CFBG stretcher with much higher precision. Such CFBG devices with as many as 32 resistive heater elements [188] or 10 TEC elements [189] have already been demonstrated for material dispersion compensation purposes in telecommunication applications.

The measured pulse envelope in the time domain and pulse spectrum after the stretcher module is depicted in Fig. 3.6. After the stretcher fiber, the pulse spectrum was slightly broader than the CFBG reflection bandwidth, so spectrum wings were truncated. The measured pulse duration was 761 ps (FWHM).

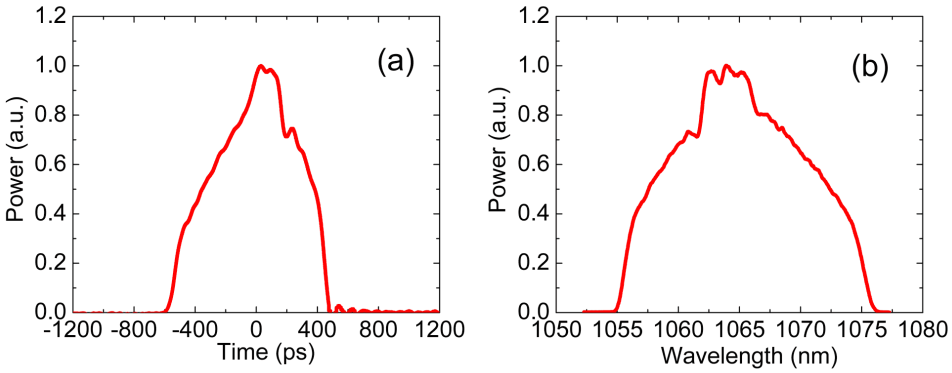

Fig. 3.6 (a) Temporal envelope of the stretched pulses measured using 35 ps response photodiode and 20 GHz oscilloscope. (b) The spectrum of the stretched pulses.

Stretched pulses were amplified in the second single-mode preamplifier, after which the pulse repetition rate was reduced from 30 MHz down to 100 kHz using acousto-optic modulator (AOM). Next, pulses were amplified in the third preamplifier and, finally, in the power amplifier based on 25 μm core diameter LMA double-clad Yb^{3+} doped fiber. Pump radiation from laser diodes (976 nm) and pulses to be amplified were launched into LMA fiber using fused-fiber pump and signal combiner (ITF Labs). The entire system up to the power amplifier output was essentially monolithic.

The pulses were compressed after amplification using the diffraction grating compressor. In the compressor, high diffraction efficiency (>94%) transmission gratings with 1600 grooves/mm line density were used (LightSmyth

Technologies Inc.). The optimal pulse compression was achieved when the distance between the diffraction gratings was ~0.7 m, which is in accordance with numerical calculations. Compressor dispersion parameters calculated for this grating separation are: β_2 = -28.97 ps^2; β_3 = 0.316 ps^3. It can be seen that there is some mismatch between the total stretcher's (200 m fiber and CFBG) TOD (β_3 = -0.263 ps^3) and the compressor's TOD. This mismatch arises because CFBG was designed with dispersion parameters to be compensated by compressor with grating separation of 0.6 m alone, and dispersion of 200 m stretcher fiber was not included.

In order to characterise the pulse compression, autocorrelation functions of pulses after the compressor were measured. First, the pulse compression when CFBG temperature was constant or with a constant temperature gradient was investigated. For every CFBG temperature setting the grating separation was reoptimised for the best compression. Pulse compression was slightly better, when constant temperature gradient, illustrated by black squares in Fig. 3.7, was set compared to the case with constant temperature (temperature gradient was zero). This indicates that a different GVD/TOD ratio was more favourable for pulse compression. Next, TEC temperatures were optimised by manually tuning each of them and monitoring in real-time pulse autocorrelation trace after the compressor. First, the temperature values were changed in coarse steps in order to find the interval of temperature values for which duration of autocorrelation trace and pedestal is decreasing and peak power is increasing. Then more fine-tuning was accomplished so as to select single temperature values corresponding to autocorrelation trace with highest peak power. Because temperature tuning at only 4 points was available, it was possible to set 3 different temperature gradients and, accordingly, change dispersion parameters at 3 sections of CFBG. The change in dispersion parameters versus wavelength actually represents the higher-order dispersion. The best compression results were achieved when temperature distribution along CFBG was set as shown by grey circles in Fig. 3.7.

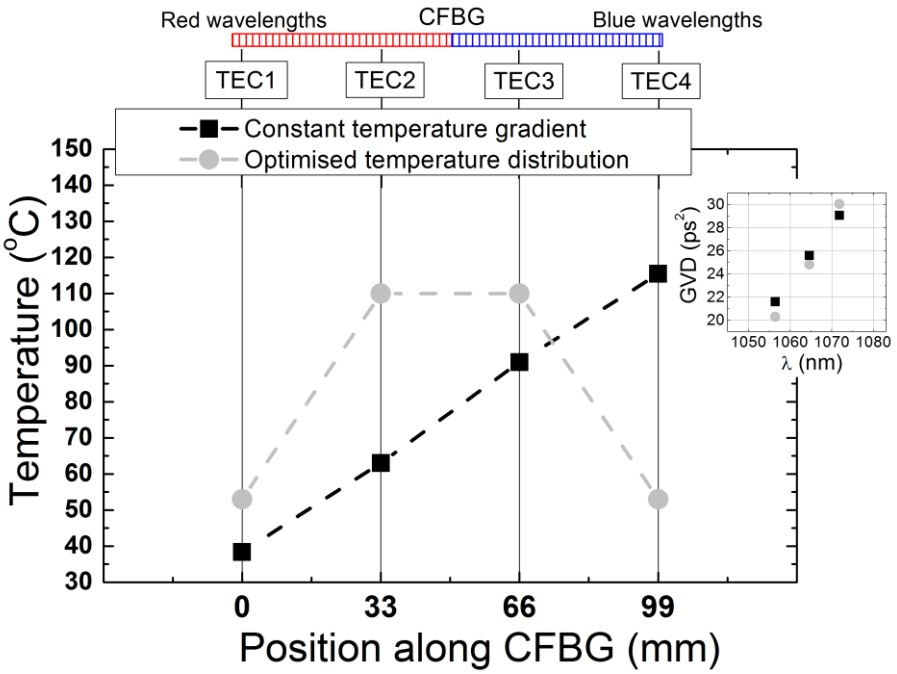

Fig. 3.7 Illustration of TEC-controlled temperature values along CFBG. Black squares – constant temperature gradient set. Grey circles – temperature of each TEC manually optimised for optimal compression. Inset – Evaluated GVD change versus wavelength for temperature distributions shown in the main graph.

This temperature distribution showed the best compression results for the experimental conditions. However, slight further optimisation could be possible by implementing rigorous search algorithm which would check all possible temperature combinations with a fine step. The experimentally achieved optimal temperature distribution is similar qualitatively but differs quantitatively from the temperature profile calculated from numerical modelling (Fig. 3.4). This could be caused by limited experimental capabilities in temperature tuning. In the experiment, the temperature tuning was available only at 4 points along CFBG, and the temperature variation was mostly linear between them, so the exact reconstruction of the optimal temperature profile predicted by numerical calculations was not possible. Numerical modelling of temperature-controlled point number influence on the CFBG and, accordingly, pulse peak power after compression, revealed that peak power increases rapidly when increasing temperature-controlled point number from 4 up to 10. At temperature-controlled point number of 10, peak power ratio of the compressed pulse to TL pulse already exceeds 80%. By further increasing temperature-controlled point

number up to 20, peak power ratio increases to 98%. From this value, peak power ratio improves very slowly with an increase in temperature-controlled point number. These results were achieved assuming linear temperature variation between temperature-controlled points and assuming system parameters as described in the section of the numerical analysis.

In Fig. 3.8, autocorrelation functions are compared when the optimised temperature distribution was set (shown in Fig. 3.7 as grey circles) with the case when the temperature gradient was constant along CFBG (shown in Fig. 3.7 as black squares). Despite limited tuning capabilities of the temperature distribution, the pulse compression improvement is clearly noticeable when the CFBG temperature distribution was optimised. For the output pulse energy of up to 30 μJ (average power of 3 W), the autocorrelation trace corresponding to the optimised (nonlinear) CFBG temperature distribution reveals a significantly smaller pedestal compared to the case when the CFBG temperature distribution was linear (constant temperature gradient).

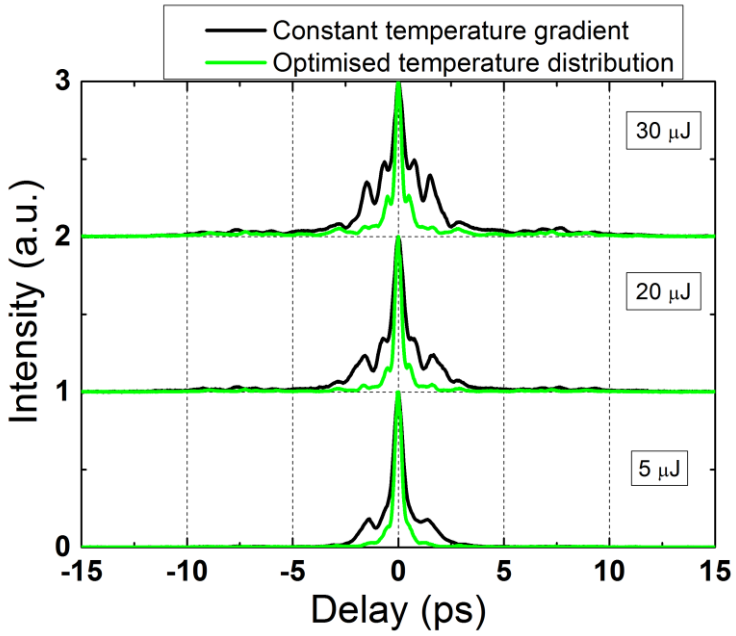

Fig. 3.8 Autocorrelation functions of compressed pulses at different output pulse energies and different CFBG temperature settings. Black trace – constant temperature gradient along CFBG is set. Green trace – temperature of each TEC manually optimised for optimal compression.

In Fig. 3.9(a), the full width at half maximum (FWHM) durations of the central peak of autocorrelation functions versus output pulse energy are

presented. The data show that in the case of the optimised temperature distribution along CFBG, the duration of the main peak of autocorrelation traces is from 33 % to 50 % (at pulse energy from 5 μJ to 30 μJ respectively) shorter than in the case of the constant temperature gradient, but longer than the duration of transform-limited pulses calculated from the experimental spectrum. With the increase of the output pulse energy, the duration of the autocorrelation central peak for the case of the constant temperature gradient increases, while for the case of the optimised temperature distribution it stays nearly the same.

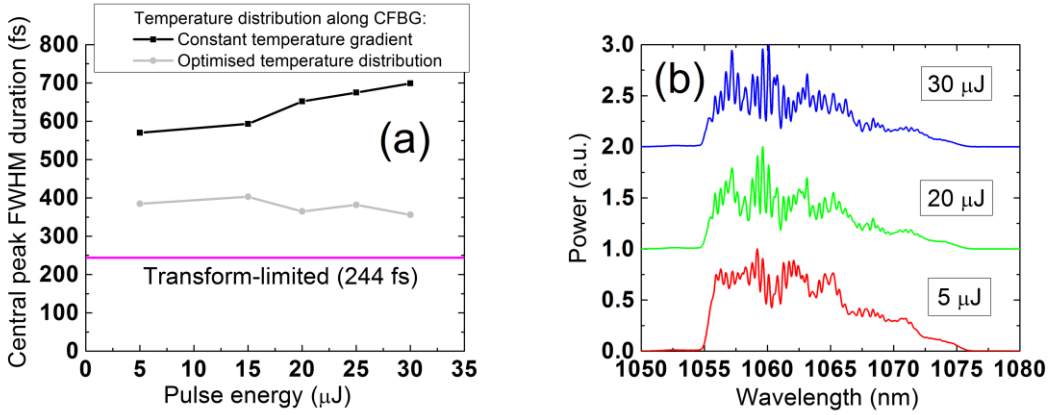

Fig. 3.9 (a) Full width at half maximum durations of the central peak of autocorrelation functions versus output pulse energy. (b) Spectra of amplified pulses at a different output pulse energy.

The optimal temperature distribution (as shown in Fig. 3.7 by grey circles), which has contributed to the better pulse compression, causes GVD parameter of CFBG to increase more rapidly with wavelength (Fig. 3.7 inset) and this effectively means the increase in the absolute value of TOD parameter. Since TOD of the stretcher module (at constant temperature) was lower than TOD of the compressor (comparing the absolute values), the increase in the temperature distribution induced TOD can be indicated as the main reason for the pulse compression improvement.

At pulse energies of more than 30 μJ, pulse deterioration after compression was registered which could not be removed by further tuning of CFBG temperature or grating compressor. The pulse contrast deterioration might have been caused by pulse spectrum modulations which were present after power amplifier and increased with output pulse energy (Fig. 3.9(b)). Spectral

amplitude modulations of chirped pulses in the presence of SPM cause spectral phase distortions, and this degrades the pulse contrast after compression [190]. It should be possible to reduce spectral modulations by carefully designing the whole system – particularly using high quality fiber optics components with a perfectly flat spectral response.

Conclusions

The femtosecond FCPA system with the temperature-tunable CFBG stretcher was investigated. The numerical analysis has shown that significant pulse compression improvement down to transform-limited duration is possible by optimising temperature distribution along the CFBG stretcher. This concept was tested experimentally by using the CFBG stretcher with 4 independent TEC elements. Despite the limited 4-point temperature tuning, by optimising the temperature distribution along CFBG, a significant pulse compression improvement, manifested by the lower pedestal and up to 50 % shorter duration of the autocorrelation function, compared to the case when temperature distribution was constant or linear, was experimentally achieved. This indicates the suitability of this method for FCPA systems for the higher-order dispersion parameter tuning. By using CFBG with a significantly larger number of TEC elements and careful management of temperature distribution nearly transform-limited pulses should be achievable as predicted by the numerical calculations.

Concerning the results achieved with the FCPA system, similar pulse stretching and compression scheme in the OPCPA front-end, which is presented in the next chapter, was theoretically investigated and experimentally realised.

4 Femtosecond wavelength-tunable OPCPA system based on picosecond fiber laser seed and picosecond DPSS laser pump

Material related to this chapter was published in A1

In this chapter, experimental realisation of a compact femtosecond wavelength-tunable OPCPA system with a novel front-end described in Chapter 2 is presented. This system used a spectrally broadened picosecond fiber oscillator for seeding picosecond DPSS regenerative amplifier and WLC generator. All the achievements in the development and optimisation of the OPCPA front-end based on hybrid fiber and solid-state laser technologies described in the previous chapters were implemented into this table-top OPCPA system.

The principle scheme of the femtosecond wavelength-tunable OPCPA system is presented in Fig. 4.1. The experimental setup consisted of OPCPA front-end based on white-light supercontinuum generation and parametric amplification by femtosecond pulses and picosecond OPCPA amplifier. Picosecond DPSS Nd:YVO_4 laser was used as a pump source.

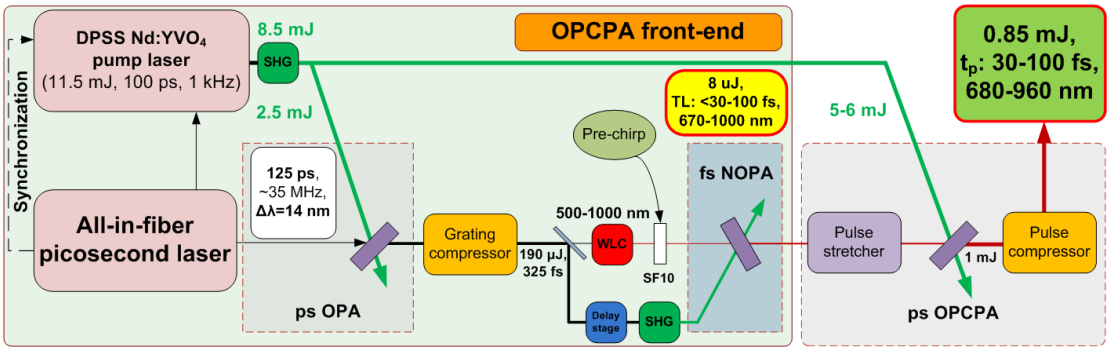

Fig. 4.1 Principal experimental scheme of the femtosecond wavelength-tunable OPCPA system. Multiple channel all-in-fiber picosecond laser was used to seed DPSS pump laser and an optical parametric amplifier (ps OPA) in order to form pulses for white-light supercontinuum (WLC) generation. WLC pulses were preamplified in femtosecond noncollinear OPA (fs NOPA) performing wavelength tuning, then stretched to picosecond duration, amplified in one stage OPCPA amplifier and recompressed.

Multiple channel fiber laser

The seed source of the OPCPA front-end and the pump source was picosecond monolithic fiber laser (Fig. 4.2), which consisted of three main parts: the picosecond oscillator, the seed formation chain for the regenerative amplifier

(RA) pump and the seed formation chain for the optical parametric amplifier (ps OPA).

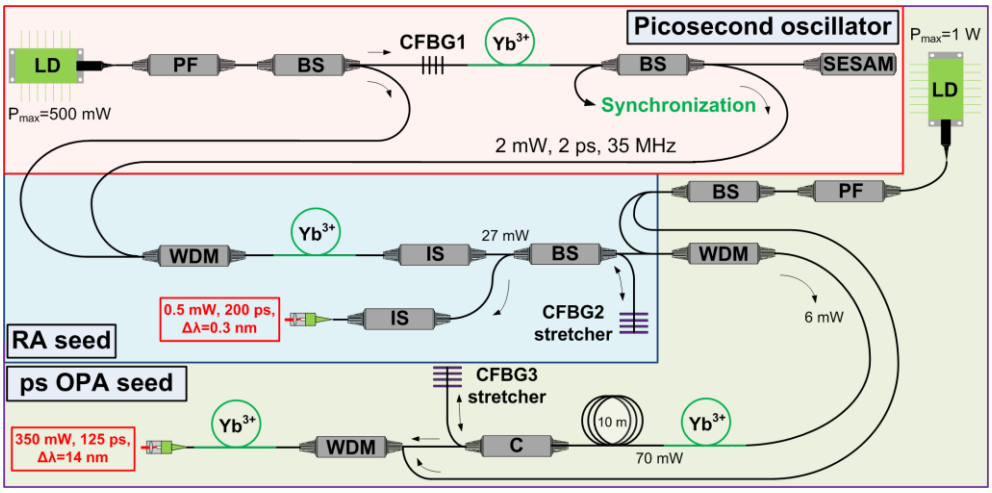

Fig. 4.2 Principle scheme of picosecond all-in-fiber laser. Passively mode-locked fiber oscillator generated 2 ps pulses which were divided into two branches. In one branch, narrowband and chirped pulses were formed in order to seed the DPSS regenerative amplifier. Another branch was used for broadband (~14 nm) pulses formation which were later amplified parametrically, compressed to femtosecond duration and then used to generate WLC.

A passively mode-locked fiber oscillator generated 2 ps transform-limited pulses at 1064.15 nm central wavelength. Pulse duration and the central wavelength of the oscillator were determined by reflectivity spectral profile of chirped fiber Bragg grating (CFBG1). The stable single-pulse mode-locking regime at 35 MHz repetition rate was achieved using semiconductor saturable absorber mirror (SESAM) as the end mirror of the resonator.

A Yb^{3+} doped polarisation maintaining single-mode fiber was used as a gain medium which was pumped with a 976 nm laser diode (LD) through the CFBG1. Fiber oscillator had 2 output ports realised by the 70/30 beam splitter (BS) which was fusion spliced inside the resonator. Photodetector connected to one port of the beam splitter was used to synchronise fiber laser with a regenerative amplifier. Average output power from the fiber oscillator was 2 mW.

Ultrafast pulses from the oscillator were amplified in Yb^{3+} doped fiber amplifier to 25 mW and then divided into two branches by 50/50 splitter. In the first branch, pulses were stretched to ~200 ps duration by a narrowband CFBG2 while back-reflected to 50/50 splitter to RA seed output port (Fig. 4.3(a)). A resistive heater element was used to tune the central wavelength of CFBG2 in

order to match the seed spectrum to the gain maximum of the RA (Fig. 4.3(a)). Stretched pulses then were amplified in Nd:YVO_4 regenerative amplifier and a single-pass Nd:YVO_4 booster operated at 1 kHz repetition rate to 11.5 mJ energy. The spectral bandwidth and the duration of the amplified chirped pulse was approximately half that of the input pulse due to gain narrowing effect in RA. The resulting duration of the amplified OPCPA pump pulses was 98 ps as spectral narrowing of chirped pulses results in pulse shortening (Fig. 4.3(b)).

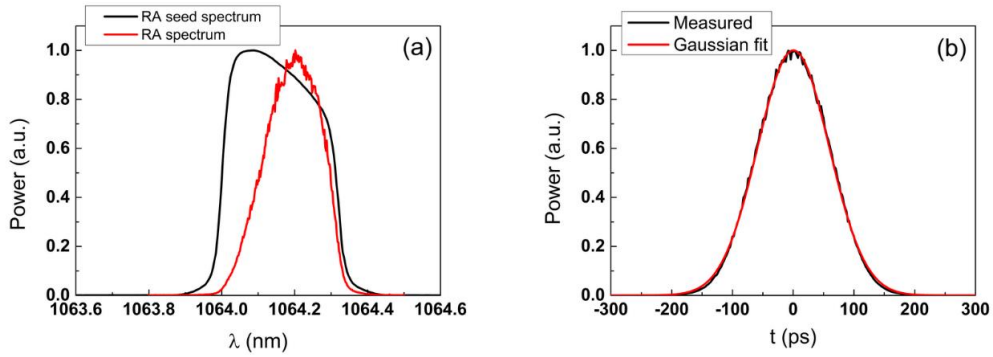

Fig. 4.3 (a) Spectrum of the regenerative Nd:YVO_4 amplifier seed pulse: red line corresponds to measured RA output spectrum; (b) autocorrelation trace of the regenerative amplifier output pulses. The retrieved pulse duration was 98 ps at FWHM when fitted with Gaussian function.

The second branch of the fiber laser was used to form pulses suitable for WLC generation. In the beginning, pulses were amplified to 2 nJ energy in Yb^{3+} doped fiber amplifier (Fig. 4.2). After the amplification pulse spectrum due to self-phase modulation (SPM) was broadened to ~14 nm in a single-mode polarisation-maintaining fiber (Fig. 4.4(a)).

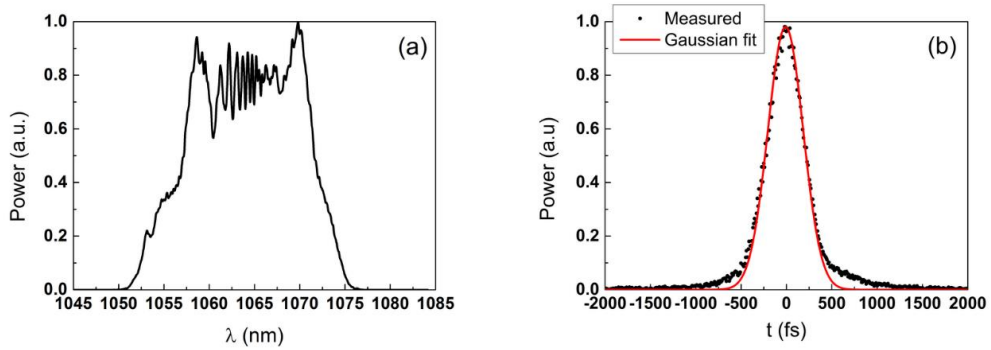

Fig. 4.4 (a) Spectrum of the OPA seed pulses; (b) Autocorrelation trace of the compressed pulses used to generate WLC. The retrieved compressed pulse duration was 325 fs at FWHM when fitted with Gaussian function.

This part of the fiber laser scheme together with ps OPA and grating compressor (Fig. 4.1) was actually an OPCPA stage inside the front-end for the main OPCPA. The scheme differed from the one described in Chapter 2.2. In order to optimise the parametric amplification stage of the spectrally broadened pulses from the fiber laser, pulse stretching in time domain was needed to be implemented. The desired ratio of signal and pump pulse duration was set to ~1.25 aiming to achieve high amplification efficiency and to smooth the oscillatory spectrum structure caused by SPM in fiber and improve compressed pulse contrast.

Before the experimental realisation, theoretical modelling was performed using numerical methods described in Chapter A. The model was simplified by omitting the pulse formation in a passively mode-locked fiber oscillator. The initial 2 ps duration transform-limited Gaussian pulses were amplified to 2.5 nJ pulse energy. Pulse spectrum broadening was achieved by propagating ultrashort pulses in a 15 m long SM PM fiber. Temporal and spectral envelope of the pulses after the propagation are shown in Fig. 4.5. A nearly flat-top 9 ps duration pulses were formed due to the interplay between dispersion and nonlinearity [156]. Pulse spectrum was broadened to approximately 14.5 nm.

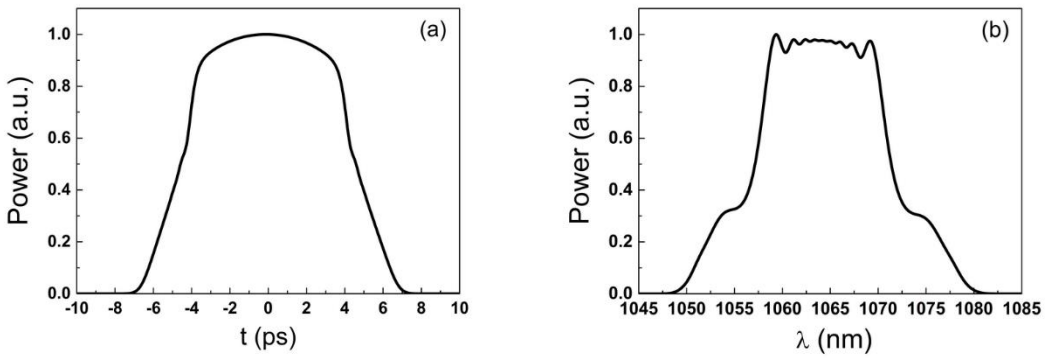

Fig. 4.5 Ultrashort pulses after the propagation in 15 m long single-mode PM fiber: (a) pulse temporal envelope; (b) pulse spectrum.

In order to stretch the pulses to 125 ps duration, sufficient amount of dispersion was numerically estimated, which resulted in the dispersion parameter to be equal to 8.3 ps/nm at 1064 nm central wavelength, corresponding to group velocity dispersion coefficient β_2 = 5.0 ps^2. Pulse

compression was modelled using the dispersion parameters of 1600 grooves/mm line density diffraction grating compressor working at Littrow angle (~58 deg). The optimal distance between the two gratings was determined by the maximum of the peak power of the pulse. Two cases of pulse compression were compared. First, the compression without compensation of TOD, induced by diffraction gratings, was modelled. Second, the residual TOD of the compressor was calculated (β_3 = 0.054 ps^3) and compensated at the stage of pulse stretching using CFBG. In this case, the amount of TOD accumulated from the SM PM fiber was neglected.

The results of pulse compression are pictured in Fig. 4.6. Modelling revealed a significant improvement in compressed pulse contrast, 2.8 times lower pulse duration and an increase of the pulse peak power by the factor of 6.3 when the TOD compensation was incorporated in the scheme. The compressed pulse duration was 78% of the transform-limited pulse duration calculated from the pulse spectrum. This difference was caused by the uncompensated TOD of the fiber stretcher and phase distortions due to the fiber nonlinearity.

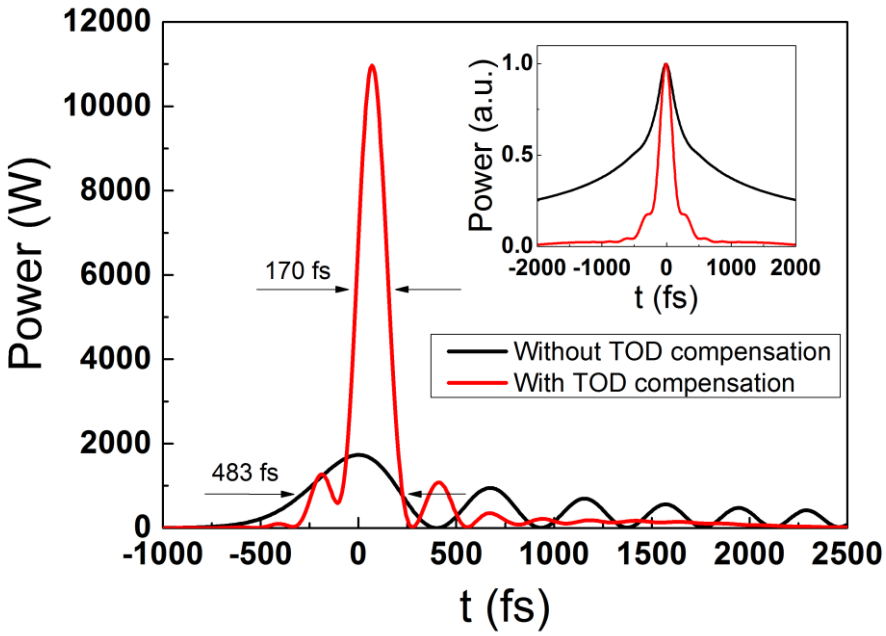

Fig. 4.6 Modelling results of the pulse compression including (red curves) and excluding (black curves) the compensation of TOD induced by diffraction grating compressor. Pulse envelopes are depicted in the main figure and corresponding autocorrelation traces in the inset.

Numerical calculations revealed that the use of CFBG stretcher with an optimised TOD coefficient is an efficient and sufficient solution to achieve pulses with an excellent contrast and nearly transform-limited pulse duration.

Concerning the results of theoretical calculations, after the spectral broadening pulses were stretched to 125 ps duration experimentally by a broadband CFBG3 (Fig. 4.2). The CFBG3 was designed in such a way that the second and the third-order dispersion of the CFBG3 was compensated by the grating compressor. After CFBG3 stretcher pulses were amplified in another fiber amplifier to 350 mW average power (10 nJ pulse energy) and directed to picosecond OPA.

Picosecond OPA and WLC generation

Pulses from DPSS laser were frequency doubled with 74% conversion efficiency (8.5 mJ@532 nm) in 6 mm length LBO crystal. Then the second harmonic pulses were split into two parts – the first was used as an OPA pump. 7 mm type I BBO picosecond OPA crystal (phase matching angle $\theta \approx 23^{o}$) was pumped by 2.5 mJ at 532 nm wavelength and produced 190 μJ amplified signal pulse energy. The parametric amplification factor was $1.9 \cdot 10^{4}$ with 7.6% pump energy conversion to signal wave. The pulse-to-pulse energy stability of the amplified signal measuring every pulse during 15 s period was ~0.6% rms which was comparable to the pump pulse stability which demonstrates that the parametric amplifier was working close to saturation regime. After picosecond OPA stage, pulses were compressed down to 325 fs duration (Fig. 4.4(b)) in a diffraction grating compressor. 1600 grooves/mm transmission diffraction gratings working in Littrow configuration were used. The efficiency of the compressor was 63%. The autocorrelation trace showed a good pulse contrast due to the third-order dispersion compensation of the diffraction grating compressor in the CFBG3 stretcher.

A small part (~1 μJ) of the parametrically amplified and compressed pulses was focused on a 5 mm sapphire plate to generate WLC. The spectrum of WLC was similar to the generated in Chapter 2.2, Fig. 2.2.8. Focusing conditions and

pulse energy were chosen to produce smooth and stable WLC. The remaining energy (115 μJ) was frequency doubled in a 2.5 mm thick BBO crystal with a ~57% efficiency (65 μJ@532 nm) and later used as a pump for femtosecond noncollinear OPA (fs NOPA). Parametric amplification was realised in a 1.2 mm thick BBO crystal (type I) at a phase matching angle $\theta = 24^{o}$ and a noncollinearity angle $\alpha \approx 2.4^{o}$ in order to reach the broadest amplification bandwidth [13,18]. The spot size of the pump beam in the crystal was adjusted to achieve the highest intensity but avoiding significant generation of the parametric fluorescence.

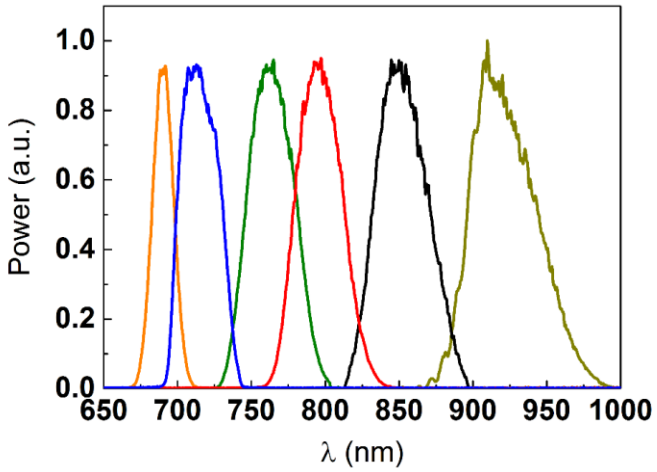

Fig. 4.7 Femtosecond NOPA output in a wavelength-tunable regime. The tuning range of the parametric amplifier output pulses was 670-1000 nm.

The aim of this experimental work was to realise a wavelength-tunable OPCPA. In order to achieve this, WLC pulses were stretched to ~1.2 ps in 10 mm thickness SF10 glass block. Wavelength tuning was performed by varying the delay between the pump and the chirped signal pulses in the femtosecond NOPA stage. Close to 300 fs duration pump pulse was slicing stretched WLC pulses during amplification in NOPA crystal and limiting their bandwidth. Pre-chirped WLC was amplified up to 8 μJ energy and spectra of the pulses corresponded to 30-35 fs transform-limited pulse durations (Fig. 4.7). The tuning range of NOPA output pulses was 670-1000 nm and was limited by the amplification bandwidth of BBO crystal at the phase matching conditions described before.

The OPCPA stage

For further amplification in the OPCPA stage, pulses were stretched to the duration of 40 ps by diffraction grating stretcher in Treacy configuration [107]. We used 1500 grooves/mm line density diffraction gratings. The efficiency of the stretcher was ~85%. Stretched pulse duration was chosen in order to optimise efficiency and bandwidth of the amplifier [72]. BBO crystal (type I) with the length of 7 mm was used for the OPCPA amplifier. Pulses were amplified up to 1 mJ energy by using 5 mJ 100 ps frequency doubled pump pulses from DPSS laser. Amplified pulse-to-pulse energy stability was 0.5% rms measuring every pulse during 15 s period. Offner-type compressor [106] with ~85% efficiency was used to recompress pulses after the amplification. The compressor consisted of one 1500 grooves/mm diffraction grating and two spherical concentric silver coated mirrors. The first mirror was concave (ROC = 500 mm) and the second was convex (ROC = -250 mm). When beam incidence angle to the diffraction grating of Offner compressor is equal to the one of Treacy stretcher, this stretcher-compressor tandem is self-compensating for all orders of dispersion [106,191].

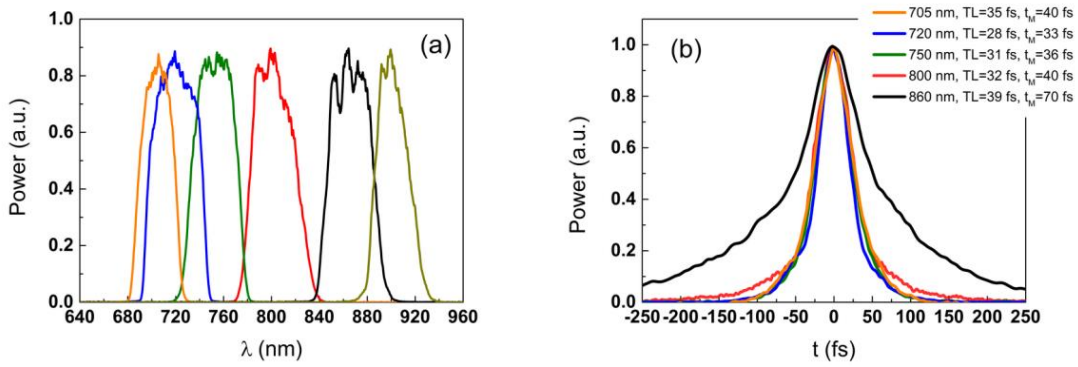

Fig. 4.8 (a) Pulse spectra at the OPCPA system output when performing wavelength tuning; (b) experimentally measured autocorrelation traces of the compressed pulses at different central wavelengths. The pulse duration was calculated at FWHM assuming Gaussian deconvolution parameter (~1.41). The legend shows the measured pulse duration (t_M) compared with transform limit calculated from the pulse spectrum.

The output spectra from the OPCPA at different central wavelengths are shown in Fig. 4.8(a). For each central wavelength, the distance between the diffraction grating and the concave mirror in Offner-type compressor was optimised to achieve the shortest pulse duration. The pulses were characterised

using multiple-shot SHG FROG autocorrelator. The mechanical construction of our experimental setup limited the pulse duration and contrast achieved throughout the full range of wavelength tuning (Fig. 4.8(b)). There was no possibility to properly align and equalise the critical geometric parameters of pulse stretcher and compressor performing the wavelength tuning at the same time. Such misalignment caused pulse phase distortions due to the third-order residual dispersion which can be clearly seen from the autocorrelation trace at 860 nm (Fig. 4.8(b)) where the measured pulse duration was nearly twice longer than the transform limit and had characteristic pedestal indicating uncompensated third-order dispersion. The stretcher-compressor scheme will be optimised in the near future and should lead to the compressed pulse duration of less than 40 fs in the whole tuning range.

In this experiment the alignment of pulse stretcher and compressor was optimised to achieve shortest pulse duration in the central wavelength range of 705-800 nm. The measured pulse durations in this range were less than 40 fs and close to the transform limit calculated from the pulse spectra (28-35 fs). We performed retrieval calculations of the pulse envelope using FROG algorithm [192] for the measurement at 750 nm central wavelength (Fig. 4.9).

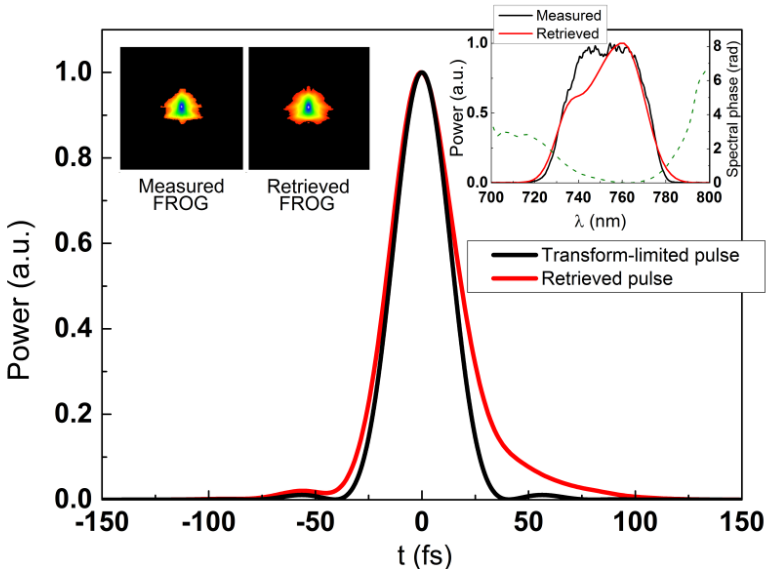

Fig. 4.9 Envelope of the compressed pulse retrieved from SHG FROG measurement at $\boldsymbol{\lambda_0}$ = 750 nm compared with transform-limited pulse calculated from the measured spectrum. Inset - measured pulse spectrum compared with retrieved spectrum and retrieved spectral phase (dashed green trace).

The FROG retrieval error was 0.38% on a 256×256 grid. The pulse duration calculated from the autocorrelation trace and FROG retrieval were identical and equal to 36 fs. As it can be seen from Fig. 4.9, a small amount of residual phase was still present after the optimisation of the compressor which resulted in an asymmetrical tail at the trailing edge of the pulse.

In order to characterise the beam quality at the output of the system, we measured the beam radius versus the distance from the beam waist. At low amplified pulse energy (<0.3 mJ) the beam quality parameter M^2 was 1.21 (Fig. 4.10(a)). At the highest achievable pulse energy, the beam quality got worse (M^2 = 1.52) (Fig. 4.10(b)) likely due to parametric back-conversion at the peak of Gaussian beam in the BBO crystal.

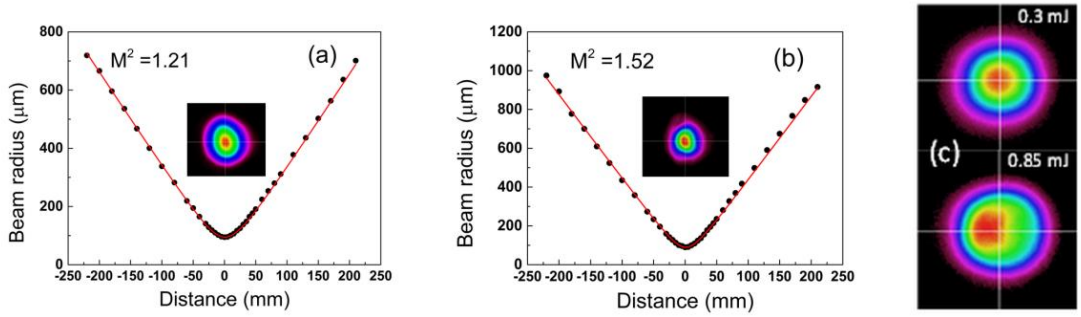

Fig. 4.10 4σ beam radius at the system output versus distance from the waist location measured (a) at low output pulse energy (<0.3 mJ) and (b) at the highest achievable pulse energy at the system output (0.85 mJ); (c) beam profiles at the plane of OPCPA crystal at 0.3 mJ and 0.85 mJ amplified pulse energies.

This effect was verified by measuring amplified signal beam profile at the plane of BBO crystal perpendicular to propagation axis using 4-f imaging lens system (Fig. 4.10(c)). At the maximum pump intensity, the peak of the beam profile shifted from the beam center due to parametric back-conversion and walk-off.

Conclusions

A compact femtosecond tunable OPCPA system with a picosecond monolithic fiber seed laser and a picosecond DPSS pump laser was developed. Pulses from the fiber laser were spectrally broadened in optical fiber, parametrically amplified, compressed to femtosecond duration and then used to generate white-light supercontinuum signal which was later preamplified in a

femtosecond broadband noncollinear optical parametric amplifier. After OPCPA amplifier and compressor high spatio-temporal quality pulses with energy up to 0.85 mJ and pulse duration down to sub-40 fs (>20 GW peak power) were obtained. Wavelength tunability in the spectral range of 680-930 nm was experimentally demonstrated.

This concept opens a path for the development of compact femtosecond high energy tunable hybrid laser systems, incorporating advantages of fiber and solid-state laser technologies, which may be adopted in a variety of ultrafast laser applications.

A Modelling methodology

Methods of modelling the ultrashort pulse propagation, formation and dynamics in fiber lasers covered in all subsections of this chapter were programmed into a user-friendly software package. This software was used to produce all the calculations mentioned in Chapters 2-4. Furthermore, most of these programmed models were implemented in the theoretical analysis of a high energy FCPA system presented by J. Želudevičius et al. [101].

A.1 Ultrashort pulse propagation in a single-mode fiber

The ultrashort pulse propagation in fiber is described by the Nonlinear Schrödinger Equation (NLSE) which is derived from Maxwell's equations using the slowly varying envelope approximation [156,193]. In this work, for pulse propagation in the polarization-maintaining (PM) single-mode (SM) fiber the most common form of NLSE was modelled:

$$\frac{\partial A}{\partial z} + \frac{i\beta_2}{2}\frac{\partial^2 A}{\partial t^2} - \frac{\beta_3}{6}\frac{\partial^3 A}{\partial t^3} = \frac{g(\omega) - \alpha}{2}A + i\gamma|A|^2 A, \qquad \text{(A.1.1)}$$

where $A(z,t)$ is the slowly varying pulse envelope, β_2 is the group velocity dispersion (GVD) parameter, β_3 is the third-order dispersion (TOD) parameter, α is the absorption coefficient, γ is the nonlinearity parameter:

$$\gamma = \frac{n_2\omega_0}{cA_{eff}}, \qquad \text{(A.1.2)}$$

where n_2 is the nonlinear refractive index, $n_2 \approx 2.2\cdot10^{-20}$ m^2/W for typical silica fibers [156], ω_0 is the central angular frequency of operation, c is the speed of light and A_{eff} is the effective fiber mode area. The optical frequency dependent gain coefficient $g(\omega)$ was used for the calculations of pulse propagation in amplification stages. Generally, when the fiber amplifier was far from gain saturation, $g(\omega)$ was calculated according to the desired pulse energy at the output of the active fiber taking into account the absorption and emission cross-sections of Yb^{3+}. This is detailed further in Chapter A.2. The full model of the

fiber amplifier including the effects of gain saturation and excited state dynamics is described in Chapter A.3. It was used for modelling of large-mode-area (LMA) fiber amplifiers.

In the following subsections, the effects of different terms of NLSE to the ultrashort pulse propagating along the fiber is presented and the methods of numerical modelling are explained.

Chromatic dispersion

Electromagnetic field propagating through the dielectric interacts with the bound electrons of the medium causing them to move in an oscillating motion which depends on the optical frequency of the field. If the field consists of a set of different frequencies, the medium response will be different for each of them. This characteristic of the material is known as a chromatic dispersion which acts through the frequency dependent refractive index $n(\omega)$. Far from the resonance frequencies at which medium absorbs the electromagnetic radiation, the refractive index is approximated by the Sellmeier formula [156]:

$$n^2(\omega) = 1 + \sum_{j=1}^{m} \frac{B_j \omega_j^2}{\omega_j^2 - \omega^2}, \tag{A.1.3}$$

where ω_j is the resonance frequency, B_j is the strength of the resonance. These parameters can be obtained from experimental dispersion measurements by fitting the curves to the equation (A.1.3). The Sellmeier equation for fused silica consists of three-term sum with parameters given in Table A.1.1.

B_1	B_2	B_3	λ_1	λ_2	λ_3
0.6961663	0.4079426	0.8974794	0.0684043 μm	0.1162414 μm	9.896161 μm

Table A.1.1 Sellmeier coefficients for fused silica glass, $\boldsymbol{\lambda_j = 2\pi c/\omega_j}$.

Fiber dispersion becomes very important when ultrashort pulses are propagated, because different spectral components of the pulse travel at different speeds $v = c/n(\omega)$. The effects of dispersion are included in NLSE by expanding the propagation constant β in Taylor series:

$$\beta(\omega) = n(\omega)\frac{\omega}{c} = \beta_0 + \beta_1(\omega - \omega_0) + \frac{1}{2}\beta_2(\omega - \omega_0) + \frac{1}{6}\beta_3(\omega - \omega_0) + \ldots, \tag{A.1.4}$$

$$\beta_m = \left(\frac{d^m\beta}{d\omega^m}\right)_{\omega=\omega_0}. \tag{A.1.5}$$

Ultrashort pulse envelope propagates at the group velocity β_1^{-1}. Parameter β_2 is called the group velocity dispersion (GVD) and is responsible for pulse broadening. β_2 can be converted into dispersion parameter D which is widely used in fiber optics communications:

$$D = -\frac{2\pi c}{\lambda^2}\beta_2. \tag{A.1.6}$$

The variation of β_2 and D according to the wavelength is shown in Fig. A.1.1(a). GVD parameter is equal to zero at ~1.27 μm and becomes negative at longer wavelengths. This wavelength is known as the zero-dispersion wavelength. Spectral region where parameter β_2 has positive values is called the normal dispersion region. In this region, longer wavelengths of the pulse propagate faster in time than the shorter ones. The opposite occurs in the anomalous dispersion region, where β_2 becomes negative. The wavelength region of 1000-1100 nm is emphasized in the graph as it is the spectral range of operation for Yb-based fiber lasers, which were studied and experimentally used in this doctoral dissertation.

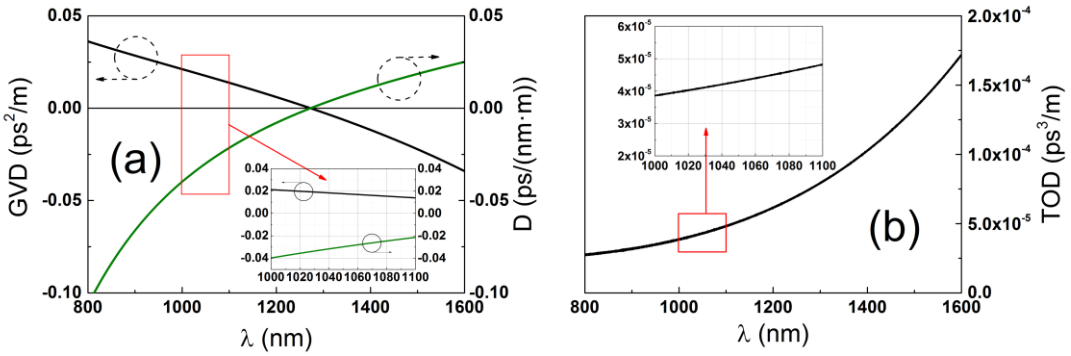

Fig. A.1.1 Chromatic dispersion in fused silica glass: (a) variation of GVD parameter $\boldsymbol{\beta_2}$ and dispersion coefficient $\boldsymbol{D}$ according to the wavelength; (b) variation of TOD parameter $\boldsymbol{\beta_3}$. The wavelength range of 1000-1100 nm which is important for Yb-based fiber lasers is emphasized in the insets of the figures.

At some cases the cubic term of the expanded propagation constant (A.1.4) becomes important. It starts to play the dominant role near the zero-dispersion wavelength or if the group velocity dispersion of an optical fiber is somehow compensated (refer to the Chapter A.4). Furthermore, it is necessary to include β_3 term for less than 100 fs duration pulses, where the ratio $\frac{\Delta\omega}{\omega_0}$ is large enough for the cubic term to be significant. Coefficient β_3 which appears at the cubic term is known as the third order dispersion (TOD) parameter. Using β_3 and β_2 values, dispersion slope coefficient S which is a popular characteristic of optical fibers can be calculated:

$$S = \frac{dD}{d\lambda} = \frac{4\pi^2 c^2}{\lambda^4}\beta_3 + \frac{4\pi c}{\lambda^3}\beta_2. \qquad \text{(A.1.7)}$$

Numerically calculated dispersion parameter values of silica glass for the characteristic wavelengths of Yb-based fiber lasers are stated in Table A.1.1.

	β_2	D	β_3	S
1030 nm	$18.9\cdot10^{-3}$ ps^2/m	$-33.7\cdot10^{-3}$ ps/(nm·m)	$4.12\cdot10^{-5}$ ps^3/m	$1.95\cdot10^{-4}$ ps/(nm^2·m)
1064 nm	$16.5\cdot10^{-3}$ ps^2/m	$-27.4\cdot10^{-3}$ ps/(nm·m)	$4.43\cdot10^{-5}$ ps^3/m	$1.74\cdot10^{-4}$ ps/(nm^2·m)

Table A.1.2 Dispersion parameters of silica glass for characteristic wavelengths of Yb-based fiber lasers.

It is important to indicate that these values differ from the calculated for the actual optical fibers because of the small concentrations of dopants such as GeO_2 and P_2O_5 which constitute the fiber. Moreover, the waveguiding effect in fiber causes the effective mode index to become lower than the material index $n(\omega)$. Therefore, it is recommended to estimate the dispersion parameters comparing with the experimental measurements for a particular fiber.

The effect of group velocity dispersion

Dominance of either dispersion or nonlinearity effects depend on the initial parameters of the ultrashort pulse which are the pulse width T_0 and the peak power P_0. It is convenient to establish the dispersion and nonlinearity lengths (L_D and L_{NL}), on which relative magnitudes depend the evolution of pulse envelope and spectrum. According to these parameters, NLSE (A.1.1) for the

pulse propagation along the passive fiber ($g(\omega) = 0$) can be changed into so called normalized form [156]:

$$i\frac{\partial U}{\partial z} = \frac{\mathrm{sgn}(\beta_2)}{2L_D}\frac{\partial^2 U}{\partial \tau^2} - \frac{\exp(-\alpha z)}{L_{NL}}|U|^2 U, \tag{A.1.8}$$

$$\tau = \frac{T}{T_0} = \frac{t - z/\beta_1^{-1}}{T_0}, \tag{A.1.9}$$

$$U(z,\tau) = \frac{A(z,\tau)}{\sqrt{P_0}\exp(-\alpha z/2)}, \tag{A.1.10}$$

$$L_D = \frac{T_0^2}{|\beta_2|}, \qquad L_{NL} = \frac{1}{\gamma P_0}, \tag{A.1.11}$$

where P_0 is the peak power, $\mathrm{sgn}(\beta_2) = \pm 1$ according to the sign of the parameter β_2, t is substituted by T in order to eliminate the group velocity term using the so-called retarded frame of reference and T_0 corresponds to the half-width at $1/e$ intensity point.

Dispersion regime dominates when such relation is satisfied:

$$\frac{L_D}{L_{NL}} = \frac{\gamma P_0 T_0^2}{|\beta_2|} \ll 1. \tag{A.1.12}$$

The effect of GVD on the ultrashort pulse is studied by setting the nonlinearity parameter γ to zero and neglecting fiber losses. Then NLSE is simplified to the form:

$$i\frac{\partial U}{\partial z} = \frac{\beta_2}{2}\frac{\partial^2 U}{\partial T^2}. \tag{A.1.13}$$

This equation can be solved in the Fourier domain. If $\widetilde{U}(z,\omega)$ is the Fourier transform of $U(z,T)$, then:

$$U(z,T) = \frac{1}{2\pi}\int_{-\infty}^{\infty}\widetilde{U}(z,\omega)\exp(-i\omega T)d\omega, \tag{A.1.14}$$

$$i\frac{\partial \widetilde{U}}{\partial z} = -\frac{\beta_2}{2}\omega^2\widetilde{U}, \tag{A.1.15}$$

which gives the solution:

$$\tilde{U}(z,\omega) = \tilde{U}(0,\omega)\exp\left(i\frac{\beta_2}{2}\omega^2 z\right). \tag{A.1.16}$$

This solution shows that GVD changes the phase of each spectral component of the pulse depending on the parameter β_2, frequency ω and the propagated distance z. These changes do not affect the form of the pulse spectrum, but has an impact to the pulse envelope. The general solution in time domain is given using equation (A.1.16) in (A.1.14):

$$U(z,T) = \frac{1}{2\pi}\int_{-\infty}^{\infty}\tilde{U}(0,\omega)\exp\left(i\frac{\beta_2}{2}\omega^2 z - i\omega T\right)d\omega, \tag{A.1.17}$$

where $\tilde{U}(0,\omega)$ is the initial pulse spectrum.

Ultrashort pulses were considered to have an initial Gaussian form throughout the numerical calculations, where the passively mode-locked oscillator was not modelled. It is proven in Chapter 2.2 that Gaussian function is close to an experimental approximation to describe the envelope of the incident field. The most common function describing the pulse with the peak amplitude U_0 and chirp parameter C is [194]:

$$U(0,T) = U_0\exp\left[-\frac{1+iC}{2}\left(\frac{T}{T_0}\right)^2\right], \tag{A.1.18}$$

$$T_{FWHM} = 2\sqrt{\ln 2}\,T_0. \tag{A.1.19}$$

Setting the chirp parameter C to zero and normalizing the pulse ($U_0 = 1$), the solution of equation (A.1.17) is:

$$U(z,T) = \frac{T_0}{\sqrt{T_0^2 - i\beta_2 z}}\exp\left(-\frac{T^2}{2(T_0^2 - i\beta_2 z)}\right), \tag{A.1.20}$$

thus the pulse remains Gaussian-shaped during the propagation, but its temporal width increases with z:

$$T(z) = T_0\sqrt{1+\left(\frac{\beta_2 z}{T_0^2}\right)^2} = T_0\sqrt{1+\left(\frac{z}{L_D}\right)^2}. \tag{A.1.21}$$

As an example, 1 ps duration pulses centered at 1064 nm wavelength were propagated along the SM PM fiber which length was equal to L_D. According to

the relation (A.1.21), the resulting pulse duration was ~1.41 ps after 22 m of propagation ($\beta_2 = 0.0165$ ps^2). Although the initial pulse exhibited no chirp, the pulse was up-chirped at the end of the fiber. The pulse phase ϕ became modulated during the propagation and dependent on the propagation distance. It is shown in [156], that this effect causes the linear instantaneous frequency change across the pulse, in the other words – the linear chirp:

$$\delta\omega(T) = -\frac{\partial\phi}{\partial T} = \frac{\mathrm{sgn}(\beta_2)(2z/L_D)}{1+(z/L_D)^2}\frac{T}{T_0^2}. \tag{A.1.22}$$

In the modelled case, dispersion coefficient β_2 was positive, thus the longer wavelengths were located at the leading edge of the pulse. It is worth mentioning that the minus sign at the derivative $\partial\phi/\partial T$ in equation (A.1.22) comes due to the particular initial form of the electric field which was chosen during the NLSE derivation in [156].

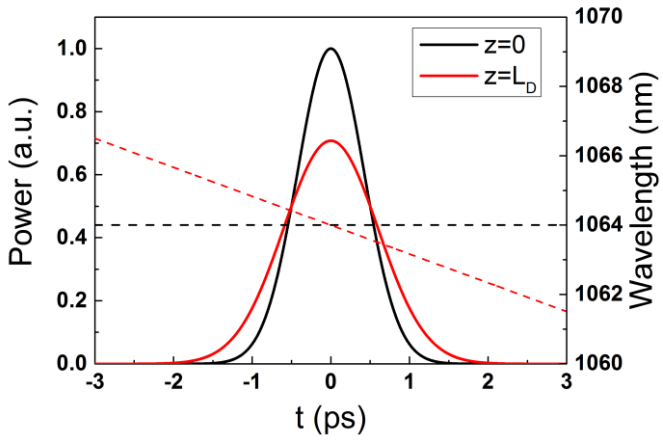

Fig. A.1.2 Ultrashort pulse broadening induced by GVD during the propagation along the SM PM fiber. For consistency purposes, the instantaneous frequency across the pulse is expressed in units of wavelength in this thesis.

The effect of third-order dispersion

In order to study the effects of TOD, equation (A.1.13) should be expanded including the cubic term of the propagation constant β (A.1.4):

$$i\frac{\partial U}{\partial z} = \frac{\beta_2}{2}\frac{\partial^2 U}{\partial T^2} + i\frac{\beta_3}{6}\frac{\partial^3 U}{\partial T^3}. \tag{A.1.23}$$

This equation can be solved using the Fourier method in the same manner as in the previous subsection. The resulting solution is:

$$U(z,T) = \frac{1}{2\pi}\int_{-\infty}^{\infty} \tilde{U}(0,\omega)\exp\left(i\frac{\beta_2}{2}\omega^2 z + i\frac{\beta_3}{6}\omega^3 z - i\omega T\right)d\omega. \qquad \text{(A.1.24)}$$

In order to compare the importance of GVD and TOD terms, the third order dispersion length can be introduced:

$$L_T = \frac{T_0^3}{|\beta_3|}. \qquad \text{(A.1.25)}$$

The effect of TOD become dominant when $L_T \leq L_D$ or $T_0|\beta_2/\beta_3| \leq 1$. This condition could be satisfied only for less than 10 fs duration pulses at 1064 nm wavelength, if the standard SM PM fiber is used, which is not relevant with the fiber lasers investigated in this thesis. A closer to experimental situation can be modelled by setting the β_2 parameter to zero and assuming that only the residual TOD acts on the pulse. Such an example is shown in Fig. A.1.3. Initial 100 fs duration pulses were propagated through $z = L_T$ length fiber. It is seen from the picture that TOD distorted the pulse envelope: it became asymmetric with a damped oscillatory structure at the trailing edge of the pulse. This is the case for a positive β_3 coefficient. The effect would be inverted in time domain for the negative values of β_3. Such distorted pulse envelope is a typical result after the pulse compression in FCPA systems using the diffraction grating compressor with no TOD compensation [195].

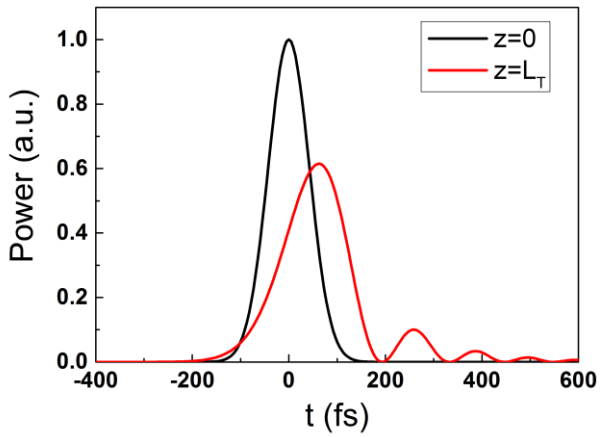

Fig. A.1.3 The effect of TOD: pulse envelope after the propagation in $\boldsymbol{z = L_T}$ length SM PM fiber. The GVD coefficient $\boldsymbol{\beta_2}$ was set to zero, $\boldsymbol{\beta_3}$=4.43·10^{-5} ps^3.

The effect of self-phase modulation

In order to separately analyse the impact of SPM to the ultrashort pulse, terms including the effects of dispersion should be neglected in NLSE. The conditions of such simplification appear from the previously introduced length scales L_D and L_{NL} (A.1.11). Generally, the pulse duration and peak power should satisfy the inequality $L_D \gg L > L_{NL}$ for a fiber length L. This is the case for relatively wide pulses with a large peak power. The normalized form of NLSE, omitting the fiber losses, becomes:

$$\frac{\partial U}{\partial z} = i\frac{1}{L_{NL}}|U|^2 U. \tag{A.1.26}$$

The equation can be solved by expressing the amplitude as $U = V\exp(i\phi_{NL})$ and separating the equation (A.1.26) for the real and the imaginary parts. This leads to:

$$\frac{\partial V}{\partial z} = 0, \qquad \frac{\partial \phi_{NL}}{\partial z} = \frac{1}{L_{NL}}V^2, \tag{A.1.27}$$

$$\phi_{NL}(L,T) = \frac{L}{L_{NL}}|U(0,T)|^2. \tag{A.1.28}$$

The amplitude does not change while propagating along the fiber and the phase equation can be solved analytically:

$$U(L,T) = U(0,T)\exp\left[i\phi_{NL}(L,T)\right]. \tag{A.1.29}$$

This solution shows that the nonlinear term includes a power dependence in pulse phase, the effect which is known as self-phase modulation (SPM). The time profile of the pulse remains unchanged. However, a temporally varying phase causes the instantaneous frequency to differ across the pulse from the central value ω_0:

$$\delta\omega(T) = -\frac{\partial \phi_{NL}}{\partial T} = -\frac{L}{L_{NL}}\frac{\partial}{\partial T}|U(0,T)|^2. \tag{A.1.30}$$

The time-dependent $\delta\omega$ is called the frequency chirp. The chirp's magnitude increases with the propagated distance. This means that the pulse itself generates new frequency components continuously during the propagation in fiber. These components broaden the pulse spectrum from its initial width.

In order to determine the pulse spectrum broadening factor, an initial unchirped Gaussian pulse is taken as an example (A.1.18). According to the equation (A.1.30), frequency chirp for such pulse is:

$$\delta\omega(T) = \frac{L}{L_{NL}}\frac{2T}{T_0^2}\exp\left[-\left(\frac{T}{T_0}\right)^2\right]. \tag{A.1.31}$$

By setting the time derivative of this function to zero, the maximum value $\delta\omega_{max}$ can be determined. For the unchirped Gaussian pulse, introducing the spectral half-width (at $1/e$ intensity point) $\Delta\omega_0 = T_0^{-1}$, this value is equal to [156]:

$$\delta\omega_{max} = 0.86\Delta\omega_0\frac{L}{L_{NL}}. \tag{A.1.32}$$

A more unified quantity to describe the amount of the accumulated nonlinear phase during the pulse propagation is called the B-integral. It is defined by [49,196]:

$$B = \frac{2\pi}{\lambda_0}n_2\int_0^L P(z)dz. \tag{A.1.33}$$

where $P(z)$ is the peak power of the pulse in time domain as a function of the position along the fiber. B-integral is usually used to characterize the pulses in FCPA systems [190]. The impact of SPM on pulse spectrum for an initial unchirped Gaussian pulse at different values of B-integral is presented in Fig. A.1.4. The characteristic SPM-broadened pulse spectrum in a highly nonlinear propagation regime is an oscillatory structure, symmetric about the central wavelength.

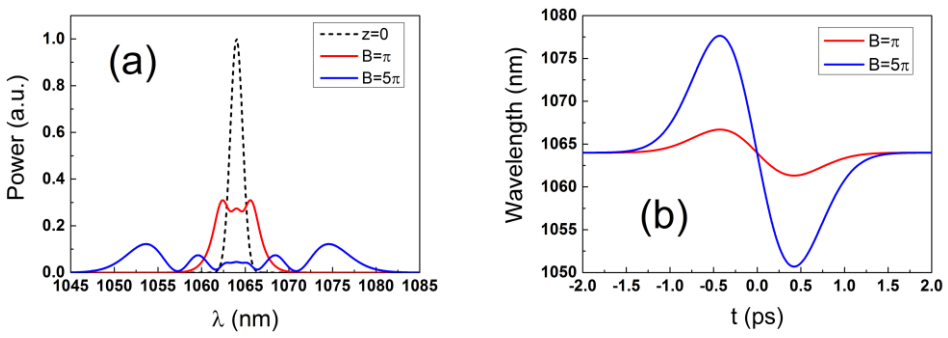

Fig. A.1.4 The effects of SPM on pulse spectrum: (a) SPM-broadened pulse spectra at different B-integral values and (b) corresponding pulse frequency chirp.

Such spectral distribution can be explained from the SPM chirp graph in Fig. A.1.4(b). Despite the extrema points, the chirp has the same values at two different times. These values represent two identical frequency waves with distinct phases which interfere constructively or destructively with each other according to the phase difference. The longer wavelengths are located at the leading part of the pulse, while the shorter – at the trailing part. The chirp is quasi-linear and positive at a particular part of the pulse around the central frequency. This feature of SPM-based frequency modulation gives an opportunity to compress the pulse with a broadened spectrum to a shorter than initial duration, which is quite often employed in FCPA systems [101,197,198]. The interplay between GVD and SPM effects cause different pulse propagation dynamics depending on parameters β_2, γ and the initial pulse shape. These combined effects are well presented in [156].

Split-step Fourier method for NLSE modelling

The NLSE is a nonlinear partial differential equation which, in general, does not have analytic solutions. Therefore, numerical methods must be implemented to study the effects of dispersion and nonlinearity in optical fibers. One of the most popular approaches used to model the NLSE is the split-step Fourier method [156].

In order to explain the theory of split-step method, equation (A.1.1) should be rewritten in the form:

$$\frac{\partial A}{\partial z} = \left(\widehat{D} + \widehat{N}\right)A, \tag{A.1.34}$$

$$\widehat{D} = -\frac{i\beta_2}{2}\frac{\partial^2}{\partial T^2} + \frac{\beta_3}{6}\frac{\partial^3}{\partial T^3} - \frac{\alpha}{2}, \tag{A.1.35}$$

$$\widehat{N} = i\gamma|A|^2. \tag{A.1.36}$$

The differential operator $\widehat{D}$ includes the effects of dispersion and fiber losses and the nonlinear operator $\widehat{N}$ is responsible for the effects of fiber nonlinearities. In practice, the dispersion and nonlinearity effects operate together during the pulse propagation along the fiber. The main idea of the split-step Fourier method is to approximate the solution of NLSE by considering that in a very small

propagation distance h these effects can be assumed as acting independently. Propagation from z to $z + h$ is calculated in two steps. In the first step, the dispersion acts alone ($\widehat{N} = 0$) and then only the nonlinearity operator is included in the second step ($\widehat{D} = 0$):

$$A(z + h, T) \approx \exp\left(h\widehat{D}\right) \exp\left(h\widehat{N}\right) A(z, T). \quad \text{(A.1.37)}$$

The dispersion part is evaluated in the Fourier domain:

$$\exp\left(h\widehat{D}\right) A(z, T) = \frac{1}{\zeta} F_T^{-1}\left[\exp\left(h\widehat{D}(-i\omega)\right)\zeta F_T[A(z, T)]\right], \quad \text{(A.1.38)}$$

where F_T is the Fourier transformation operation, ζ is the normalization constant required to satisfy the Parseval's theorem [199] and $\widehat{D}(-i\omega)$ is calculated by replacing $\partial^n/\partial T^n$ by $(-i\omega)^n$ in the Fourier domain.

In order to improve the accuracy of this calculation method, a symmetrized split-step scheme can be used, in which the equation (A.1.37) is replaced by:

$$A(z + h, T) \approx \exp\left(\frac{h}{2}\widehat{D}\right) \exp\left(h\widehat{N}\right) \exp\left(\frac{h}{2}\widehat{D}\right) A(z, T). \quad \text{(A.1.39)}$$

The accuracy can be further improved by evaluating the nonlinearity term using the 4th order Runge-Kutta method [200]. This becomes important when higher-order nonlinear effects are included in modelling [156].

A.2 Passively mode-locked oscillator

Modelling of a passively mode-locked fiber oscillator operating in the soliton regime is based on a converging method of repeated iterations which was described by J. Lægsgaard et al. in [201]. The ultrashort pulse is circulated in the cavity of the oscillator's resonator under the action of different laser components until a stable solution is achieved. Principal scheme of the all-in-fiber oscillator used in the numerical calculations is pictured in Fig. A.2.1.

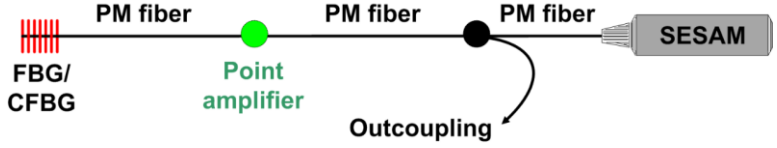

Fig. A.2.1 Modelling scheme of the all-in-fiber oscillator: initial Gaussian shape pulse is propagated through the polarisation-maintaining (PM) fiber calculating the response of active and passive cavity components. Propagation is repeated until the convergence condition is achieved.

At the beginning of the calculation, initial pulse is described using a Gaussian function. This pulse is propagated through the elements that constitute the resonator: chirped or unchirped fiber Bragg grating (FBG/CFBG), Yb^{3+} doped active fiber which is simplified to a point amplifier, beam splitter and a semiconductor saturable absorber mirror (SESAM). Between these components the ultrashort pulse propagation in a single-mode polarization maintaining (PM) fiber is modelled. The difference of output pulse energy values in present and previous iteration is tracked and compared with the predefined parameter of tolerance until the steady-state is reached:

$$\varepsilon = \left| \int_{-t}^{t} I_n(t)dt - \int_{-t}^{t} I_{n-1}(t)dt \right|, \tag{A.2.1}$$

where the intensity of the pulse I is integrated according to the time t in an initially defined time window of the calculation. This corresponds to the pulse energy. Letter n denotes the number of iteration.

The next subsections will be dedicated to describing the methods used to calculate the response of cavity elements of the all-in-fiber oscillator. The pulse propagation equation derivation and modelling were already explained in subsection A.1.

Fiber Bragg grating

Principles for understanding and methods for calculating the characteristics of fiber gratings are described in detail by T. Erdogan and R. Kashyap [187,202]. In this subsection, a brief theory of gratings and particular type gratings simulated using a modelling software are discussed.

A spatially varying pattern of ultraviolet light intensity exposed on an optical fiber is used to produce fiber phase gratings. This results in a perturbation to the effective refractive index for the guided fiber modes. Common types of induced index change δn_{eff} variations along the fiber axis z are pictured in Fig. A.2.2. These variations mainly determine the optical properties of the fiber grating.

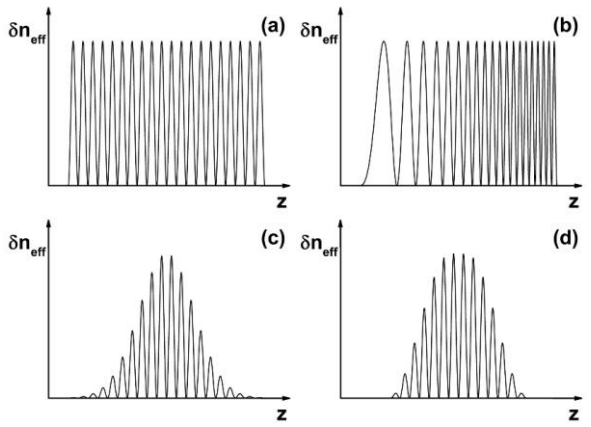

Fig. A.2.2 Types of fiber gratings used in the modelling program with distinct index modulation: (a) uniform; (b) chirped; (c) Gaussian-apodized; (d) raised-cosine-apodized.

The incidence of a light wave on the fiber grating is described using the same equation as for the optical diffraction grating:

$$n \sin \theta_2 = n \sin \theta_1 + m \frac{\lambda}{\Lambda}, \tag{A.2.2}$$

where θ_1 is the incidence angle, θ_2 is the angle of diffraction, λ – wavelength of the incident light, Λ – period of the grating, n – refractive index and m indicates the diffraction order. Using this equation, the wavelength at which fiber grating couples light between two modes most efficiently can be determined.

If the coupling occurs between the modes propagating in opposite directions, such grating is classified as fiber Bragg grating (FBG) or reflection grating. The name comes from a Bragg‘s law which describes the condition of constructive interference of X-ray radiation in a periodically spaced crystalline structure [203].

Light propagation through periodically changing higher and lower refractive index regions of FBG is led by a partial reflection at each interface between those regions. The spacing between the regions is chosen in such way that for specific wavelengths of light all partial reflections sum up in phase, thus due to the constructive interference the total reflection will grow up to the maximum value. All other wavelengths are reflected out of phase and cancel each other, which results in high transmission [204]. The simplified scheme of reflection by FBG of a single core mode with a bounce angle θ_1 to the same mode propagating in the opposite direction with an angle $\theta_2 = -\theta_1$ is pictured in Fig. A.2.3.

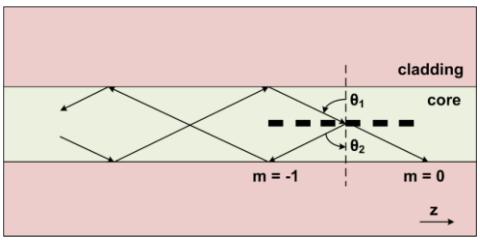

Fig. A.2.3 Illustration of a core mode Bragg reflection by FBG. Adapted from [202].

The propagation constant β for the core mode is:

$$\beta = \frac{\omega n_{eff}}{c} = \frac{2\pi}{\lambda} n_{co} \sin\theta, \tag{A.2.3}$$

where θ is the bounce angle. According to this, equation (A.2.2) can be rewritten for guided modes:

$$\beta_2 = \beta_1 + m\frac{2\pi}{\Lambda}. \tag{A.2.4}$$

First-order diffraction dominates in FBG, thus $m = -1$. If equation (A.2.4) is used stating that $\beta_2 < 0$ as negative values of the propagation constant describe propagation in *-z* direction, the resonant wavelength for reflection of two identical n_{eff} index modes is:

$$\lambda_B = 2n_{eff}\Lambda, \tag{A.2.5}$$

which is called the Bragg wavelength and the relation - the Bragg condition.

A coupled-mode propagation theory is used to analyse the properties of fiber gratings. The detailed derivation of the theory is presented in various books [187,205]. A coupled-mode theory states that the transverse component of the electric field can be written as a superposition of ideal modes travelling in $+z$ and *-z* directions. The modes are orthogonal in the ideal waveguide and do not exchange energy. Dielectric perturbation such as in fiber gratings causes modes to couple. The resulting coupled-mode equations for FBG are:

$$\frac{dR}{dz} = i\hat{\sigma}R(z) + i\kappa S(z), \tag{A.2.6}$$

$$\frac{dS}{dz} = -i\hat{\sigma}S(z) - i\kappa^* R(z), \tag{A.2.7}$$

where *R(z)* and *S(z)* are the expressions of forward (reference) and backward (signal) propagating modes respectively, κ is so called „AC“ coupling

coefficient and $\widehat{\sigma}$ is a „dc“ self-coupling coefficient, which consists of detuning δ, coupling σ and the z-dependent phase term which denotes the chirp parameter in the period of the grating:

$$\widehat{\sigma} = \delta + \sigma - \frac{1}{2}\frac{d\phi}{dz}. \tag{A.2.8}$$

Coupling coefficient σ affects propagation as it causes the change in the average refractive index of the mode. The detuning δ is independent of z and expressed in such relation:

$$\delta = 2\pi n_{eff}\left(\frac{1}{\lambda} - \frac{1}{\lambda_B}\right). \tag{A.2.9}$$

When $\delta = 0$, the Bragg condition is satisfied. For a single-mode uniform FBG (Fig. A.2.2(a)) the relations are simplified:

$$\widehat{\sigma} = \delta + \frac{2\pi}{\lambda}\overline{\delta n}_{eff}, \tag{A.2.10}$$

$$\kappa = \kappa^* = \frac{\pi}{\lambda}\Gamma\overline{\delta n}_{eff}, \tag{A.2.11}$$

where the modulation parameter $\overline{\delta n}_{eff}$ is the refractive index change spatially averaged over grating period and Γ is the core power confinement factor [194]:

$$\Gamma = 1 - \exp\left(-\frac{2a^2}{w^2}\right), \tag{A.2.12}$$

in which w is the field radius and a is the core radius of the fiber.

Equations (A.2.6) and (A.2.7) become coupled first-order ordinary differential equations with constant coefficients when uniform single-mode FBG is modelled. The analytical solutions can be found applying the boundary conditions. It is assumed that the amplitude of the incidence field from $-\infty$ at the entrance of the grating of length L is equal to 1 ($R\left(-\frac{L}{2}\right) = 1$) and the back-propagating “signal” field is equal to 0 at the output end of FBG ($S\left(-\frac{L}{2}\right) = 0$). Then the complex amplitude ($S(-\frac{L}{2})/R(-\frac{L}{2})$) and power reflection coefficients respectively are equal to:

$$\rho = \frac{-\kappa \sinh\left(\sqrt{\kappa^2 - \hat{\sigma}^2}L\right)}{\hat{\sigma}\sinh\left(\sqrt{\kappa^2 - \hat{\sigma}^2}L\right) + i\sqrt{\kappa^2 - \hat{\sigma}^2}\cosh\left(\sqrt{\kappa^2 - \hat{\sigma}^2}L\right)}, \tag{A.2.13}$$

$$R = |\rho|^2 = \frac{\sinh^2\left(\sqrt{\kappa^2 - \hat{\sigma}^2}L\right)}{\cosh^2\left(\sqrt{\kappa^2 - \hat{\sigma}^2}L\right) - \frac{\hat{\sigma}^2}{\kappa^2}}. \tag{A.2.14}$$

The zero-centered length L is used due to the convenience. Then an unshifted symmetrical function such as Gaussian can be used to modulate the variation of refractive index through the grating length. The maximum reflectivity of the Bragg grating from (A.2.14) is:

$$R_{max} = \tanh^2(\kappa L). \tag{A.2.15}$$

Most practical applications require non-uniform fiber gratings. A piecewise-uniform approach is used to calculated reflection spectrum of the two-mode coupled non-uniform grating [202]. In this method, a non-uniform grating is divided into a number uniform pieces. The solutions for each piece are combined by multiplying the matrixes of the corresponding pieces. Increasing the number of uniform pieces leads to the convergence of the solutions to sufficiently accurate values.

Modelling the apodized gratings require using a z-dependent "dc" self-coupling coefficient $\hat{\sigma}(z)$ and modify the modulation parameter $\overline{\delta n}_{eff}$ at each uniform piece according to the apodization profile function. The Gaussian apodization profile is modelled using such form of modulation parameter variation:

$$\overline{\delta n}_{eff}(z) = \overline{\delta n}_{eff}\exp\left(-\frac{4\ln 2 z^2}{\Delta z_{FWHM}{}^2}\right), \tag{A.2.16}$$

where Δz_{FWHM} is the full-width at half maximum of the grating profile. The raised-cosine apodization profile requires to divide $\overline{\delta n}_{eff}(z)$ function into 3 parts:

$$\overline{\delta n}_{eff}(z) = \begin{cases} \overline{\delta n}_{eff}, |z| \le \frac{1-\beta}{T} \\ \frac{\overline{\delta n}_{eff}}{2}\left[1+\cos\left(\frac{\pi T}{\beta}\left[|z|-\frac{1-\beta}{2T}\right]\right)\right], \frac{1-\beta}{2T} < |z| < \frac{1+\beta}{2T}, \\ 0, |z| \ge \frac{1+\beta}{2T} \end{cases} \quad \text{(A.2.17)}$$

where $T = \frac{1}{\Delta z_{FWHM}}$ and β is the roll-off factor, which determines the steepness of the function. Function profiles from rectangular ($\beta = 0$) to pure raised cosine ($\beta = 1$) can be produced varying the roll-off parameter [206].

Chirped FBG is modelled including the phase term in the self-coupling coefficient $\hat{\sigma}$ (A.2.8). The phase term for the linear chirp can be modified and written such as:

$$\frac{1}{2}\frac{d\phi}{dz} = -\frac{4\pi n_{eff} z}{\lambda_D^2} C. \quad \text{(A.2.18)}$$

The chirp parameter C is expressed in units of nm/cm and shows the rate of change of the design wavelength λ_D. In the piecewise-uniform approach the design wavelength is changes linearly from piece to piece of the grating according to the chirp parameter:

$$\lambda_D = \lambda_B + Cz. \quad \text{(A.2.19)}$$

The last step in modelling the non-uniform grating is to define the 2x2 matrix for each uniform section. Multiplying the consecutive matrixes, a single 2x2 matrix is obtained which describes the whole grating. The grating is divided into M sections, R_i and S_i are the field amplitudes of the section i. The calculation is started at $R_0 = R\left(\frac{L}{2}\right) = 1$, $S_0 = S\left(\frac{L}{2}\right) = 0$ and ended at $R\left(-\frac{L}{2}\right) = R_M$, $S\left(-\frac{L}{2}\right) = S_M$. The propagation through each section is described by a matrix $\boldsymbol{F_i}$ and the output parameters are obtained from:

$$\begin{bmatrix} R_M \\ S_M \end{bmatrix} = \boldsymbol{F}\begin{bmatrix} R_0 \\ S_0 \end{bmatrix}, \quad \text{(A.2.20)}$$

$$\boldsymbol{F} = \boldsymbol{F_M F_{M-1}} \cdots \boldsymbol{F_i} \cdots \boldsymbol{F_1}. \quad \text{(A.2.21)}$$

The propagation matrix $\boldsymbol{F_i}$ for length Δz uniform section of FBG as shown in [202] is:

$$\boldsymbol{F_i} = \begin{bmatrix} \cosh(\gamma\Delta z) - i\frac{\widehat{\sigma}}{\gamma}\sinh(\gamma\Delta z) & -i\frac{\kappa}{\gamma}\sinh(\gamma\Delta z) \\ i\frac{\kappa}{\gamma}\sinh(\gamma\Delta z) & \cosh(\gamma\Delta z) + i\frac{\widehat{\sigma}}{\gamma}\sinh(\gamma\Delta z) \end{bmatrix}, \quad \text{(A.2.22)}$$

$$\gamma = \sqrt{\kappa^2 - \widehat{\sigma}^2}. \quad \text{(A.2.23)}$$

The sufficient number of sections is chosen increasing the M value until the output results remain quantitatively constant. It is time-efficient to calculate the final matrix for each wavelength in the range of interest separately and then obtain the complex reflection amplitude from the certain matrix elements:

$$\rho(\lambda) = \frac{\boldsymbol{F}(\lambda)(2,1)}{\boldsymbol{F}(\lambda)(1,1)}. \quad \text{(A.2.24)}$$

The array of output values is used in the modelling program of the passively mode-locked oscillator multiplying with the pulse envelope $A(\omega)$ in the frequency domain. In such way, both wavelength-dependent reflectivity and grating dispersion are taken into account [201]. The group delay distribution of FBG can be extracted from the complex $\rho(\lambda)$ separating the phase part and calculating the first derivative:

$$GD(\omega) = \frac{d}{d\omega}\tan^{-1}\left(\frac{Im(\rho)}{Re(\rho)}\right). \quad \text{(A.2.25)}$$

The derivative of group delay leads to the group delay dispersion (GDD) of the grating.

The main features of uniform FBGs are discussed comparing two types of the gratings. Gratings with small modulation parameter ($\overline{\delta n}_{eff} \ll \frac{\lambda_B}{L}$) are called the weak gratings [202]. The bandwidth of such grating defined as a wavelength region between the first zeros on the either side of the maximum reflectivity is inversely proportional to the grating length L. Light does not propagate the full length of the grating in strong gratings ($\overline{\delta n}_{eff} \gg \frac{\lambda_B}{L}$), thus the bandwidth is not length-limited and is directly proportional to index change $\overline{\delta n}_{eff}$. Two 3 mm long gratings are chosen as an example (Fig. A.2.4). The design wavelength of both gratings is 1064 nm. Both gratings have a symmetrical reflectivity profile

about the Bragg wavelength and a damped sinusoidal modulation outside the band region.

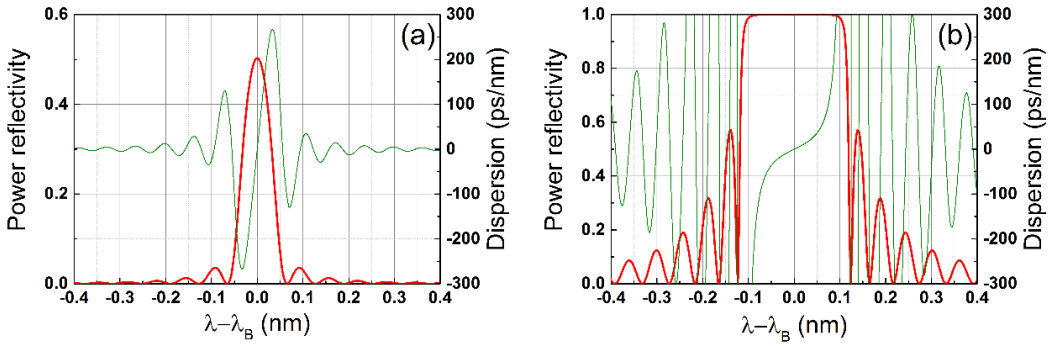

Fig. A.2.4 Comparison of (a) weaker and (b) stronger fiber Bragg grating. Red curves show the power reflectivity distribution. Dispersion parameter versus the wavelength which is recalculated as a difference from Bragg wavelength is plotted in green.

First grating (Fig. A.2.4(a)) is weaker ($\overline{\delta n}_{eff}$=1·10^{-4}) and due to the relatively small index modulation and length (A.2.15) exhibits low reflectivity at the Bragg condition wavelength. For a stronger grating ($\overline{\delta n}_{eff}$=6·10^{-4}) the maximum reflectivity is almost equal to 1, the reflection bandwidth is apparently broader and has a flat-top distribution. For both gratings, the dispersion is equal to 0 at λ_B at which it also changes the sign. The significant values of dispersion are reached approaching the edges of the grating bandwidth. The dispersion function recedes to zero in a damped sine wave function outside the bandwidth region.

Adding chirp to a grating period enables to alter the dispersion profile at the bandwidth region. This feature is widely applicable and used for dispersion compensation [207–211], pulse shaping and stretching in fiber lasers [176,212] and controlling of the mode-locking conditions in fiber oscillators [184,213,214]. In order to demonstrate the effects of FBG chirping a 3 mm long grating designed at 1064 nm wavelength was modelled (Fig. A.2.5). The modulation parameter $\overline{\delta n}_{eff}$ was equal to 8·10^{-4} and 3 nm/cm chirp rate was chosen. Chirping caused a significant broadening of the bandwidth region (Fig. A.2.5(a)) with a different structure of reflectivity comparing with a uniform FBG (Fig. A.2.4). The spectral response function had an oscillatory structure inside the band region and showed no damped sinusoidal modulations outside the region.

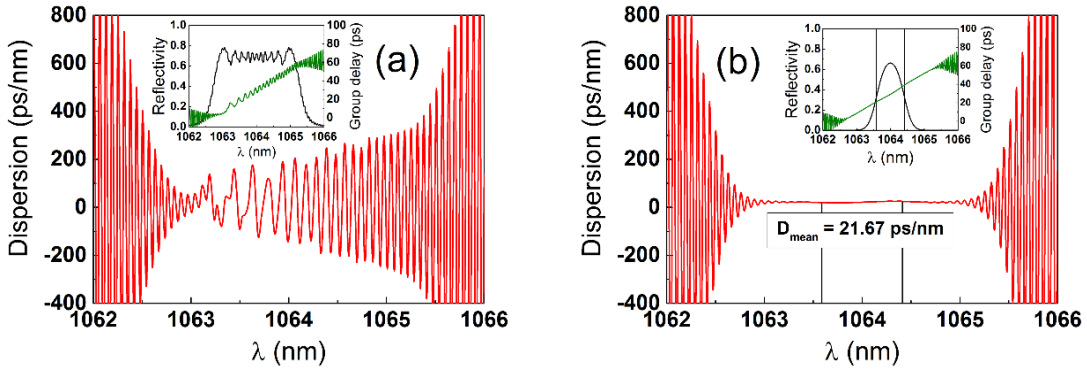

Fig. A.2.5 Theoretical demonstration of chirping and apodization effects on FBG: (a) chirped unapodized grating with an oscillatory-structured reflectivity distribution and dispersion; (b) apodized ($\boldsymbol{\Delta z_{FWHM} = 1}$) grating with the same parameters as the previous one exhibiting narrowed but smooth reflection spectrum and almost constant dispersion at the FWHM of the bandwidth region.

Both group delay and dispersion curves exhibited a noisy modulated structure which could not be applied for practical implementations. Grating apodization is used to deal with this issue. The effects of Gaussian apodization (Fig. A.2.2(c)) with a zero dc index change ($\sigma = 0$) were modelled. Although apodization caused to crucially narrow the reflection bandwidth, smooth reflection spectrum and practically constant dispersion value were achieved. The modelled grating had the dispersion coefficient of 21.67 ps/nm at the FWHM of the bandwidth region which corresponded to a delay of ~18 ps between the side spectral components. To sum up, the controlled interplay between chirping and apodization techniques is used to design FBGs with custom dispersion parameters for practical applications.

Point amplifier

Amplification in Yb^{3+} doped active fiber was modelled using a simplified approach approximating the gain medium by a point amplifier (Fig. A.2.1). The further described method serves for a quicker convergence, requiring less calculation iterations nevertheless achieving both quantitatively and qualitatively correct results. This approach was used only in the model of a passively mode-locked oscillator. The extended model which includes gain saturation and excited state population dynamics is discussed in Chapter A.3.

The effects of ultrashort pulse propagation in fiber including SPM and fiber dispersion are neglected during the amplification calculation stage. However, extra length is added to the surrounding passive fibers according to the length of the active fiber. The amplification of the pulse oscillating in the resonator is calculated in spectral domain multiplying the pulse envelope $A(\omega)$ by the total gain function:

$$G(\omega) = \exp\left(\frac{\Gamma_s}{2}(\sigma_e(\omega)N_2 - \sigma_a(\omega)N_1)L_G\right), \quad \text{(A.2.26)}$$

where σ_e and σ_a are Yb^{3+} emission and absorption cross-sections respectively, N_2 and N_1 – ion concentrations in the excited and ground states, L_G is the effective amplifier length, Γ_s is mode overlap factor.

The total ion concentration $N_t = N_1 + N_2$ is retrieved from a small-signal absorption α_s, pump wavelength cross-section $\sigma_a(\lambda_p)$ and overlap factor Γ_p in the active fiber. Small-signal absorption expressed in dB/m is specified by the manufacturer of the active fiber or measured experimentally. The following differential equation represents the pump propagation along the fiber excluding the losses when electron population is fully at the ground state [215]:

$$\frac{dP_p}{dz} = -N_t\Gamma_p\sigma_a(\lambda_p)P_p. \quad \text{(A.2.27)}$$

This is a first order linear differential equation which gives a solution:

$$P_p(z) = P_p(0)\exp(-N_t\Gamma_p\sigma_a(\lambda_p)z). \quad \text{(A.2.28)}$$

The small-signal absorption is defined as [216]:

$$\alpha_s = 10\log\left(\frac{P_p(z)}{P_p(0)}\right). \quad \text{(A.2.29)}$$

This relation used in (A.2.28) for a pump absorption per meter gives:

$$N_t = -\frac{\ln(10^{\alpha_s/10})}{\Gamma_p\sigma_a(\lambda_p)}. \quad \text{(A.2.30)}$$

The absorption and emission cross-sections of Yb^{3+} in a germanosilicate glass could be obtained from a spectroscopic measurements in fiber [215] and fitted using a series of Gaussian functions [217] in the form:

$$\sigma_j = \sum_m A_{j,m} \exp\left(-\left[\frac{\lambda - \lambda_{j,m}}{w_{j,m}}\right]^2\right). \qquad \text{(A.2.31)}$$

The coefficients for (A.2.31) are listed in Table A.2.1:

j	$A_{j,m}$ (10^{-27} m^2)	$\lambda_{j,m}$ (nm)	$w_{j,m}$ (nm)
a	180	950	70
a	360	895	24
a	510	918	22
a	160	971	12
a, e	2325	975	4
e	160	978	12
e	340	1025	20
e	175	1050	60
e	150	1030	90

Table A.2.1 Coefficients for Yb^{3+} emission and absorption cross-sections.

The resulting cross-sections are pictured in Fig. A.2.6. The importance of using wavelength-dependent cross-sections arises when oscillator modelling is performed with FBG which bandwidth is much broader than the soliton pulse spectral width. This implementation helps to determine the correct central wavelength and calculate closer to experimental pulse spectrum.

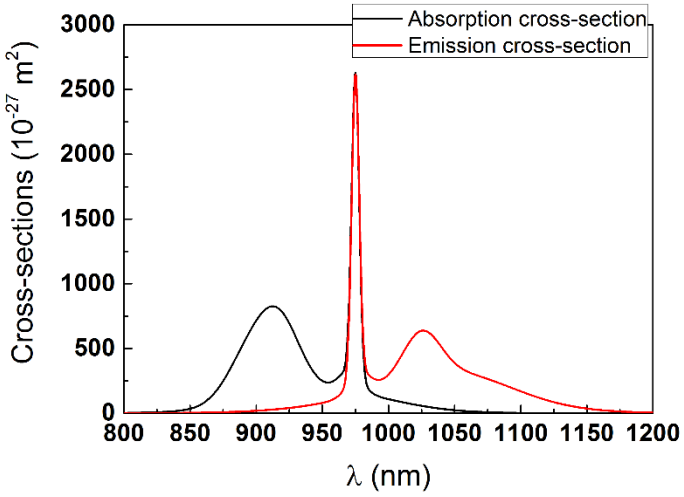

Fig. A.2.6 Absorption and emission cross-sections of Yb^{3+} in germanosilicate glass [215] fitted with series of Gaussian functions [217].

The relaxation of populations N_1 and N_2 are calculated according to the formula [201]:

$$N_2 = \frac{N_t}{2 + \overline{E}_p / E_{sat}}, \tag{A.2.32}$$

where $\overline{E}_p$ is the average of pulse energy at entry and exit points of the amplifier in the previous iteration, E_{sat} is model parameter controlling the resulting steady-state output pulse energy. This method to calculate the relaxation is suitable for quick calculations of pulse shape and double-pulse threshold determination. Regardless the initial pulse form, the model converges to the steady-state in a few hundreds of iterations.

SESAM

Modelling the response of a SESAM at one end of the resonator cavity requires a simplified mathematical description of the general theory of saturable absorbers [218,219]. The absorber is defined as a two-level or a fast three-level [219] system. The rate equation for this system describes the change of population in time due to the decay of electrons from conduction to valence band and the excitation of electrons caused by the absorption of light [201,218–220]:

$$\frac{dN_1}{dt} = -\frac{dN_2}{dt} = \frac{N_2}{\tau_A} - \frac{\sigma_a |A(t)|^2}{\hbar \omega_0 A_{eff}} N_1, \tag{A.2.33}$$

where N_1 and N_2 are the concentrations per area of lower and upper levels of the saturable absorber, τ_A is the relaxation time of the absorbing medium, σ_a – absorption cross-section, A_{eff} – effective area of the laser beam spot on the SESAM and $|A(t)|^2$ corresponds to the instantaneous pulse power. Cross-section of the absorber can be calculated from the saturation fluence and the total concentration of the absorbers $N_0 = N_1 + N_2$ – from the saturable absorption q_0:

$$\sigma_a = \frac{\hbar \omega_0}{F_s}. \tag{A.2.34}$$

$$N_0 = \frac{g_0}{\sigma_a}. \tag{A.2.35}$$

Saturation fluence F_s multiplied by the effective area of the focus A_{eff} is defined as a saturation energy E_{sat}. Knowing this and using (A.2.34), (A.2.35), equation

(A.2.33) is usually rewritten for time-dependent saturable absorption $q(t)$ of the medium which is equal to $N_1(t)\sigma_a$ [201,220].:

$$\frac{dq}{dt} = -\frac{q - q_0}{\tau_A} - \frac{|A(t)|^2}{E_{sat}} q. \tag{A.2.36}$$

This differential equation can be solved numerically, however, for two different cases analytic solutions exist. These cases will be discussed briefly.

In case of a fast absorber, when the incident pulse is much longer than the relaxation time τ_A, it is assumed that SESAM instantaneously absorbs the pulse power and $\frac{dq}{dt} = 0$. The solution of (A.2.36) in this case is:

$$q(t) = \frac{q_0}{1 + \frac{P}{P_{sat}}}, \tag{A.2.37}$$

where P_{sat} is the saturation power equals to E_{sat}/τ_A.

When absorber relaxation time is much longer than the pulse duration, it is called a slow saturable absorber case and (A.2.36) becomes:

$$\frac{dq}{dt} = -\frac{|A(t)|^2}{E_{sat}} q. \tag{A.2.38}$$

This equation is a linear ordinary differential equation, which solution is:

$$q(t) = q_0 \exp\left(-\frac{1}{E_{sat}} \int_{-\infty}^{t} P(t)dt \right). \tag{A.2.39}$$

Finally, dividing the pulse shape into small sections of a constant power, (A.2.36) can be solved analytically for each of the section. This gives the solution for a numerical recursive calculation:

$$q(t + t_0) = \left[q(t_0) - \frac{q_0 E_{sat}}{E_{sat} + P\tau_A} \right] \exp\left[-\left(\frac{1}{\tau_A} + \frac{P}{E_{sat}} \right) t \right] + \frac{q_0 E_{sat}}{E_{sat} + P\tau_A}. \tag{A.2.40}$$

The calculated time-dependent saturable absorption is used to determine the SESAM response to the coinciding pulse amplitude in the form of reduced reflectivity due to the unsaturable A_0 and saturable losses:

$$A(t) = A(t)\sqrt{1 - A_0 - q(t)}. \tag{A.2.41}$$

In the same manner, the response of passive components inside the resonator cavity such as a beam splitter is calculated.

Modelling parameters

The table below lists the main parameters of the numerical model which was used to calculate the output pulse characteristics of the all-in-fiber oscillator presented in Chapter 2.2. All the values were chosen according to the experimental conditions.

Component	*Parameter*	*Value*	*Source*
CFBG	L	2.25 mm	TeraXion specification
	$\overline{\delta n_{eff}}$	$2.145 \cdot 10^{-3}$	Calculated
	C	35 nm/cm	Calculated
	Δz_{FWHM}	0.33 mm, Gaussian	Calculated
	λ_D	1064.135 nm	Calculated
Active fiber	N_t	$2.5 \cdot 10^{25}$ m^{-3}	Calculated from Nufern specification
	L_G	0.7 m	Measured
	E_{sat}	32.5 pJ	Calculated
SESAM	A_0	0.13	Batop specification
	q_0	0.17	Batop specification
	F_s	0.42 J/m^2	Batop specification
	τ_A	1 ps	Batop specification
Passive fiber	β_2	0.02 ps^2	Calculated [156]
	β_3	$4.4 \cdot 10^{-5}$ ps^3	Calculated [156]
	γ	0.0033 (W·m)$^{-1}$	Calculated [156]
	L	3.26 m	Measured

Table A.2.2 Main parameters for the modelling of fiber oscillator which was described in Chapter 2.2.

A.3 Ultrashort pulse amplification dynamics

The point amplifier approach described in the previous section is fast but inaccurate to model the effects of ultrashort pulse amplification in Yb^{3+} doped active fibers. A combined numerical model of rate equations and NLSE was chosen for the extended analysis. This model allows calculating the excited level population dynamics, gain saturation, power loss due to the amplification of spontaneous emission and the interplay between dispersion and nonlinearity during the propagation along the active fiber. Numerical calculations of high energy Yb^{3+} doped large-mode-area (LMA) fiber amplifiers was performed using the developed model which is based on the theory presented in references [215,221–224].

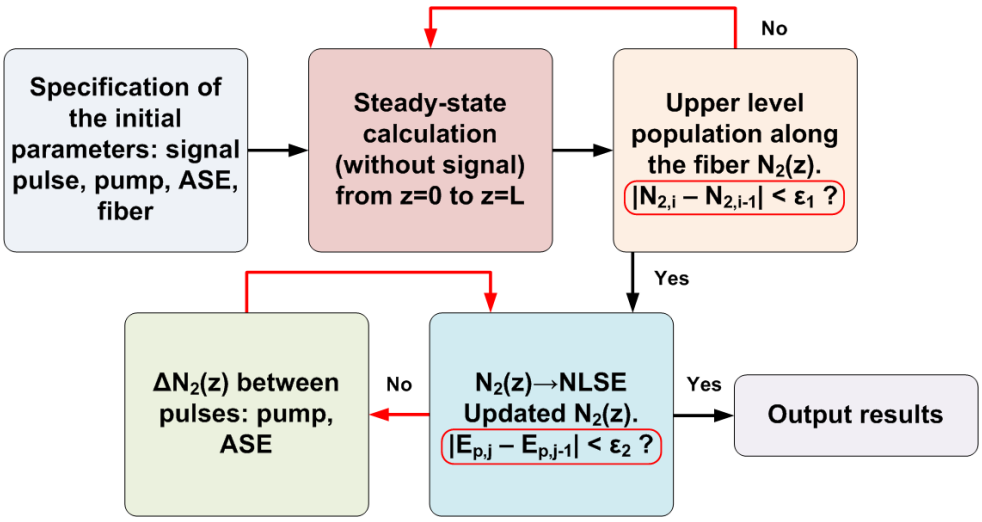

Fig. A.3.1 Principle scheme of the pulsed-mode fiber amplifier model. After specification of the initial parameters, a steady-state solution without signal input is calculated using the iterative algorithm. The upper-level population along the fiber $\boldsymbol{N_2(z)}$ is used in NLSE modelling. $\boldsymbol{N_2(z)}$ is recalculated between the pulses until the pulse energy becomes steady.

The principle modelling scheme is presented in Fig. A.3.1. Initially, parameters regarding the signal pulse, pump, amplified spontaneous emission (ASE) as well as the computation settings are specified. Next, the steady-state solution without signal input is calculated using an iterative algorithm of rate equations modelling. The calculated upper-level population $N_2(z)$ along the active fiber is sent to the extended NLSE model in which amplification of the signal pulse including the gain saturation effect is calculated at each step h. The effects of dispersion and nonlinearity are also taken into account. The upper-level population is updated after the amplification. Then population dynamics are modelled between the two adjacent pulses at the time interval according to the repetition rate of the laser. The procedure is repeated until the energy of the consecutive pulses becomes steady. Equations modelled and numerical methods used in each step of this model will be presented in the next subsections.

Steady-state calculation

Spatially and time-dependent rate and propagation equations can be established stating that the Yb^{3+} doped gain medium is a homogeneously broadened two effective energy level system with electron population densities N_1 and N_2 for ground and excited state levels respectively. The propagation of power and

change of energy level populations along the active fiber are described using the equations below [222]:

$$\frac{\partial N_2}{\partial t} = \frac{\Gamma_p}{hcA_d}\lambda^p[\sigma_a(\lambda^p)N_1 - \sigma_e(\lambda^p)N_2]P_p + \frac{\Gamma_s}{hcA_d}\lambda^s[\sigma_a(\lambda^s)N_1 - \sigma_e(\lambda^s)N_2]P_s + \frac{\Gamma_A}{hcA_d}\sum_k \lambda_k^A\left[\sigma_a\left(\lambda_k^A\right)N_1 - \sigma_e\left(\lambda_k^A\right)N_2\right]P_A^{\pm}\left(\lambda_k^A\right) - \frac{N_2}{\tau}, \quad \text{(A.3.1)}$$

$$N_1 = N_T - N_2, \quad \text{(A.3.2)}$$

$$\frac{\partial P_p}{\partial z} + \frac{1}{v_p}\frac{\partial P_p}{\partial t} = \Gamma_p[\sigma_e(\lambda^p)N_2 - \sigma_a(\lambda^p)N_1]P_p - \eta_p P_p, \quad \text{(A.3.3)}$$

$$\frac{\partial P_s}{\partial z} + \frac{1}{v_s}\frac{\partial P_s}{\partial t} = \Gamma_s[\sigma_e(\lambda^s)N_2 - \sigma_a(\lambda^s)N_1]P_s - \eta_s P_s, \quad \text{(A.3.4)}$$

$$\pm\frac{\partial P_A^{\pm}\left(\lambda_k^A\right)}{\partial z} + \frac{1}{v_A\left(\lambda_k^A\right)}\frac{\partial P_A^{\pm}\left(\lambda_k^A\right)}{\partial t} = \Gamma_A\left[\sigma_e\left(\lambda_k^A\right)N_2 - \sigma_a\left(\lambda_k^A\right)N_1\right]P_A^{\pm}\left(\lambda_k^A\right) - \eta_A P_A^{\pm}\left(\lambda_k^A\right) + 2\Gamma_A\sigma_e\left(\lambda_k^A\right)N_2\frac{hc^2\Delta\lambda}{\left(\lambda_k^A\right)^3}. \quad \text{(A.3.5)}$$

Throughout the equations (A.3.1)-(A.3.5) P_s, P_p are signal and pump powers respectively and $P_A^{\pm}$ is the power of ASE ($\pm$ corresponds to forward and backward propagation). Γ_s(Γ_p, Γ_A) is the overlap factor between the signal (pump, ASE) radiation and the doped area. This area is given by the A_d value. v_s, v_p and v_A are the phase velocities of the signal, pump and ASE respectively. Fiber losses are defined by η_s, η_p and η_A, τ is the upper level lifetime. The third term on the right side of the equation (A.3.5) accounts for a continuously generated ASE [221,225]. It is considered that pump radiation is single-wavelength and forward-propagating. The impact of ASE is calculated by defining the certain number of equal width wavelength channels [226]. Equation (A.3.5) is solved separately for each channel.

Time derivatives in equations (A.3.1)-(A.3.5) are set to zero for a steady-state calculation, which means that N_2 can be expressed from (A.3.1) and (A.3.2):

$$N_2 = N_T\frac{X}{Y}, \quad \text{(A.3.6)}$$

$$X = \frac{\Gamma_p}{hcA_d}\lambda^p\sigma_a(\lambda^p)P_p + \frac{\Gamma_s}{hcA_d}\lambda^s\sigma_a(\lambda^s)P_s + \frac{\Gamma_A}{hcA_d}\sum_k \lambda_k^A\sigma_a(\lambda_k^A)P_A^{\pm}(\lambda_k^A), \tag{A.3.7}$$

$$Y = \frac{\Gamma_p}{hcA_d}\lambda^p[\sigma_a(\lambda^p) + \sigma_e(\lambda^p)]P_p + \frac{\Gamma_s}{hcA_d}\lambda^s[\sigma_a(\lambda^s) + \sigma_e(\lambda^s)]P_s + \frac{\Gamma_A}{hcA_d}\sum_k \lambda_k^A[\sigma_a(\lambda_k^A) + \sigma_e(\lambda_k^A)]P_A^{\pm}(\lambda_k^A) + \frac{1}{\tau}. \tag{A.3.8}$$

In order to obtain steady-state conditions before the first signal pulse arrives, P_s is set to zero. Equations regarding the propagation of power (A.3.3)-(A.3.5) are solved using the 4th order Runge-Kutta method [200]. The main problem of the steady-state calculation is that the rate equations require population densities $N_1(z)$ and $N_2(z)$ which are initially unknown. Thus, the iterative calculation method is implemented. Equations (A.3.3)-(A.3.5) are solved repeatedly from $z = 0$ to the end of the fiber, determining the upper level population $N_2(z)$ at the end of each iteration until it becomes steady according to the initially defined parameter of tolerance. The resulting $N_2(z)$ is later used in NLSE-based calculation of ultrashort pulse amplification.

Pulse amplification with gain saturation

In order to propagate the pulse along the active fiber, the NLSE is used (A.1.1) with a z-dependent gain coefficient $G(\omega, z)$ calculated from the equation (A.2.26). Population densities $N_1(z)$ and $N_2(z)$ are taken from the previously presented steady-state modelling. The propagation equation is solved using a symmetrized split-step Fourier algorithm described in Chapter A.1. Furthermore, the calculation in one small step h along the fiber is extended including the effect of gain saturation on the ultrashort pulse envelope. The upper level population density N_2 is altered and distributed across the pulse in time domain according to the relation:

$$N_2^i(t) = N_2^i - \frac{1}{\hbar\omega_0 A_d h}\int_{-\infty}^{t}\left(\left|A_1^{i-1}(t)\right|^2 - \left|A_0^{i-1}(t)\right|^2\right)dt, \tag{A.3.9}$$

where $\left|A_0^{i-1}(t)\right|^2$ and $\left|A_1^{i-1}(t)\right|^2$ are the pulse intensity functions in the previous step i before and after the amplification respectively. This modification of N_2 implies that the leading part of the pulse will experience maximum gain. Moreover, the upper level population will be depleted at the trailing part of the pulse in a regime of saturated amplification.

Pulse amplification is performed in Fourier domain expanding the exponential from equation (A.2.26) in Taylor series to the 1st order:

$$\widetilde{A}_1(\omega) = \widetilde{A}_0(\omega) + \left(F_T[A_0(t)N_2(t)](\sigma_e(\omega) + \sigma_a(\omega)) - N_T\widetilde{A}_0(\omega)\sigma_a(\omega)\right)\frac{h}{2}. \qquad \text{(A.3.10)}$$

The time-dependent N_2 is included calculating the convolution with the pulse envelope in spectral domain and applying the convolution theorem [199].

The change in upper-level population ΔN_2 is determined after each step h along the z axis by comparing the pulse energies before and after amplification:

$$\Delta N_2(z) = \frac{1}{\hbar\omega A_d h}\int_{-\infty}^{\infty}(|A_1(t)|^2 - |A_0(t)|^2)dt. \qquad \text{(A.3.11)}$$

Changes in pump depletion distribution $P_p(z)$ and ASE power distribution $P_A^{\pm}\left(\lambda_k^A, z\right)$ during the pulse amplification are neglected due to the much longer than pulse duration upper level lifetime.

Population dynamics between the pulses

At the time intervals between the two signal pulses, the population of the excited electrons changes depending on continuous pumping and ASE. In order to simulate the dynamics of states, it is necessary to solve the rate equations again. Upper-level population $N_2(z)$, updated after the pulse amplification step, $P_p(z)$ and $P_A^{\pm}\left(\lambda_k^A, z\right)$, both obtained from the steady-state calculation are used as the initial conditions. The temporal interval is divided into small time steps Δt. Equation (A.3.1) is calculated analytically for each time step. Pump and ASE power distributions are updated simultaneously.

The newly calculated upper-level population $N_2(z)$ is used again in NLSE-based pulse amplification modelling. Recorded $P_p(z)$ and $P_A^{\pm}\left(\lambda_k^A, z\right)$ distributions are set as initial for the next step of population dynamics between

the pulses calculation. The procedure is repeated until the amplified pulse energy does not change from pulse to pulse according to the predefined tolerance. The resulting steady pulse is declared as the output of the ultrashort pulse fiber amplifier.

A.4 Ultrashort pulse stretching and compression

Controlled pulse stretching and compression techniques allowing not only to achieve large stretching ratios but also to compress pulses down to transform-limited durations is crucial both in CPA and FCPA systems. Possibilities to change the temporal shape in optical fiber and CFBG were discussed in the previous chapters. In this chapter, conventional free-space methods which were realised in the experimental part of this work are presented.

The ultrashort pulse is treated as a packet of quasi-monochromatic waves which are coherently added together [199,227]. The following equation relates the incident to the dispersive component electric field $\widetilde{E}_{in}(\omega)$ to the output field [227]:

$$\widetilde{E}_{out}(\omega) = \widetilde{E}_{in}(\omega)\exp\left(-i\phi_d\right), \tag{A.4.1}$$

where $\phi_d(\omega)$ denotes the spectral phase transfer function. This function will be given for the different cases described in the following subsections.

Dispersion in transparent glass

Pulse broadening in a bulk transparent glass is caused by the chromatic dispersion and calculated in the same way as for the optical fiber. An ultrashort pulse propagating a distance L in a transparent medium with the index of refraction $n(\omega)$ acquires the spectral phase [227]:

$$\phi_m(\omega) = \frac{\omega}{c} n(\omega) L. \tag{A.4.2}$$

The second and the third derivative of ϕ_m define GVD and TOD coefficients of the glass respectively, which expressed in the units of wavelength are equal to [199,227]:

$$GVD = \frac{\lambda^3 L}{2\pi c^2}\frac{d^2 n}{d\lambda^2}, \tag{A.4.3}$$

$$TOD = -\frac{\lambda^4 L}{4\pi^2 c^3}\left(3\frac{d^2 n}{d\lambda^2} + \lambda\frac{d^3 n}{d\lambda^3}\right). \tag{A.4.4}$$

The comparison of GVD and TOD coefficients with respect to the wavelength for fused silica, SF10 and SF57 glasses are shown in Fig. A.4.1. The latter two were used in the experimentally realised OPCPA system described in Chapter 4, in order to stretch the supercontinuum pulses in time. Pulse broadening caused by the propagation through 10 mm of different glasses are summarised in Table A.4.1. Initial Gaussian shape pulses at 800 nm wavelength were chosen for the modelling. The effect of uncompensated TOD becomes significant for few-cycle pulses. Assuming perfect cancellation of GVD, 10 fs pulse propagation through 10 mm of SF57 glass induces the pulse broadening to 16 fs with a characteristically distorted trailing edge.

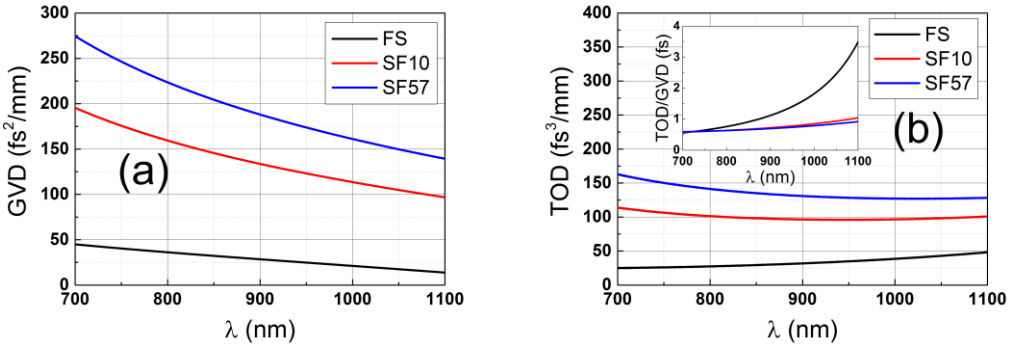

Fig. A.4.1 Dispersion characteristics of different transparent glasses: (a) GVD [fs^2/mm]; (b) TOD [fs^3/mm] with ratio between TOD and GVD pictured in the inset.

	FS (10 mm)	*SF10 (10 mm)*	*SF57 (10 mm)*
100 fs	101 fs	109 fs	118 fs
30 fs	45 fs	150 fs	209 fs
10 fs	100 fs	441 fs	618 fs

Table A.4.1 Dispersive broadening of Gaussian pulses at 800 nm wavelength propagated through 10 mm of different glasses. Pulse durations are given at FWHM.

Dispersion of a prism sequence

The interplay between material and angular dispersion determines the total dispersion of prism stretcher-compressor. In this section, two-prism sequence in a double-pass configuration is presented (Fig. A.4.2).

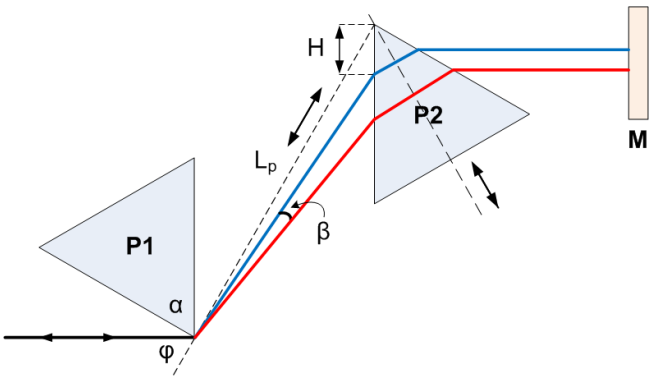

Fig. A.4.2 Principle layout of a prism pair in a double-pass configuration. The abbreviations stand for: P1, P2 – prisms with apex angles $\boldsymbol{\alpha}$, M – mirror, $\boldsymbol{\varphi}$ – angle of incidence to the first prism, L_p – prism separation distance, H – prism insertion length and $\boldsymbol{\beta}$ is the angle of rays with respect to the reference ray.

Spectral phase transfer function for devices exhibiting angular dispersion can be written in a form:

$$\phi(\omega) = \frac{\omega}{c} P_{op}(\omega), \tag{A.4.5}$$

where P_{op} is the optical path length from an input to an output plane of the dispersive system expressed as:

$$P_{op}(\omega) = L_o \cos[\beta(\omega)]. \tag{A.4.6}$$

Distance L_o is the optical path of the reference ray ω_0 and β is the angle of rays with frequency ω with respect to the ray ω_0. It is shown in [228,229] that the transfer function of a prism pair in a double-pass configuration is:

$$\phi_p(\omega) = \frac{2L_p\omega}{c} \cos[\theta_{max} - \theta(\omega)], \tag{A.4.7}$$

where θ_{max} is the maximum angle at which a ray can exit the first prism, in other words, this is the angle of the shortest wave. $\theta(\omega)$ is the frequency dependent prism exit angle, L_p is the distance between prism apices, which is multiplied by 2 due to the double-pass configuration. Exit angle $\theta(\omega)$ is found from the prism geometry using the law of refraction:

$$\theta(\omega) = \sin^{-1}\left(n(\omega)\sin\left(\alpha - \sin^{-1}\left(\frac{\sin\varphi}{n(\omega)}\right)\right)\right), \tag{A.4.8}$$

where α is the apex angle and φ is the angle of incidence to the surface of the first prism. GVD and TOD of the prism stretcher-compressor can be determined by calculating the second and the third derivatives of $\phi_p(\omega)$ respectively.

In the case of minimum deviation (beam entrance and exit angles to the first prism are equal) and with the apex angle chosen to satisfy Brewster's condition ($\alpha = \tan^{-1}(n_{glass}/n_{air})$), group velocity dispersion can be approximated [199,230]. This approximation leads to:

$$GVD = \frac{\lambda^3 L}{\pi c^2}\frac{d^2 n}{d\lambda^2} - \frac{4L_p\lambda^3}{\pi c^2}\left(\frac{dn}{d\lambda}\right)^2, \qquad \text{(A.4.9)}$$

where L is the mean path through the prism glass. Terms of this relation show two different types of contributions to the total prism pair dispersion. The first term originates from the propagation inside the prism medium and is referred to the material dispersion (A.4.3). The second term describes angular dispersion, which produces negative GVD. Fused silica (FS) and SF10 glass prism compressors were simulated and compared in Fig. A.4.3. The distance between prisms was set to 10 cm. Compressor with SF10 prisms exhibits much larger dispersion than the one with FS prisms, thus less distance is needed to compensate the same amount of material dispersion. However, the main disadvantage of using SF10 and other strongly dispersive glasses is the ratio between TOD and GVD (Fig. A.4.3(b), inset). This ratio can be few times and even more larger than the corresponding ratio of a bulk transparent glass. Therefore, due to the significant amount of residual TOD, it would be difficult to compensate the material dispersion for few-cycle (<10 fs) pulses and achieve close to a transform-limited pulse duration. For this reason, FS prism pair was used in the experimental scheme described in Chapter 2.2.

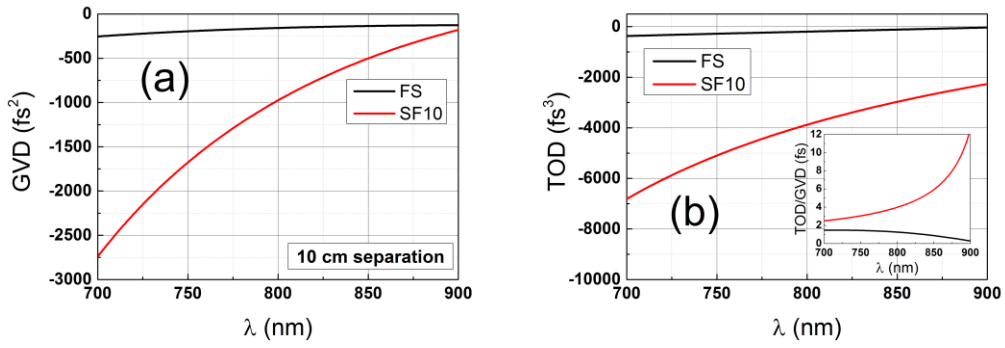

Fig. A.4.3 Dispersion characteristics of FS and SF10 glass prism double-pass compressors with 10 cm prism separation length: (a) GVD; (b) TOD and the ratio between TOD and GVD pictured in the inset.

The amount of total GVD and even its sign can be changed by translating one of the prisms along the axis of symmetry (Fig. A.4.2). Therefore, the value of positive GVD is altered due to the propagation through the glass material. The phase transfer function for a prism compressor with the insertion length H is derived in [231]:

$$\phi_p(\omega) = \frac{2L_p\omega}{c}\cos\left[\theta_{max} - \theta(\omega) + \sin^{-1}\left(\frac{H\cos(\theta_{max})}{L_p}\right)\right]. \qquad \text{(A.4.10)}$$

The effects of prism insertion are shown in Fig. A.4.4. SF10 glass prisms separated by a distance of 10 cm were chosen for the simulation. The insertion length H varied from zero to 5 mm.

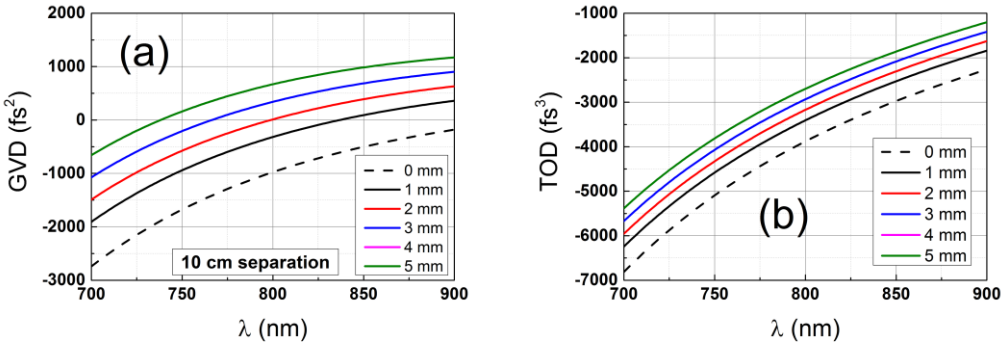

Fig. A.4.4 Dispersion characteristics of SF10 prism compressor at different insertion lengths of the second prism: (a) GVD; (b) TOD.

It is observed from the picture, that GVD coefficient changed its sign at 800 nm from negative to positive, while TOD decreased with a growing amount of H but remained negative. Prism translation along the symmetry axis is the most convenient way to fine tune the dispersion of the compressor, as it does not misalign the beam.

Diffraction grating compressor

Dispersion characteristics of a conventional diffraction grating compressor are exclusively determined by the angular dispersion. A pair of diffraction gratings in a double-pass configuration pictured in Fig. A.4.5 is analysed in this subsection. After the incidence to the first grating, the beam is diffracted at different angles θ according to the wavelength. The second grating, which is

parallel to the first, collimates the beam in the diffraction plane. A flat mirror is used to recover the original beam by inverting and reflecting it back.

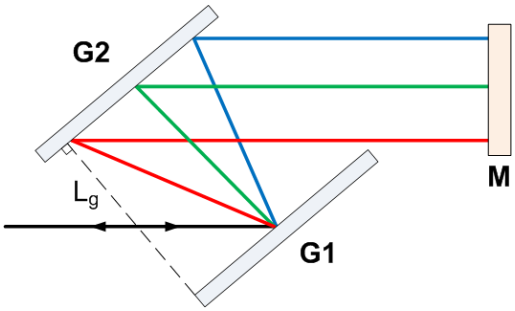

Fig. A.4.5 Principle scheme of the diffraction grating compressor. Beam incident to the grating G1 is diffracted in one plane at different angles according to the wavelength. The angularly dispersed beam is collimated by the grating G2 which is parallel to G1 and back-reflected by the mirror M.

According to the picture Fig. A.4.5, the red spectral components travel a longer optical path than the blue components. Thus, this configuration is suitable to compensate positive dispersion of a bulk transparent glass or an optical fiber.

Phase transfer function of the grating compressor is derived from the well-known grating equation (A.2.2) and is written in a form [107,228]:

$$\phi_g(\omega) = \frac{2L_g\omega}{c}\sqrt{\left[1-\left(\frac{2\pi c}{\omega d}-\sin\varphi\right)^2\right]}, \qquad \text{(A.4.11)}$$

where L_g is grating separation, d is groove spacing and φ is the angle of incidence to the first grating. Calculating the derivatives of this equation, GVD and TOD coefficients can be found. Analytical expressions of these coefficients according to the wavelength are given [199,227]:

$$GVD = -\frac{\lambda^3 L_g}{\pi c^2 d^2}\left[1-\left(\frac{\lambda}{d}-\sin\varphi\right)^2\right]^{-\frac{3}{2}}, \qquad \text{(A.4.12)}$$

$$TOD = -\frac{3\lambda}{2\pi c}\left[\frac{\cos^2\varphi+\frac{\lambda}{d}\sin\varphi}{1-\left(\frac{\lambda}{d}-\sin\varphi\right)^2}\right]GVD. \qquad \text{(A.4.13)}$$

Dispersion characteristics of two experimentally used compressors with different line density d^{-1} gratings are compared in Table A.4.2. The angle of incidence was chosen to satisfy the Littrow condition ($\varphi = \theta(\lambda_0)$) [227] at 1064 nm wavelength. This condition is usually applied for blazed diffraction

grating compressors. Blazed gratings have maximum efficiency at Littrow configuration. Moreover, at this angle, the beam astigmatism is minimized [227].

Line density	*Littrow angle*	*GVD*	*TOD*	*TOD/GVD*
1000 gr./mm	32.1 deg	-0.070 ps^2/cm	$2 \cdot 10^{-4}$ ps^3/cm	-3.03 fs
1600 gr./mm	58.3 deg	-0.755 ps^2/cm	$8 \cdot 10^{-3}$ ps^3/cm	-10.62 fs

Table A.4.2 Dispersion characteristics of 1000 grooves/mm and 1600 grooves/mm line density diffraction grating compressors.

Employing higher line density gratings in strongly chirped pulse compressors enables to compact the FCPA schemes efficiently. However, such gratings also exhibit a larger amount of positive TOD, which adds up with the fiber dispersion and causes to decrease the contrast of the output pulse. This is not an issue when specially designed CFBG with the opposite TOD sign is implemented as a stretcher in the FCPA design [212].

The Offner stretcher

A pair of lenses employed in the diffraction grating compressor improve the scheme in a way that the sign of GVD can be manipulated [102]. A principle layout of such configuration is pictured in Fig. A.4.6.

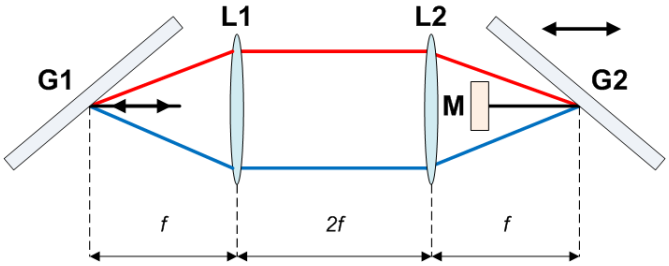

Fig. A.4.6 Principle layout of diffraction grating stretcher-compressor with a telescope in between the gratings. L1, L2 stand for lenses, *f* is the focal length.

The scheme shows a zero-dispersion configuration, when a telescope which images the beam spot on the first grating onto the second is used. This way, all the wavelengths travels the same optical path. The corresponding scheme is applied for pulse shaping or masking [227,232]. Moving one of the gratings out of the focal plane closer to the telescope lens results in a positive GVD, since the red components will travel shorter optical path. Alternatively, translating the

grating away from the focal plane will create negative GVD. If the paraxial approximation is used and lens material dispersion is neglected, a grating stretcher with a telescope configuration will produce dispersion equal and opposite to that of pulse compressor to all orders. This is valid when grating incident angles are identical and grating separation of the compressor is equal to $2f - x_1 - x_2$, where x_1 and x_2 are the distances of the stretcher gratings from the lenses [104]. Corresponding self-compensating stretcher-compressor unit was proposed and used in CPA systems [233–236]. However, dispersion of lens material causes significant temporal aberrations in systems where pulse durations are below 100 fs. Furthermore, chromatic and spherical aberrations add up to produce a spatially varying pulse spectrum and compressed pulse distortion. One of the simplest modifications of the described scheme is changing the lenses into concave mirrors [104]. A further improvement was proposed by G. Cheriaux et al. [106]. They proposed an implementation of all-reflective Offner triplet [105] in which all aberrations are canceled. This configuration is composed of two spherical concentric mirrors, whose ratio of curvature radius is two and of the opposite sign (Fig. A.4.7). The relation between grating separation L_g and the distance between the grating and the concave spherical mirror is [237]:

$$L_g = -2(R - S)\cos\theta, \tag{A.4.14}$$

where R is the radius of curvature of the concave mirror, S is the distance between the grating and the mirror and θ corresponds to the diffraction angle of the central wavelength.

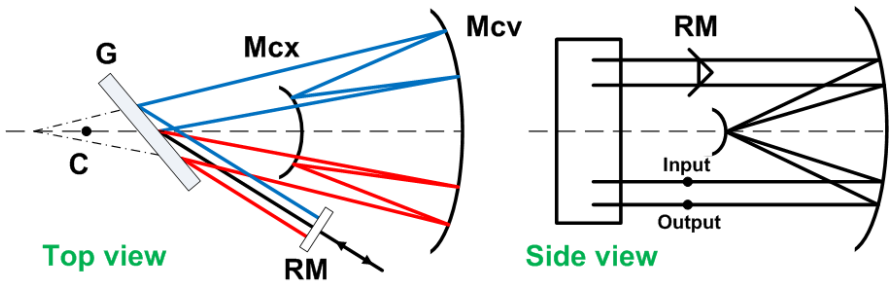

Fig. A.4.7 Principle scheme of a single-grating Offner-type pulse stretcher used in the experiments of this work. The letter C denotes the center of curvature of both convex Mcx and concave Mcv mirrors. G stands for the grating; RM is the roof mirror.

Perfect stigmatism is achieved only when the grating is at the common center of curvature (denoted by letter C in Fig. A.4.7). In a pictured single-grating layout, a diffraction grating is translated towards the concave spherical mirror out of the plane of the center of curvature. Nonetheless, it was demonstrated that the accumulated spherical aberration is weak enough not to affect the 30 fs duration pulses stretched to 300 ps and then recompressed [106]. The output pulse contrast can be limited by the surface roughness of the spherical mirrors. It was shown in [113], that for less than 15 fs duration pulses, $\lambda/10$ rms roughness can cause a significant degradation of pulse contrast.

Bibliography

[1] R. Berera, R. van Grondelle, and J. T. M. Kennis, "Ultrafast transient absorption spectroscopy: principles and application to photosynthetic systems," Photosynth. Res. **101**, 105–118 (2009). DOI: 10.1007/s11120-009-9454-y.

[2] Y.-Z. Ma, J. Stenger, J. Zimmermann, et al., "Ultrafast carrier dynamics in single-walled carbon nanotubes probed by femtosecond spectroscopy," J. Chem. Phys. **120**, 3368 (2004). DOI: 10.1063/1.1640339.

[3] T. C. Kippeny, M. J. Bowers, A. D. Dukes, et al., "Effects of surface passivation on the exciton dynamics of CdSe nanocrystals as observed by ultrafast fluorescence upconversion spectroscopy," J. Chem. Phys. **128**, 84713 (2008). DOI: 10.1063/1.2834692.

[4] N. Pontius, P. S. Bechthold, M. Neeb, and W. Eberhardt, "Ultrafast Hot-Electron Dynamics Observed in Pt_3^- Using Time-Resolved Photoelectron Spectroscopy," Phys. Rev. Lett. **84**, 1132–1135 (2000). DOI: 10.1103/PhysRevLett.84.1132.

[5] I. V. Hertel and W. Radloff, "Ultrafast dynamics in isolated molecules and molecular clusters," Reports Prog. Phys. **69**, 1897–2003 (2006). DOI: 10.1088/0034-4885/69/6/R06.

[6] T. Balciunas, A. Melninkaitis, G. Tamosauskas, and V. Sirutkaitis, "Time-resolved off-axis digital holography for characterization of ultrafast phenomena in water," Opt. Lett. **33**, 58 (2008). DOI: 10.1364/OL.33.000058.

[7] D. Pestov, M. Zhi, Z.-E. Sariyanni, et al., "Femtosecond CARS of methanol-water mixtures," J. Raman Spectrosc. **37**, 392–396 (2006). DOI: 10.1002/jrs.1482.

[8] P. F. Moulton, "Spectroscopic and laser characteristics of $Ti:Al_2O_3$," J. Opt. Soc. Am. B **3**, 125 (1986). DOI: 10.1364/JOSAB.3.000125.

[9] E. J. Mayer, J. Möbius, A. Euteneuer, W. W. Rühle, and R. Szipőcs, "Ultrabroadband chirped mirrors for femtosecond lasers," Opt. Lett. **22**,

528 (1997). DOI: 10.1364/OL.22.000528.

[10] P. G. Antal and R. Szipocs, "Tunable, low-repetition-rate, cost-efficient femtosecond Ti:sapphire laser for nonlinear microscopy," Appl. Phys. B Lasers Opt. **107**, 17–22 (2012). DOI: 10.1007/s00340-011-4830-7.

[11] S. Backus, C. G. Durfee, M. M. Murnane, and H. C. Kapteyn, "High power ultrafast lasers," Rev. Sci. Instrum. **69**, 1207–1223 (1998). DOI: 10.1063/1.1148795.

[12] G. Cerullo and S. De Silvestri, "Ultrafast optical parametric amplifiers," Rev. Sci. Instrum. **74**, 1 (2003). DOI: 10.1063/1.1523642.

[13] S. Witte and K. S. E. Eikema, "Ultrafast Optical Parametric Chirped-Pulse Amplification," IEEE J. Sel. Top. Quantum Electron. **18**, 296–307 (2011). DOI: 10.1109/JSTQE.2011.2118370.

[14] A. Dubietis, R. Butkus, and A. P. Piskarskas, "Trends in chirped pulse optical parametric amplification," IEEE J. Sel. Top. Quantum Electron. **12**, 163–172 (2006). DOI: 10.1109/JSTQE.2006.871962.

[15] K. Midorikawa, "High-Order Harmonic Generation and Attosecond Science," Jpn. J. Appl. Phys. **50**, 90001 (2011). DOI: 10.1143/JJAP.50.090001.

[16] T. Popmintchev, M.-C. Chen, D. Popmintchev, et al., "Bright Coherent Ultrahigh Harmonics in the keV X-ray Regime from Mid-Infrared Femtosecond Lasers," Science **336**, 1287–1291 (2012). DOI: 10.1126/science.1218497.

[17] N. Ishii, L. Turi, V. S. Yakovlev, et al., "Multimillijoule chirped parametric amplification of few-cycle pulses," Opt. Lett. **30**, 567 (2005). DOI: 10.1364/OL.30.000567.

[18] S. Witte, R. T. Zinkstok, W. Hogervorst, and K. S. E. Eikema, "Generation of few-cycle terawatt light pulses using optical parametric chirped pulse amplification," Opt. Express **13**, 4903 (2005). DOI: 10.1364/OPEX.13.004903.

[19] A. M. Siddiqui, G. Cirmi, D. Brida, F. X. Kärtner, and G. Cerullo, "Generation of <7 fs pulses at 800 nm from a blue-pumped optical

parametric amplifier at degeneracy," Opt. Lett. **34**, 3592 (2009). DOI: 10.1364/OL.34.003592.

[20] T. Stanislauskas, R. Budriūnas, R. Antipenkov, et al., "Table top TW-class OPCPA system driven by tandem femtosecond Yb:KGW and picosecond Nd:YAG lasers," Opt. Express **22**, 1865 (2014). DOI: 10.1364/OE.22.001865.

[21] J. Adamonis, R. Antipenkov, J. Kolenda, et al., "High-energy Nd : YAG-amplification system for OPCPA pumping," Quantum Electron. **42**, 567–574 (2012). DOI: 10.1070/QE2012v042n07ABEH014689.

[22] D. Herrmann, L. Veisz, R. Tautz, et al., "Generation of sub-three-cycle, 16 TW light pulses by using noncollinear optical parametric chirped-pulse amplification," Opt. Lett. **34**, 2459 (2009). DOI: 10.1364/OL.34.002459.

[23] N. Ishii, C. Y. Teisset, T. Fuji, et al., "Seeding of an eleven femtosecond optical parametric chirped pulse amplifier and its Nd^{3+} picosecond pump laser from a single broadband Ti:Sapphire oscillator," IEEE J. Sel. Top. Quantum Electron. **12**, 173–180 (2006). DOI: 10.1109/JSTQE.2006.871930.

[24] H. Fattahi, C. Y. Teisset, O. Pronin, et al., "Pump-seed synchronization for MHz repetition rate, high-power optical parametric chirped pulse amplification," Opt. Express **20**, 9833 (2012). DOI: 10.1364/OE.20.009833.

[25] S. Prinz, M. Häfner, M. Schultze, et al., "Active pump-seed-pulse synchronization for OPCPA with sub-2-fs residual timing jitter," Opt. Express **22**, 31050 (2014). DOI: 10.1364/OE.22.031050.

[26] J. M. Mikhailova, A. Buck, A. Borot, et al., "Ultra-high-contrast few-cycle pulses for multipetawatt-class laser technology," Opt. Lett. **36**, 3145 (2011). DOI: 10.1364/OL.36.003145.

[27] J. Hansryd, P. A. P. A. Andrekson, M. Westlund, et al., "Fiber-based optical parametric amplifiers and their applications," IEEE J. Sel. Top. Quantum Electron. **8**, 506–520 (2002). DOI: 10.1109/JSTQE.2002.1016354.

[28] Z. Yue, K. K. Y. Cheung, Y. Sigang, P. C. Chui, and K. K. Y. Wong, "Ultra-Widely Tunable, Narrow Linewidth Picosecond Fiber-Optical Parametric Oscillator," IEEE Photonics Technol. Lett. **22**, 1756–1758 (2010). DOI: 10.1109/LPT.2010.2085078.

[29] M. E. Marhic †, P. A. Andrekson, P. Petropoulos, et al., "Fiber optical parametric amplifiers in optical communication systems," Laser Photon. Rev. **9**, 50–74 (2015). DOI: 10.1002/lpor.201400087.

[30] K. Viskontas and N. Rusteika, "All-fiber wavelength-tunable picosecond nonlinear reflectivity measurement setup for characterization of semiconductor saturable absorber mirrors," Opt. Fiber Technol. **31**, 74–82 (2016). DOI: 10.1016/j.yofte.2016.06.005.

[31] L. Zhang, S. Yang, X. Wang, et al., "Photonic Crystal Fiber Based Wavelength-Tunable Optical Parametric Amplifier and Picosecond Pulse Generation," IEEE Photonics J. **6**, 1–8 (2014). DOI: 10.1109/JPHOT.2014.2353616.

[32] T. Gottschall, T. Meyer, M. Baumgartl, et al., "Fiber-based optical parametric oscillator for high resolution coherent anti-Stokes Raman scattering (CARS) microscopy," Opt. Express **22**, 21921 (2014). DOI: 10.1364/OE.22.021921.

[33] D. Kraemer, M. L. Cowan, R. Hua, K. Franjic, and R. J. Dwayne Miller, "High-power femtosecond infrared laser source based on noncollinear optical parametric chirped pulse amplification," J. Opt. Soc. Am. B **24**, 813 (2007). DOI: 10.1364/JOSAB.24.000813.

[34] C. Erny, C. Heese, M. Haag, L. Gallmann, and U. Keller, "High-repetition-rate optical parametric chirped-pulse amplifier producing 1-μJ, sub-100-fs pulses in the mid-infrared," Opt. Express **17**, 1340 (2009). DOI: 10.1364/OE.17.001340.

[35] R. Riedel, M. Schulz, M. J. Prandolini, et al., "Long-term stabilization of high power optical parametric chirped-pulse amplifiers," Opt. Express **21**, 28987 (2013). DOI: 10.1364/OE.21.028987.

[36] F. Tavella, A. Willner, J. Rothhardt, et al., "Fiber-amplifier pumped high

average power few-cycle pulse non-collinear OPCPA," Opt. Express **18**, 4689 (2010). DOI: 10.1364/OE.18.004689.

[37] S. Hädrich, S. Demmler, J. Rothhardt, et al., "High-repetition-rate sub-5-fs pulses with 12 GW peak power from fiber-amplifier-pumped optical parametric chirped-pulse amplification.," Opt. Lett. **36**, 313–5 (2011). DOI: 10.1364/OL.36.000313.

[38] J. Rothhardt, S. Demmler, S. Hädrich, J. Limpert, and A. Tünnermann, "Octave-spanning OPCPA system delivering CEP-stable few-cycle pulses and 22 W of average power at 1 MHz repetition rate," Opt. Express **20**, 10870 (2012). DOI: 10.1364/OE.20.010870.

[39] D. Bigourd, L. Lago, A. Mussot, et al., "High-gain fiber, optical-parametric, chirped-pulse amplification of femtosecond pulses at 1 μm.," Opt. Lett. **35**, 3480–3482 (2010). DOI: 10.1364/OL.35.003480.

[40] C. Caucheteur, D. Bigourd, E. Hugonnot, et al., "Experimental demonstration of optical parametric chirped pulse amplification in optical fiber," Opt. Lett. **35**, 1786 (2010). DOI: 10.1364/OL.35.001786.

[41] Y. Zhou, Q. Li, K. K. Y. Cheung, et al., "All-fiber-based ultrashort pulse generation and chirped pulse amplification through parametric processes," IEEE Photonics Technol. Lett. **22**, 1330–1332 (2010). DOI: 10.1109/LPT.2010.2055557.

[42] A. Mussot, A. Kudlinski, P. B. D'Augères, and E. Hugonnot, "Amplification of ultra-short optical pulses in a two-pump fiber optical parametric chirped pulse amplifier.," Opt. Express **21**, 12197–203 (2013). DOI: 10.1364/OE.21.012197.

[43] L. Dong, X. Peng, and J. Li, "Leakage channel optical fibers with large effective area," J. Opt. Soc. Am. B **24**, 1689 (2007). DOI: 10.1364/JOSAB.24.001689.

[44] J. Limpert, F. Stutzki, F. Jansen, et al., "Yb-doped large-pitch fibres: effective single-mode operation based on higher-order mode delocalisation," Light Sci. Appl. **1**, e8 (2012). DOI: 10.1038/lsa.2012.8.

[45] T. T. Alkeskjold, M. Laurila, L. Scolari, and J. Broeng, "Single-mode

ytterbium-doped large-mode-area photonic bandgap rod fiber amplifier," Opt. Express **19**, 7398 (2011). DOI: 10.1364/OE.19.007398.

[46] X. Ma, C. Zhu, I. Hu, A. Kaplan, and A. Galvanauskas, "Single-mode chirally-coupled-core fibers with larger than 50μm diameter cores," Opt. Express **22**, 9206 (2014). DOI: 10.1364/OE.22.009206.

[47] L. Shah and M. Fermann, "High-Power Ultrashort-Pulse Fiber Amplifiers," IEEE J. Sel. Top. Quantum Electron. **13**, 552–558 (2007). DOI: 10.1109/JSTQE.2007.896096.

[48] T. Eidam, J. Rothhardt, F. Stutzki, et al., "Fiber chirped-pulse amplification system emitting 38 GW peak power," Opt. Express **19**, 255 (2011). DOI: 10.1364/OE.19.000255.

[49] M. D. Perry, T. Ditmire, and B. C. Stuart, "Self-phase modulation in chirped-pulse amplification," Opt. Lett. **19**, 2149 (1994). DOI: 10.1364/OL.19.002149.

[50] C. V. Shank and E. P. Ippen, "Subpicosecond kilowatt pulses from a mode-locked cw dye laser," Appl. Phys. Lett. **24**, 373 (1974). DOI: 10.1063/1.1655222.

[51] N. M. Kroll, "Parametric amplification in spatially extended media and application to the design of tuneable oscillators at optical frequencies," Phys. Rev. **127**, 1207–1211 (1962). DOI: 10.1103/PhysRev.127.1207.

[52] C. C. Wang and G. W. Racette, "Measurement of Parametric Gain Accompanying Optical Difference Frequency Generation," Appl. Phys. Lett. **6**, 169 (1965). DOI: 10.1063/1.1754219.

[53] Y. Ishida and T. Yajima, "Characteristics of a new-type SHG crystala β-BaB_2O_4 in the femtosecond region," Opt. Commun. **62**, 197–200 (1987). DOI: 10.1016/0030-4018(87)90027-7.

[54] D. E. Spence, P. N. Kean, and W. Sibbett, "60-fsec pulse generation from a self-mode-locked Ti:sapphire laser," Opt. Lett. **16**, 42 (1991). DOI: 10.1364/OL.16.000042.

[55] T. B. Norris, "Femtosecond pulse amplification at 250 kHz with a Ti:sapphire regenerative amplifier and application to continuum

generation," Opt. Lett. **17**, 1009 (1992). DOI: 10.1364/OL.17.001009.

[56] T. Brabec and F. Krausz, "Intense few-cycle laser fields: Frontiers of nonlinear optics," Rev. Mod. Phys. **72**, 545–591 (2000). DOI: 10.1103/RevModPhys.72.545.

[57] M. K. Reed, M. K. Steiner-Shepard, M. S. Armas, and D. K. Negus, "Microjoule-energy ultrafast optical parametric amplifiers," J. Opt. Soc. Am. B **12**, 2229 (1995). DOI: 10.1364/JOSAB.12.002229.

[58] S. R. Greenfield and M. R. Wasielewski, "Near-transform-limited visible and near-IR femtosecond pulses from optical parametric amplification using Type II β-barium borate," Opt. Lett. **20**, 1394 (1995). DOI: 10.1364/OL.20.001394.

[59] V. Petrov, F. Seifert, and F. Noack, "Visible optical parametric generator producing nearly bandwidth-limited femtosecond light pulses at 1-kHz repetition rate," Appl. Opt. **33**, 6988 (1994). DOI: 10.1364/AO.33.006988.

[60] R. Danielius, G. P. Banfi, P. Di Trapani, et al., "Traveling-wave parametric generation of widely tunable, highly coherent femtosecond light pulses," J. Opt. Soc. Am. B **10**, 2222 (1993). DOI: 10.1364/JOSAB.10.002222.

[61] R. Danielius, A. Piskarskas, P. Di Trapani, et al., "Visible pulses of 100 fs and 100 μJ from an upconverted parametric generator," Appl. Opt. **35**, 5336 (1996). DOI: 10.1364/AO.35.005336.

[62] M. K. Reed, M. S. Armas, M. K. Steiner-Shepard, and D. K. Negus, "30-fs pulses tunable across the visible with a 100-kHz Ti:sapphire regenerative amplifier," Opt. Lett. **20**, 605 (1995). DOI: 10.1364/OL.20.000605.

[63] T. Wilhelm, J. Piel, and E. Riedle, "Sub-20-fs pulses tunable across the visible from a blue-pumped single-pass noncollinear parametric converter," Opt. Lett. **22**, 1494 (1997). DOI: 10.1364/OL.22.001494.

[64] A. Shirakawa and T. Kobayashi, "Noncollinearly phase-matched femtosecond optical parametric amplification with a 2000 cm^{-1}

bandwidth," Appl. Phys. Lett. **72**, 147 (1998). DOI: 10.1063/1.120670.

[65] A. V. Smith, "How to select nonlinear crystals and model their performance using SNLO software," in *Proceedings of SPIE*, J. W. Pierce, ed. (2000), Vol. 3928, p. 62. DOI: 10.1117/12.379931.

[66] L. Shen and D. Fan, "Theoretical research on noncollinear match conditions of the type I optical parametric process," J. Opt. Soc. Am. B **24**, 90 (2007). DOI: 10.1364/JOSAB.24.000090.

[67] G. M. Gale, M. Cavallari, T. J. Driscoll, and F. Hache, "Sub-20-fs tunable pulses in the visible from an 82-MHz optical parametric oscillator," Opt. Lett. **20**, 1562 (1995). DOI: 10.1364/OL.20.001562.

[68] A. Baltuška, T. Fuji, and T. Kobayashi, "Visible pulse compression to 4 fs by optical parametric amplification and programmable dispersion control," Opt. Lett. **27**, 306 (2002). DOI: 10.1364/OL.27.000306.

[69] D. Strickland and G. Mourou, "Compression of amplified chirped optical pulses," Opt. Commun. **56**, 219–221 (1985). DOI: 10.1016/0030-4018(85)90120-8.

[70] A. Dubietis, G. Jonušauskas, and A. Piskarskas, "Powerful femtosecond pulse generation by chirped and stretched pulse parametric amplification in BBO crystal," Opt. Commun. **88**, 437–440 (1992). DOI: 10.1016/0030-4018(92)90070-8.

[71] I. N. Ross, P. Matousek, M. Towrie, A. J. Langley, and J. L. Collier, "The prospects for ultrashort pulse duration and ultrahigh intensity using optical parametric chirped pulse amplifiers," Opt. Commun. **144**, 125–133 (1997). DOI: 10.1016/S0030-4018(97)00399-4.

[72] J. Moses, C. Manzoni, S.-W. Huang, G. Cerullo, and F. X. Kaertner, "Temporal optimization of ultrabroadband high-energy OPCPA," Opt. Express **17**, 5540 (2009). DOI: 10.1364/OE.17.005540.

[73] A. Vaupel, N. Bodnar, B. Webb, L. Shah, and M. Richardson, "Concepts, performance review, and prospects of table-top, few-cycle optical parametric chirped-pulse amplification," Opt. Eng. **53**, 51507 (2013). DOI: 10.1117/1.OE.53.5.051507.

[74] S. Adachi, N. Ishii, T. Kanai, et al., "5-fs, multi-mJ, CEP-locked parametric chirped-pulse amplifier pumped by a 450-nm source at 1 kHz," Opt. Express **16**, 14341 (2008). DOI: 10.1364/OE.16.014341.

[75] V. V. Lozhkarev, G. I. Freidman, V. N. Ginzburg, et al., "Compact 0.56 Petawatt laser system based on optical parametric chirped pulse amplification in KD*P crystals," Laser Phys. Lett. **4**, 421–427 (2007). DOI: 10.1002/lapl.200710008.

[76] O. V Chekhlov, J. L. Collier, I. N. Ross, et al., "35 J broadband femtosecond optical parametric chirped pulse amplification system," Opt. Lett. **31**, 3665 (2006). DOI: 10.1364/OL.31.003665.

[77] C. Skrobol, I. Ahmad, S. Klingebiel, et al., "Broadband amplification by picosecond OPCPA in DKDP pumped at 515 nm," Opt. Express **20**, 4619 (2012). DOI: 10.1364/OE.20.004619.

[78] O. Novák, M. Divoký, H. Turčičová, and P. Straka, "Design of a petawatt optical parametric chirped pulse amplification upgrade of the kilojoule iodine laser PALS," Laser Part. Beams **31**, 211–218 (2013). DOI: 10.1017/S0263034613000189.

[79] C. Danson, D. Hillier, N. Hopps, and D. Neely, "Petawatt class lasers worldwide," High Power Laser Sci. Eng. **3**, 1–14 (2015). DOI: 10.1017/hpl.2014.52.

[80] X. Wang, R. Zgadzaj, N. Fazel, et al., "Quasi-monoenergetic laser-plasma acceleration of electrons to 2 GeV," Nat. Commun. **4**, 1988 (2013). DOI: 10.1038/ncomms2988.

[81] S. M. Hooker, "Developments in laser-driven plasma accelerators," Nat. Photonics **7**, 775–782 (2013). DOI: 10.1038/nphoton.2013.234.

[82] H. Fattahi, H. G. Barros, M. Gorjan, et al., "Third-generation femtosecond technology," Optica **1**, 45 (2014). DOI: 10.1364/OPTICA.1.000045.

[83] M. Schultze, T. Binhammer, G. Palmer, et al., "Multi-μJ, CEP-stabilized, two-cycle pulses from an OPCPA system with up to 500 kHz repetition rate," Opt. Express **18**, 27291–27297 (2010). DOI: 10.1364/OE.18.027291.

[84] G. Andriukaitis, T. Balčiūnas, S. Ališauskas, et al., "90 GW peak power few-cycle mid-infrared pulses from an optical parametric amplifier," Opt. Lett. **36**, 2755 (2011). DOI: 10.1364/OL.36.002755.

[85] O. Chalus, P. K. Bates, M. Smolarski, and J. Biegert, "Mid-IR short-pulse OPCPA with micro-Joule energy at 100 kHz.," Opt. Express **17**, 3587 (2009). DOI: 10.1364/OE.17.003587.

[86] D. Sanchez, M. Hemmer, M. Baudisch, et al., "7 μm, ultrafast, sub-millijoule-level mid-infrared optical parametric chirped pulse amplifier pumped at 2 μm," Optica **3**, 147 (2016). DOI: 10.1364/OPTICA.3.000147.

[87] M. Hemmer, D. Sánchez, M. Jelínek, et al., "2-μm wavelength, high-energy Ho:YLF chirped-pulse amplifier for mid-infrared OPCPA," Opt. Lett. **40**, 451–454 (2015). DOI: 10.1364/OL.40.000451.

[88] R. T. Zinkstok, S. Witte, W. Hogervorst, and K. S. E. Eikema, "High-power parametric amplification of 118-fs laser pulses with carrier-envelope phase control," Opt. Lett. **30**, 78 (2005). DOI: 10.1364/OL.30.000078.

[89] J. V. Rudd, R. J. Law, T. S. Luk, and S. M. Cameron, "High-power optical parametric chirped-pulse amplifier system with a 155 μm signal and a 1064 μm pump," Opt. Lett. **30**, 1974 (2005). DOI: 10.1364/OL.30.001974.

[90] D. Kraemer, R. Hua, M. L. Cowan, K. Franjic, and R. J. D. Miller, "Ultrafast noncollinear optical parametric chirped pulse amplification in KTiOAsO_4," Opt. Lett. **31**, 981 (2006). DOI: 10.1364/OL.31.000981.

[91] C. Y. Teisset, N. Ishii, T. Fuji, et al., "Soliton-based pump-seed synchronization for few-cycle OPCPA," Opt. Express **13**, 6550 (2005). DOI: 10.1364/OPEX.13.006550.

[92] M. Schultze, T. Binhammer, A. Steinmann, et al., "Few-cycle OPCPA system at 143 kHz with more than 1 μJ of pulse energy," Opt. Express **18**, 2836 (2010). DOI: 10.1364/OE.18.002836.

[93] D. Yoshitomi, X. Zhou, Y. Kobayashi, H. Takada, and K. Torizuka, "Long-term stable passive synchronization of 50 μJ femtosecond Yb-

doped fiber chirped-pulse amplifier with a mode-locked Ti:sapphire laser," Opt. Express **18**, 26027 (2010). DOI: 10.1364/OE.18.026027.

[94] D. Yoshitomi, Y. Kobayashi, M. Kakehata, et al., "Ultralow-Jitter Passive Timing Stabilization of a Mode-Locked Fiber Laser by Injection of Reference Pulses," in *2007 Conference on Lasers and Electro-Optics (CLEO)* (IEEE, 2007), pp. 1–2. DOI: 10.1109/CLEO.2007.4452582.

[95] G. Cerullo, M. Nisoli, and S. De Silvestri, "Generation of 11 fs pulses tunable across the visible by optical parametric amplification," Appl. Phys. Lett. **71**, 3616 (1997). DOI: 10.1063/1.120458.

[96] R. Danilevičius, A. Zaukevičius, R. Budriūnas, A. Michailovas, and N. Rusteika, "Femtosecond wavelength-tunable OPCPA system based on picosecond fiber laser seed and picosecond DPSS laser pump," Opt. Express **24**, 17532 (2016). DOI: 10.1364/OE.24.017532.

[97] G. Cerullo, M. Nisoli, S. Stagira, and S. De Silvestri, "Sub-8-fs pulses from an ultrabroadband optical parametric amplifier in the visible," Opt. Lett. **23**, 1283 (1998). DOI: 10.1364/OL.23.001283.

[98] A. Shirakawa, I. Sakane, and T. Kobayashi, "Pulse-front-matched optical parametric amplification for sub-10-fs pulse generation tunable in the visible and near infrared," Opt. Lett. **23**, 1292 (1998). DOI: 10.1364/OL.23.001292.

[99] A. Shirakawa, I. Sakane, M. Takasaka, and T. Kobayashi, "Sub-5-fs visible pulse generation by pulse-front-matched noncollinear optical parametric amplification," Appl. Phys. Lett. **74**, 2268 (1999). DOI: 10.1063/1.123820.

[100] D. Zeidler, T. Hornung, D. Proch, and M. Motzkus, "Adaptive compression of tunable pulses from a non-collinear-type OPA to below 16 fs by feedback-controlled pulse shaping," Appl. Phys. B **70**, S125–S131 (2000). DOI: 10.1007/s003400000306.

[101] J. Želudevičius, R. Danilevičius, K. Viskontas, N. Rusteika, and K. Regelskis, "Femtosecond fiber CPA system based on picosecond master oscillator and power amplifier with CCC fiber," Opt. Express **21**, 5338

(2013). DOI: 10.1364/OE.21.005338.

[102] O. Martinez, "3000 times grating compressor with positive group velocity dispersion: Application to fiber compensation in 1.3-1.6 μm region," IEEE J. Quantum Electron. **23**, 59–64 (1987). DOI: 10.1109/JQE.1987.1073201.

[103] P. Maine, D. Strickland, P. Bado, M. Pessot, and G. Mourou, "Generation of ultrahigh peak power pulses by chirped pulse amplification," IEEE J. Quantum Electron. **24**, 398–403 (1988). DOI: 10.1109/3.137.

[104] B. E. Lemoff and C. P. J. Barty, "Quintic-phase-limited, spatially uniform expansion and recompression of ultrashort optical pulses," Opt. Lett. **18**, 1651 (1993). DOI: 10.1364/OL.18.001651.

[105] A. Offner, "Unit Power Imaging Catoptric Anastigmat," U.S. patent US 3748015 A (1973).

[106] G. Cheriaux, B. Walker, L. F. Dimauro, et al., "Aberration-free stretcher design for ultrashort-pulse amplification," Opt. Lett. **21**, 414 (1996). DOI: 10.1364/OL.21.000414.

[107] E. Treacy, "Optical pulse compression with diffraction gratings," IEEE J. Quantum Electron. **5**, 454–458 (1969). DOI: 10.1109/JQE.1969.1076303.

[108] W. A. Molander, A. J. Bayramian, R. Campbell, et al., "A Large-Bandwidth, Cylindrical Offner Pulse Stretcher for a High-Average-Power, 15 Femtosecond Laser," in *Advanced Solid State Photonics Conference* (2009), pp. 7–9.

[109] M. P. Kalachnikov, V. Karpov, H. Schönnagel, and W. Sandner, "100-Terawatt Titanium–Sapphire Laser System," Laser Phys. **12**, 368–374 (2002).

[110] D. Du, C. Bogusch, C. T. Cotton, et al., "Terawatt Ti:sapphire laser with a spherical reflective-optic pulse expander," Opt. Lett. **20**, 2114 (1995). DOI: 10.1364/OL.20.002114.

[111] G. Chériaux, O. Albert, V. Wänman, et al., "Temporal control of amplified femtosecond pulses with a deformable mirror in a stretcher," Opt. Lett. **26**, 169 (2001). DOI: 10.1364/OL.26.000169.

[112] H. Takada, M. Kakehata, and K. Torizuka, "Large-ratio stretch and recompression of sub-10-fs pulses utilizing dispersion managed devices and a spatial light modulator," Appl. Phys. B **74**, s253–s257 (2002). DOI: 10.1007/s00340-002-0883-y.

[113] V. Bagnoud and F. Salin, "Influence of optical quality on chirped-pulse amplification: characterization of a 150-nm-bandwidth stretcher," J. Opt. Soc. Am. B **16**, 188 (1999). DOI: 10.1364/JOSAB.16.000188.

[114] V. E. Leshchenko, V. A. Vasiliev, N. L. Kvashnin, and E. V. Pestryakov, "Coherent combining of relativistic-intensity femtosecond laser pulses," Appl. Phys. B **118**, 511–516 (2015). DOI: 10.1007/s00340-015-6047-7.

[115] S. Witte, R. T. Zinkstok, A. L. Wolf, et al., "A source of 2 terawatt, 2.7 cycle laser pulses based on noncollinear optical parametric chirped pulse amplification," Opt. Express **14**, 8168 (2006). DOI: 10.1364/OE.14.008168.

[116] P. Tournois, "Acousto-optic programmable dispersive filter for adaptive compensation of group delay time dispersion in laser systems," Opt. Commun. **140**, 245–249 (1997). DOI: 10.1016/S0030-4018(97)00153-3.

[117] T. Fuji, N. Ishii, C. Y. Teisset, et al., "Parametric amplification of few-cycle carrier-envelope phase-stable pulses at 2.1 μm," Opt. Lett. **31**, 1103 (2006). DOI: 10.1364/OL.31.001103.

[118] J. Zheng and H. Zacharias, "Design considerations for a compact grism stretcher for non-collinear optical parametric chirped-pulse amplification," Appl. Phys. B **96**, 445–452 (2009). DOI: 10.1007/s00340-009-3410-6.

[119] S. Kane and J. Squier, "Grism-pair stretcher–compressor system for simultaneous second- and third-order dispersion compensation in chirped-pulse amplification," J. Opt. Soc. Am. B **14**, 661 (1997). DOI: 10.1364/JOSAB.14.000661.

[120] K.-H. Hong, J. T. Gopinath, D. Rand, et al., "High-energy, kHz-repetition-rate, ps cryogenic Yb:YAG chirped-pulse amplifier," Opt. Lett. **35**, 1752 (2010). DOI: 10.1364/OL.35.001752.

[121] M. Schulz, R. Riedel, A. Willner, et al., "Yb:YAG Innoslab amplifier: efficient high repetition rate subpicosecond pumping system for optical parametric chirped pulse amplification," Opt. Lett. **36**, 2456 (2011). DOI: 10.1364/OL.36.002456.

[122] R. R. Alfano and S. L. Shapiro, "Emission in the Region 4000 to 7000 Å Via Four-Photon Coupling in Glass," Phys. Rev. Lett. **24**, 584–587 (1970). DOI: 10.1103/PhysRevLett.24.584.

[123] A. Couairon and A. Mysyrowicz, "Femtosecond filamentation in transparent media," Phys. Rep. **441**, 47–189 (2007). DOI: 10.1016/j.physrep.2006.12.005.

[124] J. M. Dudley, G. Genty, and S. Coen, "Supercontinuum generation in photonic crystal fiber," Rev. Mod. Phys. **78**, 1135–1184 (2006). DOI: 10.1103/RevModPhys.78.1135.

[125] M. Adachi, K. Yamane, R. Morita, and M. Yamashita, "Sub-5-fs Pulse Compression of Laser Output Using Photonic Crystal Fiber with Short Zero-Dispersion Wavelength," Jpn. J. Appl. Phys. **44**, L1423–L1425 (2005). DOI: 10.1143/JJAP.44.L1423.

[126] A. Brodeur and S. L. Chin, "Ultrafast white-light continuum generation and self-focusing in transparent condensed media," J. Opt. Soc. Am. B **16**, 637 (1999). DOI: 10.1364/JOSAB.16.000637.

[127] C. Nagura, A. Suda, H. Kawano, M. Obara, and K. Midorikawa, "Generation and characterization of ultrafast white-light continuum in condensed media," Appl. Opt. **41**, 3735 (2002). DOI: 10.1364/AO.41.003735.

[128] M. Bradler, P. Baum, and E. Riedle, "Femtosecond continuum generation in bulk laser host materials with sub-μJ pump pulses," Appl. Phys. B **97**, 561–574 (2009). DOI: 10.1007/s00340-009-3699-1.

[129] V. Jukna, J. Galinis, G. Tamosauskas, D. Majus, and A. Dubietis, "Infrared extension of femtosecond supercontinuum generated by filamentation in solid-state media," Appl. Phys. B Lasers Opt. **116**, 477–483 (2014). DOI: 10.1007/s00340-013-5723-8.

[130] A. L. Gaeta, "Catastrophic Collapse of Ultrashort Pulses," Phys. Rev. Lett. **84**, 3582–3585 (2000). DOI: 10.1103/PhysRevLett.84.3582.

[131] A. Brodeur and S. L. Chin, "Band-Gap Dependence of the Ultrafast White-Light Continuum," Phys. Rev. Lett. **80**, 4406–4409 (1998). DOI: 10.1103/PhysRevLett.80.4406.

[132] J. Darginavičius, D. Majus, V. Jukna, et al., "Ultrabroadband supercontinuum and third-harmonic generation in bulk solids with two optical-cycle carrier-envelope phase-stable pulses at 2 μm," Opt. Express **21**, 25210 (2013). DOI: 10.1364/OE.21.025210.

[133] N. P. Ernsting, S. a Kovalenko, T. Senyushkina, J. Saam, and V. Farztdinov, "Wave-Packet-Assisted Decomposition of Femtosecond Transient Ultraviolet−Visible Absorption Spectra: Application to Excited-State Intramolecular Proton Transfer in Solution," J. Phys. Chem. A **105**, 3443–3453 (2001). DOI: 10.1021/jp003298o.

[134] U. Megerle, I. Pugliesi, C. Schriever, C. F. Sailer, and E. Riedle, "Sub-50 fs broadband absorption spectroscopy with tunable excitation: putting the analysis of ultrafast molecular dynamics on solid ground," Appl. Phys. B **96**, 215–231 (2009). DOI: 10.1007/s00340-009-3610-0.

[135] D. Brida, C. Manzoni, G. Cirmi, et al., "Few-optical-cycle pulses tunable from the visible to the mid-infrared by optical parametric amplifiers," J. Opt. **12**, 13001 (2010). DOI: 10.1088/2040-8978/12/1/013001.

[136] G. Cerullo, C. Manzoni, L. Lüer, and D. Polli, "Time-resolved methods in biophysics. 4. Broadband pump–probe spectroscopy system with sub-20 fs temporal resolution for the study of energy transfer processes in photosynthesis," Photochem. Photobiol. Sci. **6**, 135–144 (2007). DOI: 10.1039/B606949E.

[137] D. Faccio, A. Averchi, A. Lotti, et al., "Generation and control of extreme blueshifted continuum peaks in optical Kerr media," Phys. Rev. A **78**, 33825 (2008). DOI: 10.1103/PhysRevA.78.033825.

[138] J. Galinis, G. Tamošauskas, I. Gražulevičiūtė, et al., "Filamentation and supercontinuum generation in solid-state dielectric media with picosecond

laser pulses," Phys. Rev. A **92**, 33857 (2015). DOI: 10.1103/PhysRevA.92.033857.

[139] R. Riedel, A. Stephanides, M. J. Prandolini, et al., "Power scaling of supercontinuum seeded megahertz-repetition rate optical parametric chirped pulse amplifiers," Opt. Lett. **39**, 1422 (2014). DOI: 10.1364/OL.39.001422.

[140] M. Nisoli, G. Sansone, S. Stagira, et al., "Effects of Carrier-Envelope Phase Differences of Few-Optical-Cycle Light Pulses in Single-Shot High-Order-Harmonic Spectra," Phys. Rev. Lett. **91**, 213905 (2003). DOI: 10.1103/PhysRevLett.91.213905.

[141] G. Cerullo, A. Baltuška, O. D. Mücke, and C. Vozzi, "Few-optical-cycle light pulses with passive carrier-envelope phase stabilization," Laser Photon. Rev. **5**, 323–351 (2011). DOI: 10.1002/lpor.201000013.

[142] A. Baltuška, T. Fuji, and T. Kobayashi, "Controlling the Carrier-Envelope Phase of Ultrashort Light Pulses with Optical Parametric Amplifiers," Phys. Rev. Lett. **88**, 133901 (2002). DOI: 10.1103/PhysRevLett.88.133901.

[143] Y. Deng, A. Schwarz, H. Fattahi, et al., "Carrier-envelope-phase-stable, 1.2 mJ, 1.5 cycle laser pulses at 2.1 μm," Opt. Lett. **37**, 4973 (2012). DOI: 10.1364/OL.37.004973.

[144] R. Budriūnas, T. Stanislauskas, and A. Varanavičius, "Passively CEP-stabilized frontend for few cycle terawatt OPCPA system," J. Opt. **17**, 94008 (2015). DOI: 10.1088/2040-8978/17/9/094008.

[145] M. E. Fermann and I. Hartl, "Ultrafast fibre lasers," Nat. Photonics **7**, 868–874 (2013). DOI: 10.1038/nphoton.2013.280.

[146] W. Zhao, X. Hu, and Y. Wang, "Femtosecond-Pulse Fiber Based Amplification Techniques and Their Applications," IEEE J. Sel. Top. Quantum Electron. **20**, 512–524 (2014). DOI: 10.1109/JSTQE.2014.2308396.

[147] M. Müller, M. Kienel, A. Klenke, et al., "1 kW 1 mJ eight-channel ultrafast fiber laser," Opt. Lett. **41**, 3439 (2016). DOI:

10.1364/OL.41.003439.

[148] U. Keller, K. J. Weingarten, F. X. Kartner, et al., "Semiconductor saturable absorber mirrors (SESAM's) for femtosecond to nanosecond pulse generation in solid-state lasers," IEEE J. Sel. Top. Quantum Electron. **2**, 435–453 (1996). DOI: 10.1109/2944.571743.

[149] A. Isomäki and O. G. Okhotnikov, "All-fiber ytterbium soliton mode-locked laser with dispersion control by solid-core photonic bandgap fiber," Opt. Express **14**, 4368 (2006). DOI: 10.1364/OE.14.004368.

[150] R. Gumenyuk, I. Vartiainen, H. Tuovinen, et al., "Dispersion compensation technologies for femtosecond fiber system," Appl. Opt. **50**, 797 (2011). DOI: 10.1364/AO.50.000797.

[151] K. Viskontas, K. Regelskis, and N. Rusteika, "Slow and fast optical degradation of the SESAM for fiber laser mode-locking at 1 μm," Lith. J. Phys. **54**, 127–135 (2014). DOI: 10.3952/physics.v54i3.2951.

[152] F. Ilday, J. Buckley, L. Kuznetsova, and F. Wise, "Generation of 36-femtosecond pulses from a ytterbium fiber laser," Opt. Express **11**, 3550 (2003). DOI: 10.1364/OE.11.003550.

[153] C. Aguergaray, N. G. R. Broderick, M. Erkintalo, J. S. Y. Chen, and V. Kruglov, "Mode-locked femtosecond all-normal all-PM Yb-doped fiber laser using a nonlinear amplifying loop mirror," Opt. Express **20**, 10545 (2012). DOI: 10.1364/OE.20.010545.

[154] A. Chong, J. Buckley, W. Renninger, and F. Wise, "All-normal-dispersion femtosecond fiber laser," Opt. Express **14**, 10095 (2006). DOI: 10.1364/OE.14.010095.

[155] Z. Zhang, Ç. Şenel, R. Hamid, et al., "Sub-50 fs Yb-doped laser with anomalous-dispersion photonic crystal fiber," Opt. Lett. **38**, 956 (2013). DOI: 10.1364/OL.38.000956.

[156] G. P. Agrawal, *Nonlinear Fiber Optics 4th Edition* (Elsevier, 2007). ISBN: 978-0-12-369516-1.

[157] W. Hu, Y. C. Shin, and G. King, "Modeling of multi-burst mode pico-second laser ablation for improved material removal rate," Appl. Phys. A

98, 407–415 (2010). DOI: 10.1007/s00339-009-5405-x.

[158] M. E. Fermann, "Single-mode excitation of multimode fibers with ultrashort pulses," Opt. Lett. **23**, 52 (1998). DOI: 10.1364/OL.23.000052.

[159] J. P. Koplow, D. A. V. Kliner, and L. Goldberg, "Single-mode operation of a coiled multimode fiber amplifier," Opt. Lett. **25**, 442 (2000). DOI: 10.1364/OL.25.000442.

[160] X. Ma, C.-H. Liu, G. Chang, and A. Galvanauskas, "Angular-momentum coupled optical waves in chirally-coupled-core fibers," Opt. Express **19**, 26515 (2011). DOI: 10.1364/OE.19.026515.

[161] W. S. Wong, X. Peng, J. M. McLaughlin, and L. Dong, "Breaking the limit of maximum effective area for robust single-mode propagation in optical fibers," Opt. Lett. **30**, 2855 (2005). DOI: 10.1364/OL.30.002855.

[162] F. Stutzki, F. Jansen, T. Eidam, et al., "High average power large-pitch fiber amplifier with robust single-mode operation," Opt. Lett. **36**, 689 (2011). DOI: 10.1364/OL.36.000689.

[163] S. Ramachandran, J. W. Nicholson, S. Ghalmi, et al., "Light propagation with ultralarge modal areas in optical fibers.," Opt. Lett. **31**, 1797–1799 (2006). DOI: 10.1364/OL.31.001797.

[164] S. Ramachandran, J. M. Fini, M. Mermelstein, et al., "Ultra-large effective-area, higher-order mode fibers: a new strategy for high-power lasers," Laser Photonics Rev. **2**, 429–448 (2008). DOI: 10.1002/lpor.200810016.

[165] X. Peng, K. Kim, M. Mielke, et al., "Higher-order mode fiber enables high energy chirped-pulse amplification," Opt. Express **21**, 32411 (2013). DOI: 10.1364/OE.21.032411.

[166] M. Kienel, A. Klenke, T. Eidam, et al., "Energy scaling of femtosecond amplifiers using actively controlled divided-pulse amplification," Opt. Lett. **39**, 1049 (2014). DOI: 10.1364/OL.39.001049.

[167] S. Zhou, D. G. Ouzounov, and F. W. Wise, "Divided-pulse Amplification of Ultrashort Pulses," in *2007 Conference on Lasers and Electro-Optics (CLEO)* (IEEE, 2007), pp. 1–2. DOI: 10.1109/CLEO.2007.4453041.

[168] M. Kienel, M. Müller, A. Klenke, J. Limpert, and A. Tünnermann, "12 mJ kW-class ultrafast fiber laser system using multidimensional coherent pulse addition," Opt. Lett. **41**, 3343 (2016). DOI: 10.1364/OL.41.003343.

[169] I. Hartl, A. Marcinkevičius, H. A. McKay, L. Dong, and M. E. Fermann, "Coherent Beam Combination Using Multi-Core Leakage-Channel Fibers," in *Advanced Solid-State Photonics* (OSA, 2009), p. TuA6. DOI: 10.1364/ASSP.2009.TuA6.

[170] M. Hanna, F. Guichard, Y. Zaouter, et al., "Coherent combination of ultrafast fiber amplifiers," J. Phys. B At. Mol. Opt. Phys. **49**, 62004 (2016). DOI: 10.1088/0953-4075/49/6/062004.

[171] V. I. Kruglov, A. C. Peacock, J. D. Harvey, and J. M. Dudley, "Self-similar propagation of parabolic pulses in normal-dispersion fiber amplifiers," J. Opt. Soc. Am. B **19**, 461 (2002). DOI: 10.1364/JOSAB.19.000461.

[172] M. E. Fermann, V. I. Kruglov, B. C. Thomsen, J. M. Dudley, and J. D. Harvey, "Self-Similar Propagation and Amplification of Parabolic Pulses in Optical Fibers," Phys. Rev. Lett. **84**, 6010–6013 (2000). DOI: 10.1103/PhysRevLett.84.6010.

[173] A. Chong, H. Liu, B. Nie, et al., "Pulse generation without gain-bandwidth limitation in a laser with self-similar evolution," Opt. Express **20**, 14213 (2012). DOI: 10.1364/OE.20.014213.

[174] Y. Zaouter, J. Boullet, E. Mottay, and E. Cormier, "Transform-limited 100 μJ, 340 MW pulses from a nonlinear-fiber chirped-pulse amplifier using a mismatched grating stretcher–compressor," Opt. Lett. **33**, 1527 (2008). DOI: 10.1364/OL.33.001527.

[175] F. Röser, T. Eidam, J. Rothhardt, et al., "Millijoule pulse energy high repetition rate femtosecond fiber chirped-pulse amplification system," Opt. Lett. **32**, 3495 (2007). DOI: 10.1364/OL.32.003495.

[176] A. Galvanauskas, M. E. Fermann, D. Harter, K. Sugden, and I. Bennion, "All-fiber femtosecond pulse amplification circuit using chirped Bragg gratings," Appl. Phys. Lett. **66**, 1053 (1995). DOI: 10.1063/1.113571.

[177] J. Limpert, T. Schreiber, S. Nolte, H. Zellmer, and A. Tünnermann, "All fiber chirped-pulse amplification system based on compression in air-guiding photonic bandgap fiber," Opt. Express **11**, 3332 (2003). DOI: 10.1364/OE.11.003332.

[178] L. Glebov, V. Smirnov, E. Rotari, et al., "Volume-chirped Bragg gratings: monolithic components for stretching and compression of ultrashort laser pulses," Opt. Eng. **53**, 51514 (2014). DOI: 10.1117/1.OE.53.5.051514.

[179] S. Hädrich, A. Klenke, A. Hoffmann, et al., "Nonlinear compression to sub-30-fs, 05 mJ pulses at 135 W of average power," Opt. Lett. **38**, 3866 (2013). DOI: 10.1364/OL.38.003866.

[180] I. Pupeza, S. Holzberger, T. Eidam, et al., "Compact high-repetition-rate source of coherent 100 eV radiation," Nat. Photonics **7**, 608–612 (2013). DOI: 10.1038/nphoton.2013.156.

[181] M. Krebs, S. Hädrich, S. Demmler, et al., "Towards isolated attosecond pulses at megahertz repetition rates," Nat. Photonics **7**, 555–559 (2013). DOI: 10.1038/nphoton.2013.131.

[182] S. Hädrich, M. Kienel, M. Müller, et al., "Energetic sub-2-cycle laser with 216 W average power," Opt. Lett. **41**, 4332 (2016). DOI: 10.1364/OL.41.004332.

[183] D. U. Noske, N. Pandit, and J. R. Taylor, "Source of spectral and temporal instability in soliton fiber lasers," Opt. Lett. **17**, 1515 (1992). DOI: 10.1364/OL.17.001515.

[184] O. Katz, Y. Sintov, Y. Nafcha, and Y. Glick, "Passively mode-locked ytterbium fiber laser utilizing chirped-fiber-Bragg-gratings for dispersion control," Opt. Commun. **269**, 156–165 (2007). DOI: 10.1016/j.optcom.2006.07.034.

[185] V. Loriot, G. Gitzinger, and N. Forget, "Self-referenced characterization of femtosecond laser pulses by chirp scan," Opt. Express **21**, 24879 (2013). DOI: 10.1364/OE.21.024879.

[186] M. Tsang, D. Psaltis, and F. G. Omenetto, "Reverse propagation of femtosecond pulses in optical fibers," Opt. Lett. **28**, 1873 (2003). DOI:

10.1364/OL.28.001873.

[187] R. Kashyap, *Fiber Bragg Gratings*, 2nd ed. (Academic Press, Elsevier, 2010). ISBN: 978-0-12-372579-0. DOI: 10.1016/B978-0-12-372579-0.00012-0.

[188] S. Matsumoto, T. Ohira, M. Takabayashi, K. Yoshiara, and T. Sugihara, "Tunable dispersion equalizer with a divided thin-film heater for 40-Gb/s RZ transmissions," IEEE Photonics Technol. Lett. **13**, 827–829 (2001). DOI: 10.1109/68.935817.

[189] T. Sugihara, K. Ishida, K. Shimomura, K. Shimizu, and Y. Kobayashi, "Adaptive dispersion compensation for 40 Gbit/s RZ transmission by using Bragg gratings," IEICE Trans. Commun. **84**, 1153–1158 (2001).

[190] D. N. Schimpf, E. Seise, J. Limpert, and A. Tünnermann, "The impact of spectral modulations on the contrast of pulses of nonlinear chirped-pulse amplification systems," Opt. Express **16**, 10664 (2008). DOI: 10.1364/OE.16.010664.

[191] O. Martinez, "Design of high-power ultrashort pulse amplifiers by expansion and recompression," IEEE J. Quantum Electron. **23**, 1385–1387 (1987). DOI: 10.1109/JQE.1987.1073518.

[192] D. J. Kane and R. Trebino, "Characterization of arbitrary femtosecond pulses using frequency-resolved optical gating," IEEE J. Quantum Electron. **29**, 571–579 (1993). DOI: 10.1109/3.199311.

[193] A. P. Stabinis and G. Valiulis, *Ultratrumpųjų Šviesos Impulsų Netiesinė Optika* (TEV, 2008). ISBN: 9789955879282.

[194] G. P. Agrawal, *Fiber-Optic Cummunication Systems*, 3rd ed. (Wiley, 2002). ISBN: 0-471-21571-6.

[195] J. Želudevičius, R. Danilevičius, and K. Regelskis, "Optimization of pulse compression in a fiber chirped pulse amplification system by adjusting dispersion parameters of a temperature-tuned chirped fiber Bragg grating stretcher," J. Opt. Soc. Am. B **32**, 812 (2015). DOI: 10.1364/JOSAB.32.000812.

[196] A. E. Siegman, *Lasers* (University Science Books, 1986). ISBN: 0-

935702-11-3.

[197] L. Shah, Z. Liu, I. Hartl, et al., "High energy femtosecond Yb cubicon fiber amplifier," Opt. Express **13**, 4717 (2005). DOI: 10.1364/OPEX.13.004717.

[198] W. J. Tomlinson, R. H. Stolen, and C. V. Shank, "Compression of optical pulses chirped by self-phase modulation in fibers," J. Opt. Soc. Am. B **1**, 139 (1984). DOI: 10.1364/JOSAB.1.000139.

[199] A. M. Weiner, *Ultrafast Optics* (Wiley, 2009). ISBN: 9780470473467.

[200] W. Press, B. Flannery, S. Teukolsky, and W. Vetterling, *Numerical Recipes: The Art of Scientific Computing* (Cambridge University Press, 2007). ISBN: 978-0-521-88068-8.

[201] J. Lægsgaard, "Control of fibre laser mode-locking by narrow-band Bragg gratings," J. Phys. B At. Mol. Opt. Phys. **41**, 95401 (2008). DOI: 10.1088/0953-4075/41/9/095401.

[202] T. Erdogan, "Fiber grating spectra," J. Light. Technol. **15**, 1277–1294 (1997). DOI: 10.1109/50.618322.

[203] W. H. Bragg and W. L. Bragg, "The Reflection of X-rays by Crystals," Proc. R. Soc. A Math. Phys. Eng. Sci. **88**, 428–438 (1913). DOI: 10.1098/rspa.1913.0040.

[204] S. Kurtaran and M. S. Kılıçkaya, "The modelling of Fiber Bragg Grating," Opt. Quantum Electron. **39**, 643–650 (2007). DOI: 10.1007/s11082-007-9117-1.

[205] T. Tamir, *Guided-Wave Optoelectronics*, Springer Series in Electronics and Photonics (Springer Berlin Heidelberg, 1988), Vol. 26. ISBN: 978-3-642-97076-4.

[206] I. A. Glover and P. M. Grant, *Digital Communications* (2003), Vol. 49. ISBN: 9780273718307.

[207] F. Ouellette, "Dispersion cancellation using linearly chirped Bragg grating filters in optical waveguides.," Opt. Lett. **12**, 847 (1987). DOI: 10.1364/OL.12.000847.

[208] M. Sumetsky and B. J. Eggleton, "Fiber Bragg gratings for dispersion

compensation in optical communication systems," J. Opt. Fiber Commun. Reports **2**, 256–278 (2005). DOI: 10.1007/s10297-004-0026-9.

[209] N. M. Litchinitser, M. Sumetsky, and P. S. Westbrook, "Fiber-based tunable dispersion compensation," J. Opt. Fiber Commun. Reports **4**, 41–85 (2007). DOI: 10.1007/s10297-006-0072-6.

[210] I. Riant, S. Gurib, J. Gourhant, et al., "Chirped Fiber Bragg Gratings for WDM Chromatic Dispersion Compensation in Multispan 10-Gb / s Transmission," **5**, 1312–1324 (1999).

[211] K. O. Hill, K. Takiguchi, F. Bilodeau, et al., "Chirped in-fiber Bragg gratings for compensation of optical-fiber dispersion," Opt. Lett. **19**, 1314 (1994). DOI: 10.1364/OL.19.001314.

[212] G. Imeshev, I. Hartl, and M. E. Fermann, "Chirped pulse amplification with a nonlinearly chirped fiber Bragg grating matched to the Treacy compressor.," Opt. Lett. **29**, 679–681 (2004). DOI: 10.1364/OL.29.000679.

[213] M. E. Fermann, K. Sugden, and I. Bennion, "High-power soliton fiber laser based on pulse width control with chirped fiber Bragg gratings.," Opt. Lett. **20**, 172–4 (1995).

[214] O. Katz and Y. Sintov, "Strictly all-fiber picosecond ytterbium fiber laser utilizing chirped-fiber-Bragg-gratings for dispersion control," Opt. Commun. **281**, 2874–2878 (2008). DOI: 10.1016/j.optcom.2008.01.048.

[215] R. Paschotta, J. Nilsson, A. C. Tropper, and D. C. Hanna, "Ytterbium-doped fiber amplifiers," IEEE J. Quantum Electron. **33**, 1049–1056 (1997). DOI: 10.1109/3.594865.

[216] J. M. Senior and M. Y. Jamro, *Optical Fiber Communications: Principles and Practice* (2009). ISBN: 013032681X. DOI: 10.1080/716099703.

[217] J. R. Marciante and J. D. Zuegel, "High-gain, polarization-preserving, Yb-doped fiber amplifier for low-duty-cycle pulse amplification," Appl. Opt. **45**, 6798 (2006). DOI: 10.1364/AO.45.006798.

[218] H. A. Haus, "Theory of mode locking with a fast saturable absorber," J. Appl. Phys. **46**, 3049 (1975). DOI: 10.1063/1.321997.

[219] M. Hercher, "An Analysis of Saturable Absorbers," Appl. Opt. **6**, 947 (1967). DOI: 10.1364/AO.6.000947.

[220] M. Haiml, R. Grange, and U. Keller, "Optical characterization of semiconductor saturable absorbers," Appl. Phys. B **79**, 331–339 (2004). DOI: 10.1007/s00340-004-1535-1.

[221] Y. Sintov, O. Katz, Y. Glick, et al., "Extractable energy from ytterbium-doped high-energy pulsed fiber amplifiers and lasers," J. Opt. Soc. Am. B **23**, 218 (2006). DOI: 10.1364/JOSAB.23.000218.

[222] Z. Huang, J. Wang, H. Lin, et al., "Combined numerical model of laser rate equation and Ginzburg–Landau equation for ytterbium-doped fiber amplifier," J. Opt. Soc. Am. B **29**, 1418 (2012). DOI: 10.1364/JOSAB.29.001418.

[223] F. He, J. H. Price, K. T. Vu, et al., "Optimisation of cascaded Yb fiber amplifier chains using numerical-modelling," Opt. Express **14**, 12846 (2006). DOI: 10.1364/OE.14.012846.

[224] G. Liu and D. Liu, "Optimization of pumping mode for double-clad fiber lasers," Opt. Laser Technol. **40**, 256–260 (2008). DOI: 10.1016/j.optlastec.2007.04.010.

[225] O. Svelto, *Principles of Lasers* (Springer, 2010). ISBN: 978-1-4419-1302-9.

[226] N. A. Brilliant, R. J. Beach, A. D. Drobshoff, and S. A. Payne, "Narrow-line ytterbium fiber master-oscillator power amplifier," J. Opt. Soc. Am. B **19**, 981 (2002). DOI: 10.1364/JOSAB.19.000981.

[227] F. Trager, *Springer Handbook of Lasers and Optics* (Springer New York, 2007). ISBN: 978-0-387-95579-7.

[228] C. H. Brito Cruz, P. C. Becker, R. L. Fork, and C. V Shank, "Phase correction of femtosecond optical pulses using a combination of prisms and gratings," Opt. Lett. **13**, 123 (1988). DOI: 10.1364/OL.13.000123.

[229] R. L. Fork, O. E. Martinez, and J. P. Gordon, "Negative dispersion using pairs of prisms," Opt. Lett. **9**, 150 (1984). DOI: 10.1364/OL.9.000150.

[230] R. L. Fork, C. H. Brito Cruz, P. C. Becker, and C. V. Shank, "Compression

of optical pulses to six femtoseconds by using cubic phase compensation," Opt. Lett. **12**, 483 (1987). DOI: 10.1364/OL.12.000483.

[231] R. Zhang, D. Pang, J. Sun, et al., "Analytical expressions of group-delay dispersion and cubic phase for four-prism sequence used at other than Brewster's angle," Opt. Laser Technol. **31**, 373–379 (1999). DOI: 10.1016/S0030-3992(99)00082-1.

[232] A. Präkelt, M. Wollenhaupt, A. Assion, et al., "Compact, robust, and flexible setup for femtosecond pulse shaping," Rev. Sci. Instrum. **74**, 4950–4953 (2003). DOI: 10.1063/1.1611998.

[233] M. Pessot, P. Maine, and G. Mourou, "1000 times expansion/compression of optical pulses for chirped pulse amplification," Opt. Commun. **62**, 419–421 (1987). DOI: 10.1016/0030-4018(87)90011-3.

[234] C. Fiorini, C. Sauteret, C. Rouyer, et al., "Temporal aberrations due to misalignments of a stretcher-compressor system and compensation," IEEE J. Quantum Electron. **30**, 1662–1670 (1994). DOI: 10.1109/3.299499.

[235] F. Salin, J. Squier, and G. Mourou, "Large temporal stretching of ultrashort pulses," Appl. Opt. **31**, 1225 (1992). DOI: 10.1364/AO.31.001225.

[236] M. Lai, S. T. Lai, and C. Swinger, "Single-grating laser pulse stretcher and compressor," Appl. Opt. **33**, 6985 (1994). DOI: 10.1364/AO.33.006985.

[237] J. Jiang, Z. Zhang, and T. Hasama, "Evaluation of chirped-pulse-amplification systems with Offner triplet telescope stretchers," J. Opt. Soc. Am. B **19**, 678 (2002). DOI: 10.1364/JOSAB.19.000678.